# Advances
## in Clinical and Experimental Medicine

## Wroclaw
## MEDICAL UNIVERSITY

# Advances
## in Clinical and Experimental Medicine
### Medicine

# Advances
## in Clinical and Experimental Medicine

## Editorial Policy

# Contents

# Dentists can provide reliable shear wave elastography measurements of the stiffness of masseter muscles: A possible scenario for a faster diagnostic process

Cyprian Olchowy[1,A–F], Anna Olchowy[2,A,B,D,F], Jakub Hadzik[1,B,E,F], Paweł Dąbrowski[3,A,C,F], Dorota Mierzwa[1,C]

[1] Department of Oral Surgery, Wroclaw Medical University, Poland

[2] Department of Experimental Dentistry, Wroclaw Medical University, Poland

[3] Division of Normal Anatomy, Department of Human Morphology and Embryology, Wroclaw Medical University, Poland

A – research concept and design; B – collection and/or assembly of data; C – data analysis and interpretation;
D – writing the article; E – critical revision of the article; F – final approval of the article

## Abstract

**Background.** Masseter muscle pathologies include hypertrophy and the experience of pain, which clinically manifest with increased stiffness and tension. Assessment of muscle stiffness has been gaining importance among physicians dealing with temporomandibular disorders (TMD). Currently, shear wave elastography (SWE) is still often performed by radiologists, while dentists diagnose, treat and monitor TMD.

**Objectives.** In this cohort study, we investigated whether dentists trained to use SWE can obtain reliable measurements of masseter muscle stiffness following participation in a short training program and hands-on workshop.

**Materials and methods.** A group of healthy volunteers was examined by an experienced radiologist and a novice dentist before and after the training.

**Results.** The mean values of stiffness obtained by the operators were consistent and ranged from 10.20 kPa to 10.84 kPa. Intraobserver agreement was excellent for measurements of the radiologist (intraclass correlation coefficient (ICC) 0.92 and 0.93, respectively). The training improved the agreement between measurements made by the dentist from poor before the training (ICC = 0.46) to good after the training (ICC = 0.89). Also, the operator agreement between the radiologist and dentist increased from poor (ICC = 0.48) before the training to good (ICC = 0.84) after the training.

**Conclusions.** The diagnostic accuracy of measuring masseter muscle stiffness was acceptable among dentists after the training. For this reason, the patient can be diagnosed by a single TMD specialist. This can shorten the diagnostic process and reduce treatment costs.

**Key words:** elasticity, temporomandibular disorders, shear wave elastography, intraobserver agreement, interobserver agreement

# Background

Assessment of muscle stiffness using shear wave elastography (SWE) has been gaining importance and greater interest among physicians dealing with temporomandibular disorders (TMD).[1] First, it is an objective method for the evaluation of muscle and soft tissue stiffness in general. Second, it provides repeatable and reliable measurements that can be compared with other results over the treatment period and against the normal values. Third, muscle stiffness measured with SWE reflects the condition of the muscle.[2] Shear wave elastography was developed to differentiate between malignant and benign thyroid and breast nodules, but now the method is gaining wider application in other areas, including in muscles. In addition, the method is quick – a reliable examination by a skilled examiner takes about 1 min. Other methods of masseter muscle assessment have been reported to be useful (including electromyography, portable muscle hardness meter and manual palpation), but they are of less importance.[3,4] The precision of SWE is rooted in shear waves created by ultrasound push beams that lead to tissue displacement that is detected using pulse-echo ultrasound. Young's modulus is used to calculate stiffness based on wave velocity.[5]

Most studies on SWE do not provide information about the specialty and experience of the examiner[6,7]; however, many reports on TMD indicate that masseter muscle examinations were performed by radiologists.[8–13] Attempts have been made to engage radiologists in the monitoring of the treatment results of other pathologies of the stomatognathic system using SWE, such as bruxism and many other oral and maxillofacial diseases.[12,14] To the best of our knowledge, no studies have investigated SWE performed by a dentist.

The TMD consists of a group of symptoms whose classification and taxonomy are evolving.[15] The current diagnostic system for TMD (Diagnostic Criteria for Temporomandibular Disorders (DC/TMD)) focuses on physical symptoms of the temporomandibular joints and masseter muscles (axis I) and assessment of psychosocial and behavioral factors (axis II).[16] This being said, the current criteria are based on clinical symptoms and disturbed functioning, which are mostly subjective. Masseter muscle pathologies include hypertrophy and the experience of pain, which clinically manifest with increased stiffness and tension.[15–17] Treatment of TMD is complex, especially if other chronic diseases coexist.[18,19] The diagnostic process of TMD can be performed by dentists and maxillofacial surgeons. Physical therapists are usually engaged in treatment. Patients benefit from this multidisciplinary approach[20]; however, at the same time, late or mistaken diagnosis and delayed treatment due to other reasons contribute to the chronicity of the disease.[21] For this reason, methods of rapid assessment of the patient's condition, which could be used during routine check-ups by dentists.

Due to the specificity of TMD, the diagnostic process and treatment are conducted by dentists. Currently, SWE of the masseter muscles is performed by radiologists who have limited knowledge about TMD. In contrast, in other specialties of medicine, SWE of internal organs can be conducted by physicians who treat the disease themselves and, at the same time, can use this examination as a fast, cheap and non-invasive modality to evaluate disease progression or to check the effectiveness of the treatment being used.[22,23] Furthermore, SWE can be performed by a trained radiology technician.[24] Such approaches may help in designing faster pathways for diagnosis and treatment evaluation as well as reducing treatment costs.

# Objectives

The aim of this study was to investigate whether TMD specialists and dentists trained to use SWE can obtain reliable measurements of masseter muscle stiffness following participation in a short training program and hands-on workshop. We hypothesized that stiffness of the masseter muscle could be measured with similar accuracy by experienced radiologists and trained dentists with limited experience. For this purpose, interobserver agreement was analyzed.

# Materials and methods

## Study design

This cohort study included 51 healthy adult volunteers. Patients were recruited in September 2020 and examined through October 2020. All SWE examinations were performed by a radiologist with 7 years of experience and a dentist with limited experience who participated in a tailored training program. This 1.5-hour training program included ultrasound anatomy of the masseter muscle, technicalities of the Aixplorer Ultimate device (SuperSonic Imagine, Aix-en-Provence, France), and stiffness measurements. Masseter muscle stiffness measurements were performed twice. In the 1st round, measurements were made by the experienced radiologist and the novice dentist (30 people). After the 1st round, the dentist participated in the training seminar, which included experience sharing during which they could dispel doubts, discuss difficult cases, improve skills, and learn how to perform examinations correctly. In the 2nd round, measurements were made by the experienced radiologist and the novice dentist who participated in the training seminar (21 people). During the study, both observers were blinded to each other's measurements as well as to the participant's condition. Measurements conducted by the dentist were made immediately after (obligatory within 10 min) the examinations by the radiologist.

## Participants

Masseter muscle stiffness was measured in an outpatient setting. Fifty-one healthy adult volunteers were enrolled in the study. Volunteers were divided into 2 groups and examined by the radiologist and dentist before and after the training. The 1st group consisted of 30 people (12 men and 18 women) with a median age of 42 years. In the 2nd round, 21 people (6 men and 15 women) with a median age of 43 years were examined.

Only subjects without signs and symptoms suggestive of TMD based on DC/TMD were included.[15] The exclusion criteria were the following: any neuromuscular disorders, malignancy or pain within the masseter muscles; a diagnosis of TMD in the history with or without treatment of TMD; current treatment with muscle relaxants and/or other drugs affecting muscle function; pregnancy; and breastfeeding. The study was conducted in accordance with the Declaration of Helsinki, and the protocol was approved by the Bioethical Committee of the Wroclaw Medical University. All subjects gave their informed consent for inclusion before they participated in the study.

Masseter muscle stiffness expressed in kilopascals was a continuous variable. The condition of the masseter muscles was confirmed during the physical examination and medical history of the participants.

## Data sources/measurement

To measure masseter muscle stiffness, the Aixplorer Ultimate device with a high-frequency linear probe SL 18–5 (5–18 MHz) with a width of 55 mm was used. Propagation of shear waves in tissues varies between 1 m/s and 10 m/s, which corresponds to elasticity of 1 kPa to 300 kPa. The tests were performed in the morning, before the first meal. The subjects were asked to lie down in the supine position, remain relaxed and comfortable during the examination, and refrain from swallowing. Before the examination, the probe was covered with an ultrasound gel for better visualization. The patients' tissues were not compressed. The probe was placed longitudinally to the long axis of the masseter muscle, and a region of interest (ROI) with a circle size of 4 mm was positioned in the center of the muscle (the widest part of the muscle belly). The center of the masseter muscle was defined as the widest part of the masseter muscle belly and confirmed by ultrasound. With each patient, 10 measurements of the left masseter muscle and 5 measurements of the right masseter muscle were recorded and analyzed.

All measurements were performed in the same settings and conditions to ensure that the impact of other factors on muscle stiffness was eliminated. The study group included healthy people without any pathology of the masseter muscles.

## Statistical methods

The collected data were stored in an Excel spreadsheet (Microsoft Excel 2013; Microsoft Corp., Redmond, USA) and statistically analyzed using the MedCalc v. 19.5.3 (MedCalc Software Ltd., Ostend, Belgium). Means and standard deviations (SDs) were calculated. Reproducibility of the results was assessed using a descriptive statistic – intraclass correlation coefficient (ICC).[25] Intraobserver agreement was evaluated based on a comparison of the first 5 measurements and the last 5 measurements of the left masseter muscle by the same examiner. For interobserver agreement, measurements carried out by the radiologist and the dentist were compared (the first 5 measurements from before the training and the 5 measurements after the training were considered). The ICC values were interpreted as poor for ICC below 0.5, moderate for ICC between 0.5 and 0.75, good for ICC between 0.75 and 0.9, and excellent for ICC above 0.9.[26] The ICC estimates and their 95% confidence intervals (95% CIs) were calculated using the MedCalc v. 19.5.3 based on the reliability of single ratings (k = 2), consistency, two-way model, and the same raters for all subjects. Graphical presentation of operator agreements was presented on Bland–Altman plots.

## Results

The overall mean stiffness of the masseter muscle measured by the radiologist was 10.73 kPa. Table 1 presents details (means with mean SDs) of stiffness values recorded by the radiologist and the dentist before and after the training. Operator agreement, measured with ICC, between the radiologist and dentist increased from 0.48 before the training to 0.84 after the training. The ICC values are presented in Table 2.

A graphical presentation of the interobserver agreement is depicted in Fig. 1. The plots showed a mean difference of –0.1 kPa between operators before the training and –0.07 kPa after the training. The limits of agreement were larger before the training (from –1.01 to 0.98) than after the training (from –0.94 to 0.80).

The mean values of stiffness of the healthy masseter muscles obtained by the operators were consistent and ranged from 10.54 kPa to 10.88 kPa. However, SD values were higher for the dentist's measurements than for the radiologist's measurements, which indicates greater variability for the measurements of the novice operator. The operator agreement between the radiologist and dentist increased from moderate (ICC = 0.48) before the training to good (ICC = 0.84) after the training.

## Discussion

The main strength of the study is that its design excluded other sources of variability, such as patient characteristics (e.g., amount of subcutaneous fatty tissue and age), known

Table 1. Measurement of stiffness

| Measurement | Radiologist | | Dentist | |
| --- | --- | --- | --- | --- |
| | mean | mean SD | mean | mean SD |
| Left masseter – before training [kPa] | 10.72 | 2.32 | 10.85 | 3.13 |
| Right masseter – before training [kPa] | 10.88 | 2.34 | 10.80 | 3.65 |
| Left masseter – after training [kPa] | 10.67 | 2.23 | 10.73 | 2.50 |
| Right masseter – after training [kPa] | 10.54 | 2.38 | 10.58 | 2.79 |

SD – standard deviation.

Table 2. Operator agreement

| Agreement | Comparison | ICC |
| --- | --- | --- |
| Intra-observer (left masseter) | radiologist – before training | 0.92 (95% CI: 0.84–0.96) |
| | radiologist – after training | 0.93 (95% CI: 0.83–0.97) |
| | dentist – before training | 0.46 (95% CI: 0.13–0.7) |
| | dentist – after training | 0.89 (95% CI: 0.75–0.95) |
| Inter-observer (all measurements) | before training radiologist–dentist | 0.48 (95% CI: 0.26–0.65) |
| | after training radiologist–dentist | 0.84 (95% CI: 0.71–0.91) |

CI – confidence interval; ICC – intraclass correlation coefficient.

to contribute to interobserver differences.[27] All examinations were performed on the same subjects and in the same environment, so the experience of the examiner was the only variable that changed during the study. We believe this is the first study aimed at evaluating the interobserver accuracy of SWE in the evaluation of masseter muscle stiffness.

Although SWE has been proven to be a reliable method that produces reproducible results in kPa, allowing for comparison between patients and different time points

in the patient, its results can be affected by many factors. One factor is the experience and knowledge of the examiner and the associated learning curve.[28,29] Several approaches have been used to quantify differences among observers reporting the same measurements, with interobserver agreement being the most commonly used.

Interobserver and intraobserver reproducibility of SWE has been investigated for other organs, but not for the masseter muscle until now. For example, Ferraioli et al.[30] evaluated the reproducibility of real-time SWE in the evaluation of liver stiffness. They reported an ICC of 0.93–0.95 for intraobserver agreement between measurements performed in the same subject on the same day. The ICC for intraobserver agreement dropped to 0.65–0.84 when the examination was carried out in the same subject but on different days. The ICC for interobserver agreement was 0.88. The study was performed on 42 healthy volunteers by 2 examiners. The 1st examiner, a radiologist, had more than 20 years of experience in abdominal ultrasound and 4 years of experience in elastography, while the 2nd operator had limited experience (3 months of training in ultrasound and 1 day of training in SWE). They determined that based on their experience, a novice examiner should perform at least 50 supervised scans to obtain consistent results. In another study on liver stiffness measurements carried out by Grădinaru-Taşcău et al.[31] on 371 consecutive subjects, the number of reliable examinations was
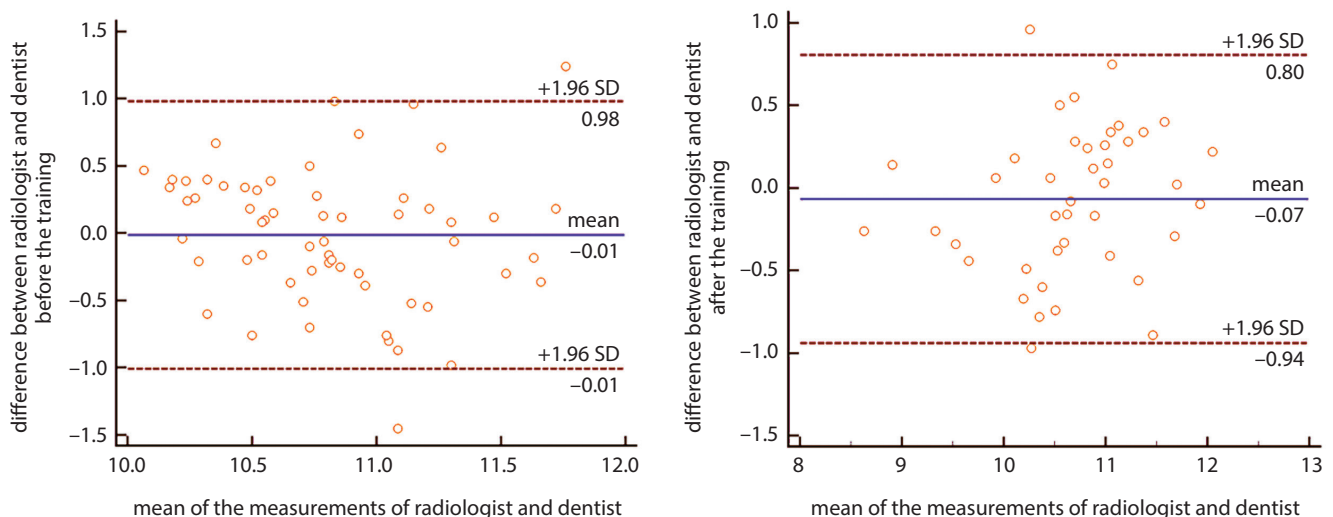


Fig. 1. Measurement of stiffness of masseter muscles carried out by the radiologist and dentist before and after the training (Bland–Altman plots)

significantly higher for an experienced examiner than for a novice (87.4% compared to 72.8%; p = 0.001). However, this difference disappeared when overweight patients were excluded from the comparison. Their findings suggest that there might also be some factors in masseter muscle stiffness measurements that make the examination more difficult for novice operators. Those factors were not investigated in the present study. We recommend the investigation of such factors in future research.

Ultrasound examinations are the domain of radiologists; however, reports from the literature indicate that ultrasound scans can also offer clinical benefits to patients when performed by treating physicians or physicians of other specialties. A number of studies suggest that the results of ultrasound examinations for screening purposes carried out by residents with minimal training have acceptable diagnostic accuracy. Ruddox et al.[32] compared the diagnostic accuracy of pocket-size cardiac ultrasound performed by experienced echocardiographers and residents with minimal experience. At the start of the study, all internal medicine residents participated in a 2-hour introductory course in pocket-size cardiac ultrasound. The comparison included data on 303 patients suspected of having heart failure or experiencing chest pain. The overall agreement reported was moderate (k = 0.50). The authors concluded that ultrasound examinations performed by residents were good enough to help with rapid differential diagnosis upon patient admission. Another study by Lucas et al.[33] investigated the diagnostic accuracy of hand-carried ultrasound echocardiography performed by physicians who had participated in a 27-hour training program. After comparing the results of initial hand-carried ultrasound echocardiography with standard echocardiography, the authors concluded that the diagnostic accuracy of detecting 6 cardiac abnormalities was moderate-to-excellent. The authors also highlighted that echocardiography performed by physicians with limited experience may fill an important gap in cases where cardiac pathologies need to be diagnosed quickly, but standard echocardiography is unavailable.

## Limitations

This study has some limitations that need to be mentioned. First, it included a relatively small number of subjects, and all were healthy volunteers who did not present any pathologies of the stomatognathic system. For this reason, we could not investigate whether SWE could be used to distinguish normal from pathological findings within the masseter muscle. Another limitation is that this study evaluated SWE only, so it did not compare this technique to other techniques used to assess the condition of masseter muscles. Also, up-to-date, normal ranges of masseter muscle stiffness have not yet been developed. Finally, no association between higher stiffness of the masseter muscle and TMD has been fully proven yet. For this reason, we could not calculate the sensitivity and specificity of this method.

## Conclusions

The diagnostic accuracy of measuring masseter muscle stiffness was acceptable among dentists after a short training program and hands-on workshop. These results suggest that patients could benefit from a complete evaluation performed by one specialist during a single visit. This would shorten the diagnostic process and reduce costs.

## ORCID iDs

Cyprian Olchowy  https://orcid.org/0000-0002-6559-3973
Anna Olchowy  https://orcid.org/0000-0002-5601-7173
Jakub Hadzik  https://orcid.org/0000-0002-2353-3198
Paweł Dąbrowski  https://orcid.org/0000-0001-6016-9201
Dorota Mierzwa  https://orcid.org/0000-0002-1041-1968

## References

1. Olchowy A, Wieckiewicz M, Winocur E, et al. Great potential of ultrasound elastography for the assessment of the masseter muscle in patients with temporomandibular disorders: A systematic review. *Dentomaxillofac Radiol*. 2020;49(8):20200024. doi:10.1259/dmfr.20200024
2. Goo M, Johnston LM, Hug F, Tucker K. Systematic review of instrumented measures of skeletal muscle mechanical properties: Evidence for the application of shear wave elastography with children. *Ultrasound Med Biol*. 2020;46(8):1831–1840. doi:10.1016/j.ultrasmedbio.2020.04.009
3. Pessoa DR, Costa DR, Prianti BM, et al. Association of facial massage, dry needling, and laser therapy in temporomandibular disorder: Case report. *Codas*. 2018;30(6):e20170265. doi:10.1590/2317-1782/20182017265
4. Hiraiwa Y, Ariji Y, Kise Y, Sakuma S, Kurita K, Ariji E. Efficacy of massage treatment technique in masseter muscle hardness: Robotic experimental approach. *Cranio*. 2013;31(4):291–299. doi:10.1179/crn.2013.31.4.007
5. Creze M, Nordez A, Soubeyrand M, Rocher L, Maître X, Bellin MF. Shear wave sonoelastography of skeletal muscle: Basic principles, biomechanical concepts, clinical applications, and future perspectives. *Skeletal Radiol*. 2018;47(4):457–471. doi:10.1007/s00256-017-2843-y
6. Badea I, Tamas-Szora A, Chiorean I, Fildan F, Ciulea E, Badea M. Quantitative assessment of the masseter muscle's elasticity using acoustic radiation force impulse. *Med Ultrason*. 2014;16(2):89–94. doi:10.11152/mu.201.3.2066.162.ib1asz2
7. Ariji Y, Nakayama M, Nishiyama W, Nozawa M, Ariji E. Shear-wave sonoelastography for assessing masseter muscle hardness in comparison with strain sonoelastography: Study with phantoms and healthy volunteers. *Dentomaxillofac Radiol*. 2016;45(2):20150251. doi:10.1259/dmfr.20150251
8. Herman J, Sedlackova Z, Vachutka J, Furst T, Salzman R, Vomacka J. Shear wave elastography parameters of normal soft tissues of the neck. *Biomed Pap Med Fac Univ Palacky Olomouc Czech Repub*. 2017;161(3):320–325. doi:10.5507/bp.2017.024
9. Ewertsen C, Carlsen J, Perveez MA, Schytz H. Reference values for shear wave elastography of neck and shoulder muscles in healthy individuals. *Ultrasound Int Open*. 2018;4(1):E23–E29. doi:10.1055/s-0044-102013
10. Gotoh A, Ariji Y, Hasegawa T, et al. Sonographic elastography for assessing changes in masseter muscle elasticity after low-level static contraction. *Oral Radiol*. 2013;29(2):140–145. doi:10.1007/s11282-012-0119-8
11. Arda K, Ciledag N, Aktas E, Aribas BA, Köse K. Quantitative assessment of normal soft-tissue elasticity using shear-wave ultrasound elastography. *AJR Am J Roentgenol*. 2011;197(3):532–536. doi:10.2214/ajr.10.5449
12. Ogura I, Nakahara K, Sasaki Y, Sue M, Oda T. Usefulness of shear wave elastography in the diagnosis of oral and maxillofacial diseases. *Imaging Sci Dent*. 2018;48(3):161–165. doi:10.5624/isd.2018.48.3.161

13. Olchowy C, Więckiewicz M, Sconfienza LM, et al. Potential of using shear wave elastography in the clinical evaluation and monitoring of changes in masseter muscle stiffness. *Pain Res Manag*. 2020;2020: 4184268. doi:10.1155/2020/4184268

14. Yazici G, Kafa N, Kolsuz ME, Volkan-Yazici M, Evli C, Orhan K. Evaluation of single session physical therapy methods in bruxism patients using shear wave ultrasonography. *Cranio*. 2020:1–7. doi:10.1080/08869634. 2020.1812817

15. Schiffman E, Ohrbach R. Executive summary of the Diagnostic Criteria for Temporomandibular Disorders for clinical and research applications. *J Am Dent Assoc*. 2016;147(6):438–445. doi:10.1016/j.adaj.2016.01.007

16. Peck CC, Goulet JP, Lobbezoo F, et al. Expanding the taxonomy of the diagnostic criteria for temporomandibular disorders. *J Oral Rehabil*. 2014;41(1):2–23. doi:10.1111/joor.12132

17. Osiewicz M, Manfredini D, Biesiada G, et al. Prevalence of function-dependent temporomandibular joint and masticatory muscle pain, and predictors of temporomandibular disorders among patients with Lyme disease. *J Clin Med*. 2019;8(7):929. doi:10.3390/jcm8070929

18. Byun SH, Min C, Choi HG, Hong SJ. Increased risk of temporomandibular joint disorder in patients with rheumatoid arthritis: A longitudinal follow-up study. *J Clin Med*. 2020;9(9):3005. doi:10.3390/jcm9093005

19. Walter C, Lechner KH, Karl M. A pilot study on spatial changes in the maxilla caused by osteopathic therapy. *Quintessence Int*. 2015; 46(1):81–86. doi:10.3290/j.qi.a32513

20. Garrigós-Pedrón M, Elizagaray-García I, Domínguez-Gordillo AA, Del-Castillo-Pardo-de-Vera JL, Gil-Martínez A. Temporomandibular disorders: Improving outcomes using a multidisciplinary approach. *J Multidiscip Healthc*. 2019;12:733–747. doi:10.2147/JMDH.S178507

21. Schiffman E, Ohrbach R, Truelove E, et al; International RDC/TMD Consortium Network, International association for Dental Research; Orofacial Pain Special Interest Group, International Association for the Study of Pain. Diagnostic Criteria for Temporomandibular Disorders (DC/TMD) for Clinical and Research Applications: Recommendations of the International RDC/TMD Consortium Network and Orofacial Pain Special Interest Group. *J Oral Facial Pain Headache*. 2014; 28(1):6–27. doi:10.11607/jop.1151

22. Cieciura T, Hryniewiecka E, Perkowska-Ptasińska A, Ciszek M, Pączek L. Shear wave elastography performance in noninvasive assessment of liver cirrhosis in liver transplant recipients with the recurrence of hepatitis C infection. *Transplant Proc*. 2020;52(8):2480–2483. doi:10.1016/j.transproceed.2020.02.097

23. Łasecki M, Olchowy C, Sokołowska-Dąbek D, Biel A, Chaber R, Zaleska-Dorobisz U. Modified sonoelastographic scale score for lymph node assessment in lymphoma: A preliminary report. *J Ultrason*. 2015; 15(60):45–55. doi:10.15557/JoU.2015.0004

24. Shaheen AA, Riazi K, Medellin A, et al. Risk stratification of patients with nonalcoholic fatty liver disease using a case identification pathway in primary care: A cross-sectional study. *CMAJ Open*. 2020;8(2): E370–E376. doi:10.9778/cmajo.20200009

25. Stanish WM, Taylor N. Estimation of the intraclass correlation coefficient for the analysis of covariance model. *Am Stat*. 1983;37:221–224. doi:10.1080/00031305.1983.10483107

26. Koo TK, Li MY. A guideline of selecting and reporting intraclass correlation coefficients for reliability research. *J Chiropr Med*. 2016;15(2): 155–163. doi:10.1016/j.jcm.2016.02.012

27. Boursier J, Konate A, Guilluy M, et al. Learning curve and interobserver reproducibility evaluation of liver stiffness measurement by transient elastography. *Eur J Gastroenterol Hepatol*. 2008;20(7):693–701. doi:10.1097/MEG.0b013e3282f51992

28. Sporea I, Mare R, Popescu A, Sirli R, Pienar C. Learning curve evaluation using Elastpq. *Ultrasound Med Biol*. 2017;43:S100. doi:10.1016/j.ultrasmedbio.2017.08.1276

29. Ferraioli G, Tinelli C, Zicchetti M, et al. Reproducibility of real-time shear wave elastography in the evaluation of liver elasticity. *Eur J Radiol*. 2012;81(11):3102–3106. doi:10.1016/j.ejrad.2012.05.030

30. Grădinaru-Taşcău O, Sporea I, Bota S, et al. Does experience play a role in the ability to perform liver stiffness measurements by means of supersonic shear imaging (SSI)? *Med Ultrason*. 2013;15(3):180–183. doi:10.11152/mu.2013.2066.153.ogt1is2

31. Ruddox V, Stokke TM, Edvardsen T, et al. The diagnostic accuracy of pocket-size cardiac ultrasound performed by unselected residents with minimal training. *Int J Cardiovasc Imaging*. 2013;29(8):1749–1757. doi:10.1007/s10554-013-0278-7

32. Lucas BP, Candotti C, Margeta B, et al. Diagnostic accuracy of hospitalist-performed hand-carried ultrasound echocardiography after a brief training program. *J Hosp Med*. 2009;4(6):340–349. doi:10.1002/jhm.438

33. Yoon K, Jeong WK, Kim Y, Kim MY, Kim TY, Sohn JH. 2-dimensional shear wave elastography: Interobserver agreement and factors related to interobserver discrepancy. *PLoS One*. 2017;12(4):e0175747. doi:10.1371/journal.pone.0175747

# Low-intensity pulsed ultrasound enhances angiogenesis in rabbit capsule tissue that acts as a novel vascular bed in vivo

Mingming Yu[1,2,A,B,D], Yu Bian[2,C], Lin Wang[1,2,B], Fang Chen[1,2,E,F]

[1] Department of Urology, Shanghai Children's Hospital, Shanghai Jiao Tong University, China

[2] Department of Urology, Shanghai Sixth People's Hospital affiliated with Jiao Tong University, China

A – research concept and design; B – collection and/or assembly of data; C – data analysis and interpretation;
D – writing the article; E – critical revision of the article; F – final approval of the article

## Abstract

**Background.** In vivo prevascularization followed by pedicled transfer has emerged as a promising strategy for tissue engineering in recent years. We recently demonstrated that capsule tissue could serve as a novel axial in vivo vascular bed, although its high-density microvessels could only be maintained for about a week.

**Objectives.** In this present study, we aimed to demonstrate whether low-intensity pulsed ultrasound (LIPUS) promotes angiogenesis in capsule tissue.

**Materials and methods.** After successful induction of capsule tissue using a skin expander, 24 rabbits were randomly divided into the LIPUS group and the control group. The LIPUS group received LIPUS treatment 3 times per week. After 2 and 4 weeks of treatment, angiogenesis of the capsule tissue was assessed using in vivo and in vitro methods, including contrast-enhanced ultrasound (CEUS), photoacoustic imaging (PAI), photoacoustic microscope (PAM), and CD31 immunohistochemistry.

**Results.** In vivo assessments (CEUS, PAI and PAM) showed that tissue perfusion, hemoglobin content and vascular density were all significantly higher in the LIPUS group, which was consistent with CD31 immunohistochemistry. The LIPUS also promoted protein and mRNA expression of vascular endothelial growth factor α (VEGFα) and basic fibroblast growth factor (bFGF) in capsule tissue. Furthermore, cell experiments showed that LIPUS enhanced tube formation of human microvascular endothelial cells (HMECs) and promoted secretion of VEGFα and bFGF.

**Conclusions.** The LIPUS treatment promoted angiogenesis of the capsule tissue by stimulating release of angiogenic factors such as VEGFα and bFGF from endothelial cells, making the capsule tissue more potent and sustained when acting as in vivo vascular bed.

**Key words:** low-intensity pulsed ultrasound, capsule tissue, angiogenesis, vascular bed, tissue engineering

582

F. Chen et al. Ultrasound enhances angiogenesis in capsule

# Background

Timely vascularization to establish blood supply after implantation is essential for successful reconstruction and is one of the major challenges currently faced by tissue engineering. Classical approaches, including optimization of the material properties of the scaffolds, addition of angiogenic factors and inclusion of microvascular networks in the constructs, are barely suitable for large grafts.[1] Prevascularization on in vivo or in vitro vascular beds and fabrication of vascularized constructs with vascular pedicles have been proven to be promising solutions to this problem.[2,3]

Capsule tissue induced by an expander can serve as an in vivo vascular bed due to its unique blood supply. Bengtson et al. demonstrated that an isolated flap of capsule tissue can survive as a local pedicle flap to provide sufficient inherent vascularity to support a split-thickness skin graft in pigs.[4] This study was the first to use the capsule tissue as an in vivo vascular bed. Schoeller et al. utilized pouch-like capsule tissue to cultivate urothelial cells suspended in fibrin glue and fabricate a pre-laminated flap for bladder reconstruction in a rat model.[5] In addition, capsule tissue can be used as a tissue-engineered blood vessel for arteriovenous grafting by changing its shape to a tubular shape.[6] Moreover, capsule tissue can be directly used to rebuild tissue defects or redefine the tissue border in clinical practice.[7,8]

In our previous study, the capsule tissue induced by an expander served as a novel in vivo vascular bed for cultivating smooth muscle cell sheets or buccal mucosa and fabricating vascularized and pedicled constructs that can be successfully used for bladder or urethra reconstruction.[9–12] However, according to our findings, the vascular density within the capsule tissue was highest 1 week after the full expansion, rapidly declined in the next week, and then tended to remain stable at a relatively low level.[9] This phenomenon may limit the application of the method in multilayered engineered tissues, which usually need a few weeks to stack together and form integrated tissues.

Low-intensity pulsed ultrasound (LIPUS) has been proven to be effective in promoting angiogenesis under many conditions, such as cardiac dysfunction, tissue injury and tissue engineering.[13–15] However, LIPUS has rarely been applied to promote angiogenesis in the vascular bed for tissue engineering.

Thus, in the present study, we aimed to determine whether LIPUS ameliorates vascularization of the capsule tissue through therapeutic angiogenesis and enhances the potency and durability of this in vivo vascular bed for tissue engineering.

# Objectives

The purpose of the study was to promote angiogenesis in the capsule tissue by LIPUS, which may enhance the efficacy and sustainability of this in vivo vascular bed

for tissue engineering, and to preliminarily investigate the mechanism of this proangiogenic effect.

# Materials and methods

## Animals and study design

The animal protocol was approved by the Ethics Committee of Shanghai Sixth People's Hospital affiliated with Jiao Tong University, China. Twenty-four male New Zealand white rabbits, purchased from Shanghai Jiao Tong University and raised in the same feeding room, were randomly divided into 2 groups (n = 12 per group) using a random number table. Only the authors in charge of research design and conduct of the treatment were aware of the group allocation. The LIPUS group was treated with LIPUS 3 times per week (every Monday, Wednesday and Friday) after a successful induction of the capsule tissue (2 weeks after implantation of an expander), and the control group received the same treatment with the LIPUS device turned off. Angiogenesis in the capsule tissues of rabbits in the 2 groups was evaluated 2 and 4 weeks after LIPUS treatment (n = 6 per time point for each group). Obvious complications such as infection, wound disruption or poor healing at any point throughout the whole process were criteria for exclusion.

## Expander capsule induction

Following general anesthesia, inguinal incisions were made at an average length of 2 cm, and the superficial circumflex iliac vessels (SCIs) were carefully isolated from the surrounding tissue. An empty spherical skin expander (10 mL) was placed around separated SCIs to induce the capsule tissue (Fig. 1A). Starting from day 8 after the implantation, 3 mL of saline solution was injected into the expanders every other day until the expanders were fully expanded (Fig. 1B). Full expansion took 2 weeks after skin expander implantation, and the capsule tissue was fully formed at this time point.

## LIPUS application

After full expansion, LIPUS treatment was applied 3 times per week for 2 or 4 weeks using a portable ultrasound device (LIFU-DT100; Institute of Ultrasound Imaging of Chongqing Medical University, Chongqing, China). Comprehensive comparison of previous studies suggested the following conditions for LIPUS treatment: a pulse frequency of 1.0 MHz, an output intensity of 200 mW/cm$^2$, a duty cycle of 20%, and a repetition rate of 100 Hz.[14–16] Rabbits were anesthetized, and the skin around the expander was cleaned. Then, LIPUS was administered to the skin around the expander for 20 min for each rabbit (Fig. 1C). The probe was slowly moved over the skin to ensure that the capsule tissue was treated evenly
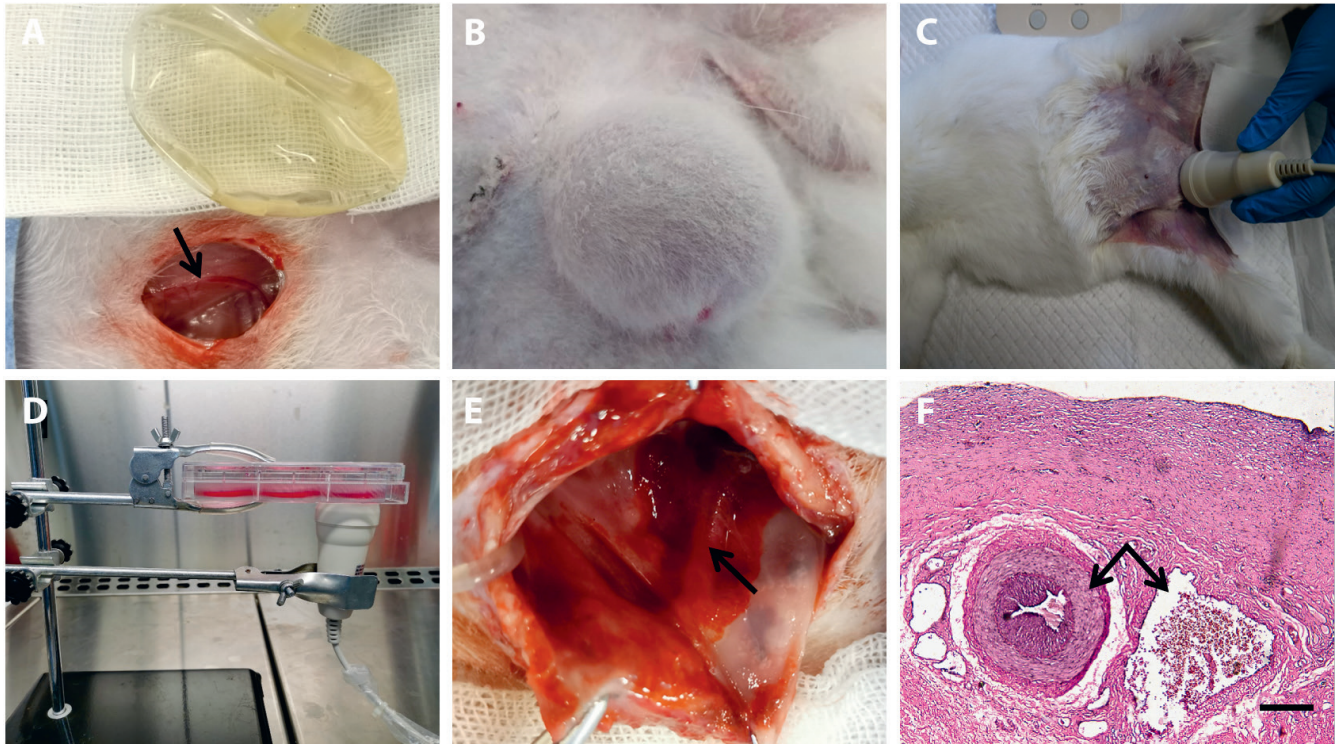
**Fig. 1.** Induction of the capsule tissue using a skin expander. A. A skin expander was placed to surround the separated superficial circumflex iliac vessels (SCIs) in the groin; B. The skin expander was fully injected 2 weeks after the implantation; C. The application of LIPUS on rabbit capsule tissue; D. The application of LIPUS on HMECs in vitro; E. Gross appearance of the induced capsule tissue; F. H&E staining showed that SCIs were located in the central layer of the capsule tissue. Black arrow – SCIs; scale bars = 200 μm

and to prevent local overheating. The rabbits in the control group received the same anesthesia and treatment procedures with the device turned off.

## Contrast-enhanced ultrasound

Contrast-enhanced ultrasound (CEUS) was performed with a MyladTwice eHD instrument (Esaote, Genoa, Italy) using a CA541 probe (1–8 MHz bandwidth). The rabbits were anesthetized and placed in the prone position. The best image plane was confirmed under greyscale ultrasonography scanning. The examination data were acquired immediately after a 0.1 mL bolus injection of SonoVue (Bracco Suisse SA, Geneva, Switzerland) followed by a saline flush into the ear vein of each rabbit. The images were obtained before and during microbubble passage through the capsule tissue. The region of interest (ROI) was manually selected in each image based on the border of the capsule tissue, and the time-intensity curves were plotted using Sonomath software (developed by the Department of Ultrasound in Medicine, Shanghai Sixth People's Hospital affiliated with Jiao Tong University, Shanghai, China).

## Photoacoustic imaging

Photoacoustic imaging (PAI) was performed using a PrexionLED AcousticX instrument (PreXion Co. Ltd.,

Tokyo, Japan) with a 10 MHz transducer (L100AAN) immediately after CEUS. The lower part of the bodies of the rabbits were placed in a basin with warm water, and the sensor was pressed against the local skin to achieve better acoustic coupling between the sensor and the capsule tissues. The imaging parameters were set as follows: display mode: PA+B; frequency: 9 MHz; gain: 45 dB and 60 dB; and depth: 4 cm. Images were acquired at a wavelength of 850 nm corresponding to oxygenated hemoglobin. The results were recorded as images. The ROI was manually selected in each image based on the border of the capsule tissue, and the signal intensity was calculated using ColorQuantification software (developed by the Department of Ultrasound in Medicine, Shanghai Sixth People's Hospital affiliated with Jiao Tong University).

## Photoacoustic microscope scanning

A photoacoustic microscope (PAM) (Hadatomo™ Z WEL5200; Advantest, Tokyo, Japan) was used for three-dimensional (3D) imaging of the vasculature within the capsule tissue under the following settings: frequency: 500 MHz, wavelength: 532 nm, measurement range: 9 × 9 × 6 mm. The results were recorded, and the 3D distribution of the vessels was reconstructed using the software for enhanced calculation of the vascular density.

584

F. Chen et al. Ultrasound enhances angiogenesis in capsule

## Histological analysis

After general anesthesia, the capsule tissue of each rabbit was fully exposed. Then, the capsule tissues were harvested and placed in liquid nitrogen or 4% paraformaldehyde. The samples were embedded in paraffin and sectioned into 4-μm thick sections, and hematoxylin and eosin (H&E) staining was performed according to the standard protocols. In addition, the sections were deparaffinized and blocked with 3% bovine serum albumin (BSA) for 30 min followed by incubation with a mouse anti-CD31 monoclonal antibody (1 : 500; Abcam, Cambridge, UK). The images were acquired using fluorescence microscopy. Each slide was carefully examined at ×40 magnification to identify the area with the highest density of vessels. Then, 3 fields of view were selected at ×200 magnification. The number of CD31-positive vessels and the area ratios were quantified using ImageJ software (National Institutes of Health, Bethesda, USA).

## ELISA

The tissue samples were stored at 2–8°C after thawing and manually ground to homogeneity in phosphate-buffered saline (PBS) followed by centrifugation at $10,000 \times g$ for 20 min at 4°C. The supernatant was collected, and the protein levels of vascular endothelial growth factor α (VEGFα) and basic fibroblast growth factor (bFGF) in the supernatant were measured using enzyme-linked immunosorbent assay (ELISA) kits (Keshun, Shenzen, China) according to the manufacturer's instructions.

## Real-time PCR

RNA was extracted from the samples using TRIzol reagent (Invitrogen, Carlsbad, USA). Total RNA was converted to cDNA using an RT reagent kit (TaKaRa, Tokyo, Japan). The primer sequences were as follows: (forward) 5'-TGGCAGAAGAAGGAGACAATAA-3' and (reverse) 5'-GCACTCCAGGCTTTCATCATT-3' for VEGFα; (forward) 5'-AGACTGCTGGCTTCTAAATGTGTT-3' and (reverse) 5'-TTCGTTTCAGTGCCACATACCA-3' for bFGF; and (forward) 5'-CCGCCCAGAACATCATCCCT-3' and (reverse) 5'-GCACTGTTGAAGTCGCAGGAGA-3' for glyceraldehyde-3-phosphate dehydrogenase (GAPDH).

Reverse transcription was performed at 37°C for 15 min; then, quantitative real-time polymerase chain reaction (qPCR) was performed using a SYBR5 Premix Ex Taq kit (TaKaRa). The qPCR was performed for 5 min at 95°C, followed by 40 cycles of 15 s at 95°C and 30 s at 65°C. The results are presented as the copy number of the target gene relative to that of *GAPDH*, which was used as a housekeeping gene.

## Cell culture and LIPUS treatment

Human microvascular endothelial cells (HMECs) were purchased from the American Type Culture Collection (ATCC, Manassas, USA) and used for in vitro experiments. The HMECs were reseeded into six-well cell culture plates overnight in complete MCDB 131 medium (Gibco, Waltham, USA) and then stimulated with LIPUS (Fig. 1D). The in vitro-cultured cells were in a fragile external environment different from the ones in vivo, and a previous study showed that an intensity over 200 mW/cm$^2$ might be harmful to cultured endothelial cells.[17] Thus, the parameters for cell treatment were set as follows: frequency of 1 MHz, intensity of 100 mW/cm$^2$ and duration of 10 min per day for 3 days. Control cells were subjected to the same treatment with the machine turned off. After the last stimulation, the cells were cultured in complete medium for another 30 min and harvested for tube formation assays and protein extraction.

## Endothelial cell tube formation assay and ELISA

Matrigel matrix (Becton Dickinson Biosciences, Franklin Lakes, USA) was added to prechilled 96-well plates at a dose of 50 μL/well and then incubated at 37°C for 3 min. The HMECs suspended in complete medium at a density of $2 \times 10^4$ cells/well were seeded in Matrigel-coated wells. After incubation for 8 h, tube formation was detected using an inverted microscope. The tube formation indicators (total length and total nodes) were measured using ImageJ software.

The HMECs were lysed using whole cell lysis buffer (Keshun) containing 1% phenylmethylsulfonyl fluoride (PMSF) and placed on ice for 30 min to extract total protein. Then, the protein levels of VEGFα and bFGF in the lysates were measured using ELISA kits (Keshun) according to the manufacturer's instructions.

## Statistical analyses

All statistical analyses were performed using GraphPad Prism v. 8.0 software (GraphPad Prism, San Diego, USA). The results are expressed as mean ± standard deviation (SD). Statistical analyses were performed using Student's t-test for two-group comparisons. A value of $p < 0.05$ were considered statistically significant.

# Results

## Characteristics of the capsule

Capsule tissues were successfully induced in all of the rabbits, and no rabbit was excluded due to obvious complications during the whole process. The morphology of the capsule tissue was hollow with a smooth surface. Pulsatile SCIs were located inside the capsule tissue, and numerous small vessels originated from axial SCIs and extended to the periphery of the capsule (Fig. 1E).

The H&E staining showed 3 layers of the capsule tissue: the cellular layer (closest to the expander), central layer and fibrous layer. The SCIs were located in the central layer surrounded by numerous microvessels (Fig. 1F).

## Effects of LIPUS on angiogenesis in the capsule tissue

Angiogenesis in the capsule tissue was assessed in vivo with CEUS (Fig. 2A), PAI (Fig. 2B) and PAM (Fig. 2C), which detected tissue perfusion, hemoglobin content and vessel density, respectively. The recordings were processed using the corresponding software as described in the Materials and methods section to quantify the signal intensity (Fig. 2D–F). The results showed that the signal intensities of CEUS, PAI and PAM were significantly higher in the LIPUS group (p < 0.01) 2 and 4 weeks after LIPUS treatment (Fig. 2G–I).

The results of CD31 immunohistochemistry showed a significantly higher number of vessels and greater CD31-positive areas in the LIPUS group (Fig. 3A,B). Although there was a decline in the LIPUS group at 4 weeks (p < 0.01), the vascular density remained relatively high. In addition, there was no significant difference between the 2 time points in the control group.
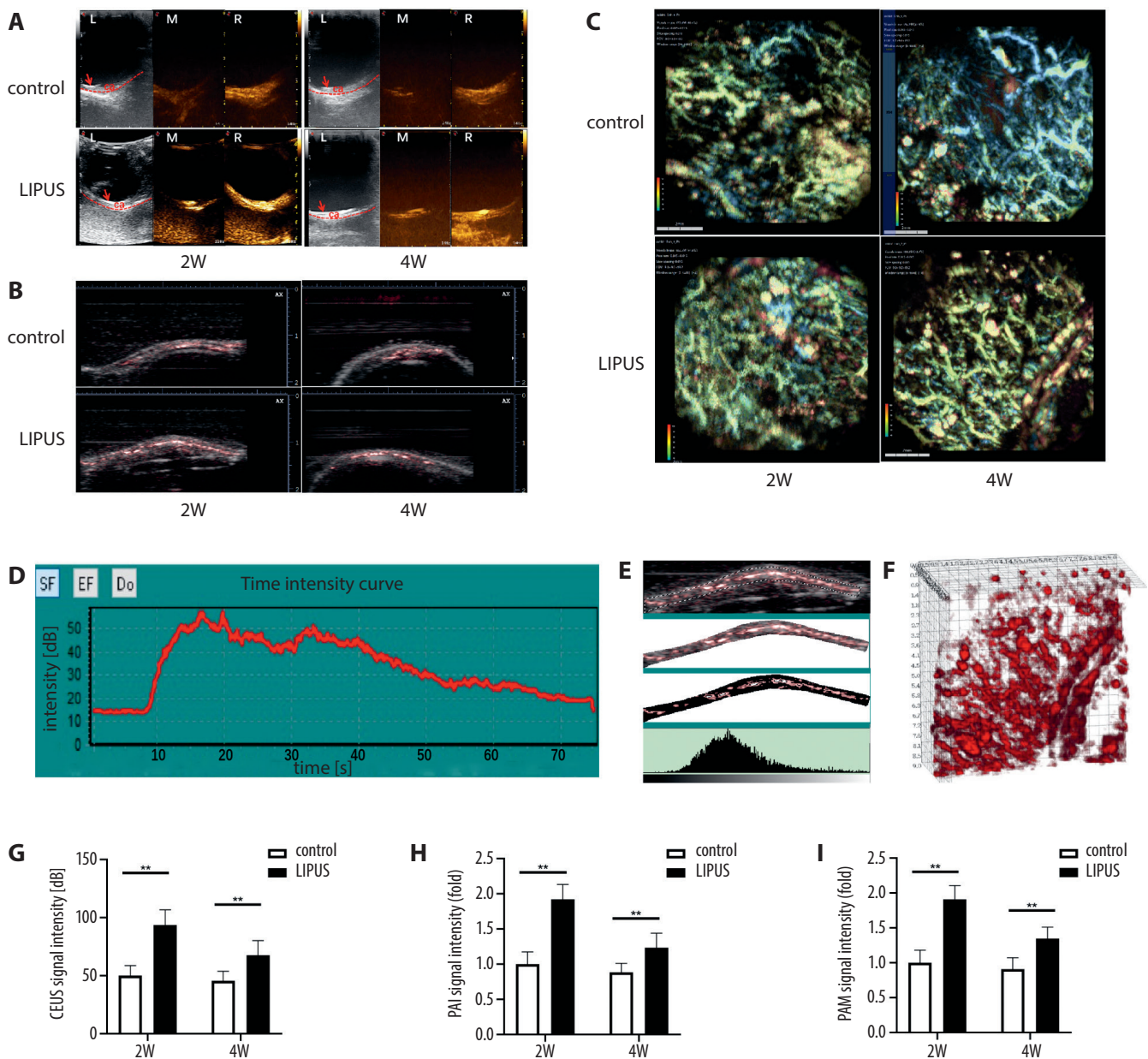


Fig. 2. LIPUS promoted tissue perfusion, increases in hemoglobin content and vascular density in the capsule tissue detected using CEUS, PAI and PAM, respectively. A. CEUS images of each group. Red arrow – the wall of the expander; L – greyscale ultrasonography scanning of the capsule tissue; M – before the injection of microbubbles; R – microbubbles passing through the capsule tissue; ca – capsule tissue; B. PAI of each group; C. Images obtained with PAM of each group (color scale: percentage of oxygen saturation); D. Time-intensity curve of CEUS; E. Quantitative analysis of the PAI signal intensity; F. Reconstructed 3D distribution of the vessels used for quantification; G–I. Comparison of CEUS, PAI and PAM signal intensities in each group and at each time point. The data are shown as mean ±SD; **p < 0.01

## Effects of LIPUS on the expression of protein and mRNA of VEGFα and bFGF in the capsule tissue

We then determined the effect of LIPUS treatment on the secretion of VEGFα and bFGF in the capsule tissue. The expression of protein and mRNA of VEGFα and bFGF in the capsule tissue was detected using ELISA and real-time PCR (RT-PCR), respectively. The results demonstrate that LIPUS enhanced the expression of VEGFα and bFGF at the protein and mRNA levels (Fig. 3C,D).

## Effects of LIPUS on HMECs

An in vitro tube formation assay was performed to assess the potential proangiogenic effects of LIPUS treatment on HMECs. The results indicated that LIPUS treatment apparently promoted tube formation in treated HMECs compared with that in the control cells (p < 0.01), including total length and total nodes (Fig. 4A,B). Furthermore, the results of ELISA of HMEC lysates showed that LIPUS treatment also enhanced the secretion of VEGFα and bFGF in HMECs (p < 0.01, Fig. 4C). These results indicate that LIPUS stimulated VEGFα and bFGF expression in HMECs and enhanced tube formation.

## Discussion

The lack of timely and functional vascularization has become a common shortcoming in tissue engineering.[18] For example, the clinical results of bladder reconstruction showed that engineered bladder tissues usually develop into fibrotic tissue due to insufficient blood supply.[19] Therefore, in recent years, the field of tissue engineering has turned towards angiogenesis, which is being actively pursued by a variety of physical and chemical methods, such as co-culture with endothelial cells and application of angiogenic growth factors using topographical engineering or 3D bioprinting.[1] However, these traditional strategies cannot produce a marked effect on large or thick tissue since the average growth rate of newly formed vasculature in transplanted tissue is only approx. 5 µm/h.[20] Pre-vascularization on a vascular bed with a pedicle, which can be finally transplanted together with the construct, has been recently proven to be an effective strategy because the vascular pedicle can provide sufficient and continuous blood supply for the graft.

Capsule tissue is a valuable in vivo vascular bed for tissue engineering[4] due to its unique blood supply and the flexibility to generate it in locations without sacrificing any normal tissue. In our previous studies, a tissue expander
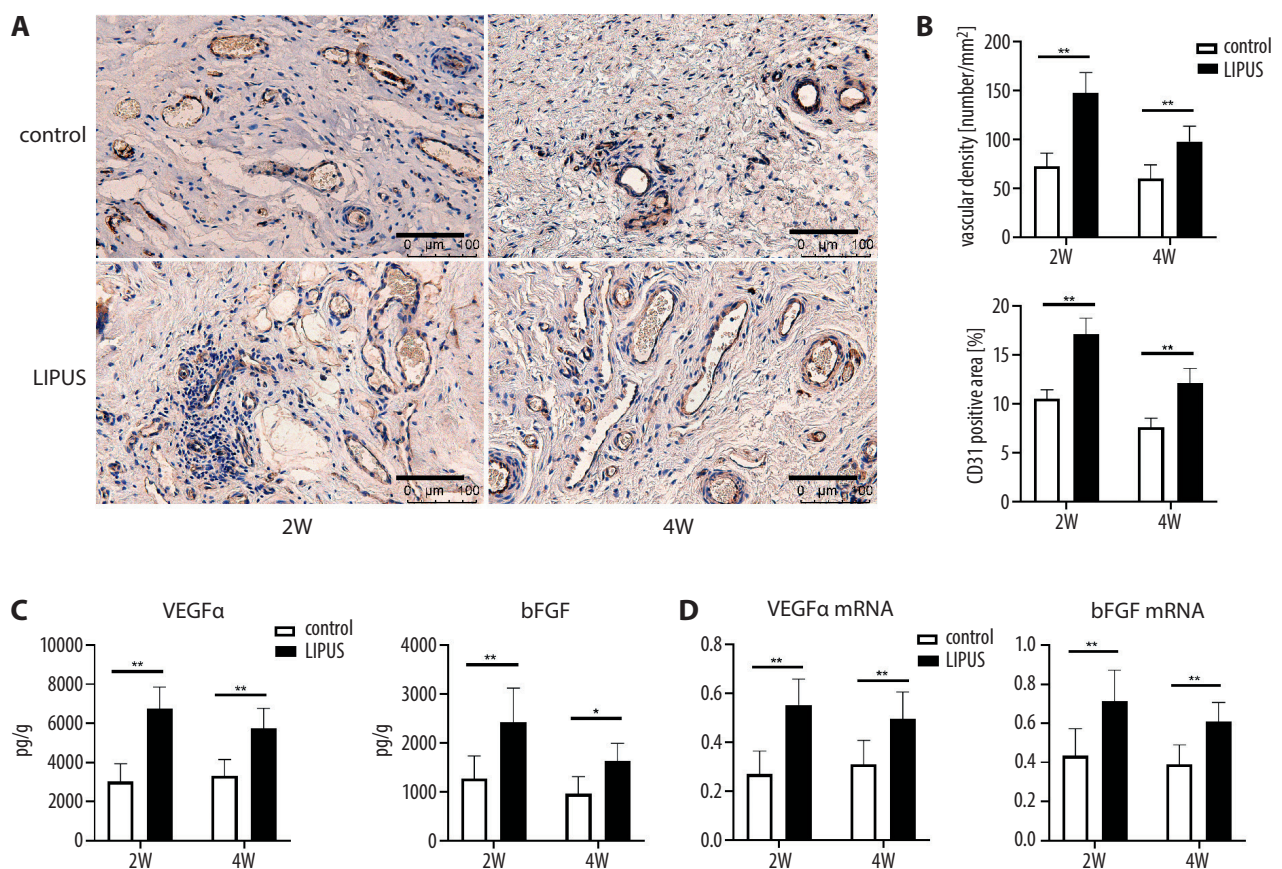


**Fig. 3.** LIPUS increased the number and area of blood vessels and upregulated the expression of VEGFα and bFGF at the protein and mRNA levels in the capsule tissue. A. CD31 immunohistochemical staining of each group; B. The number of CD31-positive vessels and CD31-positive areas in each group; C. Expression of VEGFα and bFGF detected using ELISA; D. Expression of VEGFα mRNA and bFGF mRNA detected using real-time PCR. The data are shown as mean ±SD; **p < 0.01; *p < 0.05; scale bars = 100 µm
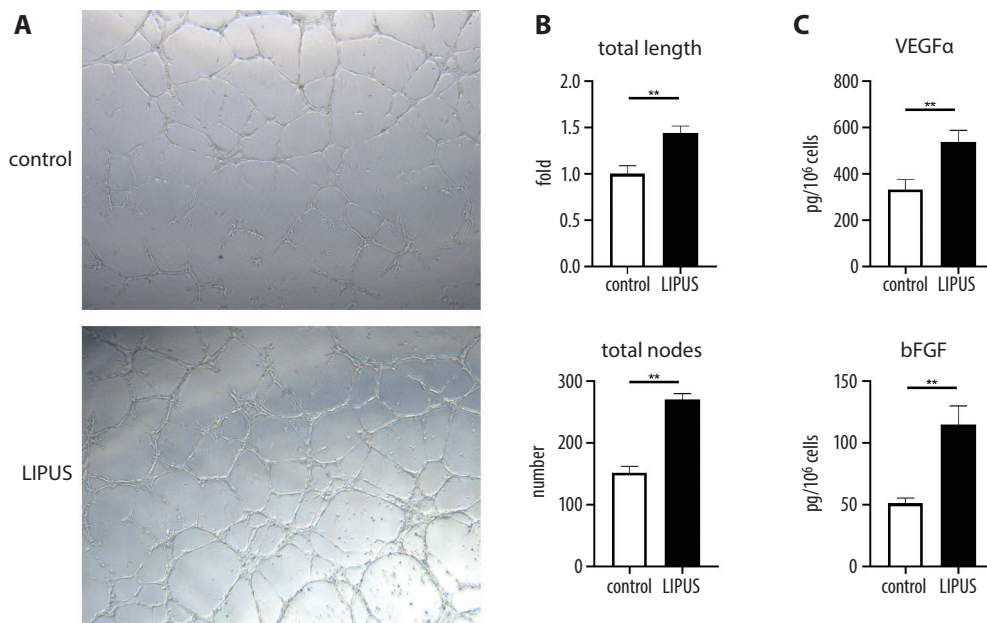
**Fig. 4.** LIPUS enhanced tube formation and upregulated the expression of VEGFα and bFGF in HMECs. A. Tube formation assay of HMECs; B. Quantified results of tube formation assay; C. Expression of VEGFα and bFGF in HMECs detected using ELISA. The results are expressed as mean ±SD; **p < 0.01

was placed to surround separated SCIs in the groin region to generate capsule tissue that contained an axial vascular pedicle influenced by SCIs. The effectiveness of the capsular vascular bed was verified by comparison with the subcutaneous vascular bed.[9] Subsequently, we used the capsule tissue as a vascular bed to cultivate free buccal mucosa grafts or multilayered smooth muscle cell sheets and fabricated pedicled vascularized constructs that can be successfully used for anterior and posterior urethra or bladder reconstruction, respectively.[10–12] The results were encouraging since the vascular pedicle continuously provided independent blood supply for the construct. However, we still encountered certain problems in the previous experiments. We demonstrated that the vascular density of the capsule tissue continued to increase after full expansion and reached its peak approx. 1 week later. Then, the vascular density rapidly decreased in the next week and remained stable. Thus, high efficiency of the capsular vascular bed can be maintained only for several days, which may limit the application of this method in the fabrication of multilayered constructs, such as full-thickness bladder tissue, that usually need multistage implantations and a long build time. Therefore, maintaining a sufficient blood supply of the capsule tissue for a sufficiently long time represents one of the major challenges.

The change in vascular density in the capsule tissue is related to its formation. Capsule tissue is the product of foreign body reaction against the implanted expander, which can be generally divided into 5 phases: 1) protein adsorption; 2) acute inflammation; 3) chronic inflammation; 4) foreign body giant cell formation; and 5) fibrosis or fibrous capsule formation.[21,22] Macrophages are predominant in the chronic inflammation phase and secrete many proangiogenic growth factors, such as VEGF, FGF and platelet-derived growth factor (PDGF), which play important role in angiogenesis. Therefore, a subsequent

decrease in inflammation results in gradual maturation of the initial capsule tissue into less cellular and more collagenous and thicker tissue. The concentration of angiogenic growth factors is thus reduced, leading to a decrease in vascular density.

The LIPUS is a noninvasive and straightforward technology that has been proven to be effective in promoting angiogenesis under many conditions. In the present study, we aimed to verify the angiogenic effect of LIPUS on the capsular vascular bed. The LIPUS treatment was applied 3 times per week after the expander was fully filled with saline solution, and the results show that tissue perfusion and vascular density of the capsule tissue were significantly enhanced by LIPUS treatment. After 2 weeks of LIPUS treatment, the vascular density of the capsule tissue almost reached the peak level of the untreated tissue registered 1 week after full expansion. Although the vascular density in the LIPUS group was decreased after 2 weeks, it remained relatively high, indicating that LIPUS treatment of the in vivo vascular bed enhanced the efficacy and sustainability of the capsule tissue. In addition, LIPUS resulted in prolonged upregulation of VEGFα and bFGF, 2 fundamental growth factors involved in angiogenesis, at the protein and mRNA levels.

The potential mechanism for the angiogenic effect of LIPUS has been explored before. Previous studies demonstrated that endothelial cells are sensitive to ultrasound waves, and LIPUS can alter their morphology, proliferative activity, gene expression, and protein secretion.[23] The acoustic streaming of LIPUS affects caveolae in endothelial cells, which play a key role in mechanotransduction via embedded mechanosensors, such as integrin and caveolin. Mechanical stimuli are then transmitted to several intracellular signaling pathways, such as the PI3K-Akt, Hippo and HIF-1α signaling pathways, to upregulate the expression of angiogenic growth factors and thus

enhance angiogenesis.[23–25] In addition, ultrasound can induce sonoporation on the endothelial cell membrane that results in an influx of calcium ions, which is correlated with this bioeffect.[26] Moreover, ultrasound can be used for the promotion of angiogenesis and monitoring of angiogenesis in vivo. The CEUS is a common method for the detection of angiogenesis, and targeted ultrasound contrast agents can produce stronger signals associated with angiogenesis.[27] The PAI technique is based on a combination of laser and ultrasound, which is particularly suitable for visualization of microvasculature due to high optical absorption of hemoglobin; it has proven valuable for monitoring neovascularization in tissue engineering.[28] The PAM is a new method for in vivo imaging of the microvasculature using high contrast and deep penetration, and has great potential for biomedical research.[29] Real-time in vivo monitoring of the vasculature enhances visualization of angiogenesis to provide an intuitive understanding of these processes for investigators.

## Limitations

The results of the present study are encouraging; however, some limitations remain. First, we selected a single set of parameters of LIPUS treatment based on previous studies. The best stimulation condition for capsule tissue requires additional exploration. Second, the effect of LIPUS on inflammation of the capsule tissue was not investigated, and inflammation plays an important role in capsule formation and angiogenesis. Finally, we only examined the proangiogenic effect on endothelial cells, while several types of cells in the capsule tissue, such as fibroblasts and smooth muscle cells, might be stimulated using LIPUS to some extent.

# Conclusions

The LIPUS treatment of vascular beds in vivo can enhance angiogenesis of the capsule tissue by stimulating microvascular endothelial cells to secrete proangiogenic growth factors. This approach can enhance the potency and sustainability of the capsule tissue and is thus extremely important for thick or multilayered constructs.

## ORCID iDs

Mingming Yu https://orcid.org/0000-0001-9957-6568
Yu Bian https://orcid.org/0000-0002-5735-7102
Lin Wang https://orcid.org/0000-0002-6509-6408
Fang Chen https://orcid.org/0000-0002-0242-331X

## References

1. Kant RJ, Coulombe KLK. Integrated approaches to spatiotemporally directing angiogenesis in host and engineered tissues. *Acta Biomater.* 2018;69:42–62. doi:10.1016/j.actbio.2018.01.017
2. Epple C, Haumer A, Ismail T, et al. Prefabrication of a large pedicled bone graft by engineering the germ for de novo vascularization and osteoinduction. *Biomaterials.* 2019;192:118–127. doi:10.1016/j.biomaterials.2018.11.008

3. Rnjak-Kovacina J, Gerrand YW, Wray LS, et al. Vascular pedicle and microchannels: Simple methods toward effective in vivo vascularization of 3D scaffolds. *Adv Healthc Mater.* 2019;8(24):e1901106. doi:10.1002/adhm.201901106
4. Bengtson BP, Ringler SL, George ER, DeHaan MR, Mills KA. Capsular tissue: A new local flap. *Plast Reconstr Surg.* 1993;91(6):1073–1079. doi:10.1097/00006534-199305000-00016
5. Schoeller T, Lille S, Stenzl A, et al. Bladder reconstruction using a prevascularized capsular tissue seeded with urothelial cells. *J Urol.* 2001;165(3):980–985. PMID:11176526
6. Geelhoed WJ, van der Bogt KEA, Rothuizen TC, et al. A novel method for engineering autologous non-thrombogenic in situ tissue-engineered blood vessels for arteriovenous grafting. *Biomaterials.* 2020;229:119577. doi:10.1016/j.biomaterials.2019.119577
7. DeGeorge Br Jr, Campbell CA. Techniques to refine the upper outer breast aesthetic subunit in alloplastic breast reconstruction: The lateral capsular flap. *Plast Surg (Oakv).* 2016;24(2):83–88. doi:10.4172/plastic-surgery.1000966
8. Josiassen M, Kudibal MT, Gramkow C, Trojahn Kølle SF. Closure of thoracic wall defect using breast implant capsule tissue as a rotation flap: A case report. *Case Reports Plast Surg Hand Surg.* 2018;5(1):39–40. doi:10.1080/23320885.2018.1476150
9. Jia Z, Guo H, Xie H, et al. Construction of pedicled smooth muscle tissues by combining the capsule tissue and cell sheet engineering. *Cell Transplant.* 2019;28(3):328–342. doi:10.1177/0963689718821682
10. Guo HL, Peng XF, Bao XQ, et al. Bladder reconstruction using autologous smooth muscle cell sheets grafted on a pre-vascularized capsule. *Theranostics.* 2020;10(23):10378–10393. doi:10.7150/thno.47006
11. Guo HL, Wang L, Jia ZM, et al. Tissue expander capsule as an induced vascular bed to prefabricate an axial vascularized buccal mucosa-lined flap for tubularized posterior urethral reconstruction: Preliminary results in an animal model. *Asian J Androl.* 2020;22(5):459–464. doi:10.4103/aja.aja_133_19
12. Guo HL, Jia ZM, Wang L, et al. Tubularized urethral reconstruction using a prevascularized capsular tissue prelaminated with buccal mucosa graft in a rabbit model. *Asian J Androl.* 2019;21(4):381–386. doi:10.4103/aja.aja_43_19
13. Kang PL, Huang HH, Chen T, Ju KC, Kuo SM. Angiogenesis-promoting effect of LIPUS on hADSCs and HUVECs cultured on collagen/hyaluronan scaffolds. *Mater Sci Eng C Mater Biol Appl.* 2019;102:22–33. doi:10.1016/j.msec.2019.04.045
14. Ogata T, Ito K, Shindo T, et al. Low-intensity pulsed ultrasound enhances angiogenesis and ameliorates contractile dysfunction of pressure-overloaded heart in mice. *PLoS One.* 2017;12(9):e0185555. doi:10.1371/journal.pone.0185555
15. Kamatsuki Y, Aoyama E, Furumatsu T, et al. Possible reparative effect of low-intensity pulsed ultrasound (LIPUS) on injured meniscus. *J Cell Commun Signal.* 2019;13(2):193–207. doi:10.1007/s12079-018-0496-9
16. Hanawa K, Ito K, Aizawa K, et al. Low-intensity pulsed ultrasound induces angiogenesis and ameliorates left ventricular dysfunction in a porcine model of chronic myocardial ischemia. *PLoS One.* 2014;9(8):e104863. doi:10.1371/journal.pone.0104863
17. Su Z, Xu T, Wang Y, et al. Low-intensity pulsed ultrasound promotes apoptosis and inhibits angiogenesis via p38 signaling-mediated endoplasmic reticulum stress in human endothelial cells. *Mol Med Rep.* 2019;19(6):4645–4654. doi:10.3892/mmr.2019.10136
18. Gholobova D, Terrie L, Mackova K, et al. Functional evaluation of prevascularization in one-stage versus two-stage tissue engineering approach of human bio-artificial muscle. *Biofabrication.* 2020;12(3):035021. doi:10.1088/1758-5090/ab8f36
19. Adamowicz J, Pokrywczynska M, Van Breda SV, Kloskowski T, Drewa T. Concise review: Tissue engineering of urinary bladder. We still have a long way to go? *Stem Cells Transl Med.* 2017;6(11):2033–2043. doi:10.1002/sctm.17-0101
20. Utzinger U, Baggett B, Weiss JA, Hoying JB, Edgar LT. Large-scale time series microscopy of neovessel growth during angiogenesis. *Angiogenesis.* 2015;18(3):219–232. doi:10.1007/s10456-015-9461-x
21. Kastellorizios M, Tipnis N, Burgess DJ. Foreign body reaction to subcutaneous implants. *Adv Exp Med Biol.* 2015;865:93–108. doi:10.1007/978-3-319-18603-0_6
22. Klopfleisch R, Jung F. The pathology of the foreign body reaction against biomaterials. *J Biomed Mater Res A.* 2017;105(3):927–940. doi:10.1002/jbm.a.35958

23. Huang JJ, Shi YQ, Li RL, et al. Angiogenesis effect of therapeutic ultrasound on HUVECs through activation of the PI3K-Akt-eNOS signal pathway. *Am J Transl Res*. 2015;7(6):1106–1115. PMID:26279754

24. Xu XM, Xu TM, Wei YB, et al. Low-intensity pulsed ultrasound treatment accelerates angiogenesis by activating YAP/TAZ in human umbilical vein endothelial cells. *Ultrasound Med Biol*. 2018;44(12):2655–2661. doi:10.1016/j.ultrasmedbio.2018.07.007

25. Costa V, Carina V, Conigliaro A, et al. miR-31-5p Is a LIPUS-mechanosensitive microRNA that targets HIF-1α signaling and cytoskeletal proteins. *Int J Mol Sci*. 2019;20(7):1569. doi:10.3390/ijms20071569

26. Hassan MA, Campbell P, Kondo T. The role of Ca(2+) in ultrasound-elicited bioeffects: Progress, perspectives and prospects. *Drug Discov Today*. 2010;15(21–22):892–906. doi:10.1016/j.drudis.2010.08.005

27. Lau C, Rivas M, Dinalo J, King K, Duddalwar V. Scoping review of targeted ultrasound contrast agents in the detection of angiogenesis. *J Ultrasound Med*. 2020;39(1):19–28. doi:10.1002/jum.15072

28. Ogunlade O, Ho JOY, Kalber TL, et al. Monitoring neovascularization and integration of decellularized human scaffolds using photoacoustic imaging. *Photoacoustics*. 2019;13:76–84. doi:10.1016/j.pacs.2019.01.001

29. Yang F, Wang Z, Zhang W, et al. Wide-field monitoring and real-time local recording of microvascular networks on small animals with a dual-raster-scanned photoacoustic microscope. *J Biophotonics*. 2020;13(6):e202000022. doi:10.1002/jbio.202000022

# Silencing of lncRNA *SNHG12* inhibits proliferation and migration of vascular smooth muscle cells via targeting *miR-766-5p/EIF5A* axis

Wen Liu[1,B,C,F], Jianhuan Che[2,C,D,F], Yan Gu[1,B,C,F], Ling Song[1,C,E,F], Yingying Jiao[1,A,C,F], Shui Yu[1,A,E,F]

[1] Department of Cardiovascular Medicine, The First Hospital of Jilin University, China

[2] Department of Oral and Maxillofacial Surgery, Hospital of Stomatology, Jilin University, China

A – research concept and design; B – collection and/or assembly of data; C – data analysis and interpretation;
D – writing the article; E – critical revision of the article; F – final approval of the article

**Address for correspondence**
Shui Yu
E-mail: qinlei256@163.com

## Abstract

**Background.** Although long non-coding RNAs (lncRNAs) have been reported to serve as potential biomarkers of atherosclerosis (AS), the role of lncRNA small nucleolar RNA host gene 12 (*SNHG12*) in AS still remains to be elucidated.

**Objectives.** The present study aimed to investigate the regulatory effects and potential mechanisms of *SNHG12* in human vascular smooth muscle cells (hVSMCs).

**Materials and methods.** Reverse-transcription quantitative polymerase chain reaction (RT-qPCR) was employed to determine the expression of *SNHG12*, *miR-766-5p* and eukaryotic translation initiation factor 5A (*EIF5A*) in oxidized low-density lipoprotein (ox-LDL)-induced hVSMCs. After transfection with short hairpin RNA (shRNA)-*SNHG12*, cell viability was estimated using the Cell Counting Kit-8 (CCK-8) assay. Wound healing and transwell assays were used for evaluating migratory capacities of hVSMCs. To further investigate the regulatory mechanisms, binding sites between *SNHG12* and *miR-766-5p*, and *EIF5A* and *miR-766-5p* were predicted using starBase database and validated using luciferase reporter gene assays. Moreover, cell viability and migration were detected following *EIF5A* overexpression and *SNHG12*-knockdown.

**Results.** *SNHG12* was significantly upregulated in ox-LDL-induced hVSMCs. *SNHG12* silencing inhibited ox-LDL-induced proliferation and migration of hVSMCs. Moreover, *SNHG12* acted as a sponge of *miR-766-5p*, and *miR-766-5p* also interacted with *EIF5A*. *EIF5A* plasmids promoted the capacities of proliferation and migration in ox-LDL-induced hVSMCs. However, shRNA-*SNHG12* counteracted the facilitation of *EIF5A* plasmids on hVSMCs biological behaviors.

**Conclusions.** Taken together, these findings demonstrated that silencing of *SNHG12* blocks the proliferation and migration of hVSMCs via targeting the *miR-766-5p/EIF5A* axis.

**Key words:** migration, *SNHG12*, human vascular smooth muscle cells, *miR-766-5p*, eukaryotic translation initiation factor 5A

592

W. Liu et al. Effects of *SNHG12* in ox-LDL-induced hVSMCs

# Background

Long non-coding RNAs (lncRNAs) are a heterogeneous class of non-coding RNAs greater than 200 nucleotides in length without protein-coding capacity.[1] Recently, studies have found that lncRNAs emerge as crucial regulators of atherosclerosis (AS).[2,3] Atherosclerosis is commonly recognized as a lipid-induced chronic inflammation of the vascular wall associated with activation and dysfunction of resident vascular cells[4] and contributes to stenosis of internal arteries due to plaque accumulation.[5] The number of lncRNAs was reported to be implicated in regulating cholesterol and lipid metabolism, and they also play diverse roles in a variety of atherosclerotic processes including cell proliferation, migration, inflammation, differentiation, and apoptosis.[6]

Small nucleolar RNA host gene 12 (*SNHG12*) is one of the classes of SNHGs.[7] Studies revealed that *SNHG12* regulates cell proliferation, migration, invasion, and metastasis in several cancers,[8–12] indicating a potential target for cancer-directed interventions.[13] Except for its role in cancers, *SNHG12* could also ameliorate brain microvascular endothelial cell injury.[14] To date, a number of well-studied lncRNAs gave us important clues about their potential for AS treatment.[15] For instance, lincRNA-p21 is downregulated in atherosclerotic plaques of ApoE(–/–) mice, and it can suppress vascular smooth muscle cell (VSMC) proliferation and induce apoptosis.[16] HIF1α-AS1 regulates the proliferation and apoptosis of VSMCs.[17] The expression of H19 is higher in serum of AS patients,[18] serving as a potential biomarker for diagnosing AS. However, the status, biological function and regulatory mechanisms of *SNHG12* in AS are still unknown.

# Objectives

We examined the expression of *SNHG12* in human VSMCs (hVSMCs) exposed to oxidized low density lipoprotein (ox-LDL) and evaluated the influence of *SNHG12* on cell migration. Furthermore, the regulatory mechanisms of *SNHG12* on hVSMCs were explored.

# Materials and methods

## Cell lines and transfection

The hVSMCs (Cell Bank of the Shanghai Institute of Cell Biology, Shanghai, China) were cultured in Dulbecco's modified Eagle's medium (DMEM; ProCell, Wuhan, China) containing 10% fetal bovine serum (FBS; Gibco, Waltham, USA) under an atmosphere of 95% air and 5% $CO_2$ at 37°C. The ox-LDL (Solarbio, Beijing, China) was used to stimulate hVSMCs for 48 h. *miR-766-5p* mimic, miR-NC (negative control), and 2 pairs of short hairpin RNA (shRNA)-SNHG12

(sh-SNHG12-1, sh-SNHG12-2) were obtained from GenePharma Co., Ltd. (Shanghai, China). Overexpression plasmids of *EIF5A* and the negative control were generated with the help of Sangon Biotech (Shanghai, China). Cells were collected 24 h following transfection, and transfection efficiency was evaluated using reverse-transcription quantitative polymerase chain reaction (RT-qPCR).

## RT-qPCR

Total RNA was harvested (TRIzol™ Plus RNA Purification Kit; Invitrogen, Carlsbad, USA) and reverse transcribed into cDNA (M-MLV Reverse Transcriptase; Promega, Madison, USA). TaqMan MicroRNA Assay kit (Applied Biosystems; Thermo Fisher Scientific, Waltham, USA) was employed to quantify *miR-766-5p*, the relative expression of *miR-766-5p* was normalized to U6, and others were normalized to *GAPDH* based on the $2^{-\Delta\Delta Ct}$ method.[19] The primers used in this study were as follows: *SNHG12*, forward: 5′-GTGATACTGAGGAGGTGAG-3′ and reverse: 5′-CCTTCTGCTTCCCATAGAG-3′; *EIF5A*, forward: 5′-AGGCCATGGCAAAATAACTG-3′ and reverse: 5′-GGGTGGGGAAAACCAAAATA-3′; *GAPDH*, forward: 5′-AGCCTCCCGCTTCGCTCTCTGC-3′ and reverse: 5′-ACCAGGCGCCCAATACGACCAAA-3′; *miR-766-5p*, forward: 5′-TCGAGTACTTGAGATGGAGTTTT-3′ and reverse: 5′-GGCCGCGTTGCAGTGAGCCGAG-3′; *U6*, forward: 5′-CTCGCTTCGGCAGCACA-3′ and reverse: 5′-AACGCTTCACGAATTTGCGT-3′.

## Cell viability assay

The hVSMCs were seeded into a 96-well plate, then cells were incubated with 10 μL Cell Counting Kit-8 (CCK-8) solution (Beyotime, Jiangsu, China) at 24 h, 48 h and 72 h. Absorbance values were recorded on a BioTek microplate reader (BioTek, Winooski, USA) at 450 nm.

## Wound healing assay

An amount of $1 \times 10^5$ of hVSMCs were plated into each well of a 12-well plate. When 100% confluence was achieved, the culture medium was removed and drew straight from the plate using a 200 μL plastic pipette. The sample was washed gently to remove the floating cells, then serum-free medium was added and maintained in the incubator for 24 h. Samples were photographed at 0 h and 24 h under a microscope (Axioscope 5; Carl Zeiss, Oberkochen, Germany).

## Transwell migration assay

For the transwell migration assay, serum-free media containing $5 \times 10^4$ of hVSMCs were seeded into the upper chamber of a 24-well transwell filter with 8-μm pore size. The lower chamber was filled with media supplemented

with 10% FBS. Cells were allowed to transgress through the porous filters for 24 h at 37°C. Then, VSMCs were fixed with 4% paraformaldehyde for 20 min. Cells that migrated through the pores of the filter were stained with 1% crystal violet for 30 min. The images were photographed under a fluorescence microscope (BX51; Olympus Corp., Tokyo, Japan), and the number of migrated cells was calculated using ImageJ software (National Institutes of Health, Bethesda, USA).

## Luciferase reporter gene assay

SNHG12 or EIF5A sequences containing the wild-type (WT) binding site or mutated-type (Mut) binding site for miR-766-5p were synthesized by Vigorous Biotechnology Beijing Co. Ltd. (Beijing, China) and cloned into the pmiR-GLO vector (Promega). Prior to transfection, cells were seeded into 24-well plates (5 × 10³ cells/well) and cultured for 24 h. Afterward, the WT or Mut of SNHG12 was transiently co-transfected with miR-766-5p mimics or miR-NC using Lipofectamine 3000 reagent for another 48 h. The firefly luciferase activity normalized to Renilla represented the value of relative luciferase activity. Likewise, EIF5A WT or Mut co-transfected with miR-766-5p mimic or miR-NC was similar to the above method.

## Western blotting

Total protein from treated cells was extracted using a radio immunoprecipitation assay lysis buffer containing proteinase inhibitors (Beyotime). After the determination of protein concentrations, equal protein samples (40 μg) were loaded on SDS-PAGE gels and transferred onto polyvinylidene difluoride (PVDF) membranes (Merck Millipore, Madison, USA). Then, the membranes were blocked with 5% non-fat milk for 2 h and incubated with primary antibodies against EIF5A and GAPDH (both obtained from Cell Signaling Technology, Inc., Danvers, USA) at 4°C overnight. Horseradish peroxidase (HRP)-conjugated antibody (Santa Cruz Biotechnology, Santa Cruz, USA) was used to incubate membranes for 2 h at room temperature. The blots were visualized using the Odyssey Infrared Imaging System (LI-COR Biosciences, Lincoln, USA) and subsequently quantified using ImageJ software v. 1.52r (National Institutes of Health).

## Statistical analyses

All data were presented as the mean ± standard deviation (SD). The results were analyzed using GraphPad Prism v. 6.0 (GraphPad Software, Inc., San Diego, USA). An unpaired student's t-test was employed to evaluate differences between 2 groups, and one-way analysis of variance (ANOVA) followed by Tukey's post hoc test was used for comparison of differences between 3 or more groups. A value of p < 0.05 was considered statistically significant.

# Results

## Interference with SNHG12 inhibits proliferation and migration of ox-LDL-induced hVSMCs

We first investigated the expression of SNHG12. The hVSMCs were stimulated with different concentrations of ox-LDL, and, as shown in Fig. 1A, ox-LDL could promote the expression of SNHG12 in a dose-dependent manner. A volume of 100 mg/L ox-LDL was considered an optimal concentration to induce the transcription of SNHG12. To elucidate the function of SNHG12 in hVSMCs, a loss-of-function study was performed via transfecting sh-SNHG12 into cells. It was identified that sh-SNHG12-1 presented a better outcome for silencing SNHG12 (Fig. 1B). Afterward, we estimated the cell viability of hVSMCs in the absence of SNHG12, and results showed that sh-SNHG12-1 transfection significantly inhibited the increased cell proliferation caused by ox-LDL stimulation (Fig. 1C). Moreover, the wound healing assay and transwell migration assay indicated that ox-LDL-triggered cell migration was overturned by silencing of SNHG12 (Fig. 1D–G). These results suggest that disturbing the expression of SNHG12 could inhibit the viability and migration of hVSMCs induced by ox-LDL.

## SNHG12 functions as a sponge of miR-766-5p

The LncRNAs are considered competing endogenous RNAs (ceRNAs) to bind with miRNAs and modulate gene expression.[20] Jia et al. demonstrated that miR-766-5p participated in cell proliferation, migration and invasion in colorectal cancer.[21] Of note, binding sites between SNHG12 and miR-766-5p were predicted using starBase v. 2.0 (http://starbase.sysu.edu.cn) (Fig. 2A), and miR-766-5p mimic was validated to be effective to elevate the expression of miR-766-5p (Fig. 2B). The luciferase reporter gene assay demonstrated that miR-766-5p mimic inhibited luciferase activity in hVSMCs transfected with SNHG12-WT (Fig. 2C). Additionally, it was found that sh-SNHG12-1 elevated the expression of miR-766-5p (Fig. 2D). Moreover, the level of miR-766-5p in hVSMCs treated with ox-LDL was notably decreased (Fig. 2E). Collectively, this data reveal that miR-766-5p is remarkably downregulated in ox-LDL-treated hVSMCs, and SNHG12 directly targeted miR-766-5p.

## EIF5A is a direct target gene of miR-766-5p

As mentioned above, SNHG12 directly targeted miR-766-5p and served as a ceRNA to bind with miR-766-5p. The ceRNA activity forms a large-scale cross-talk network among the transcriptome. The miRNAs are generally regarded as active regulatory elements which reduce
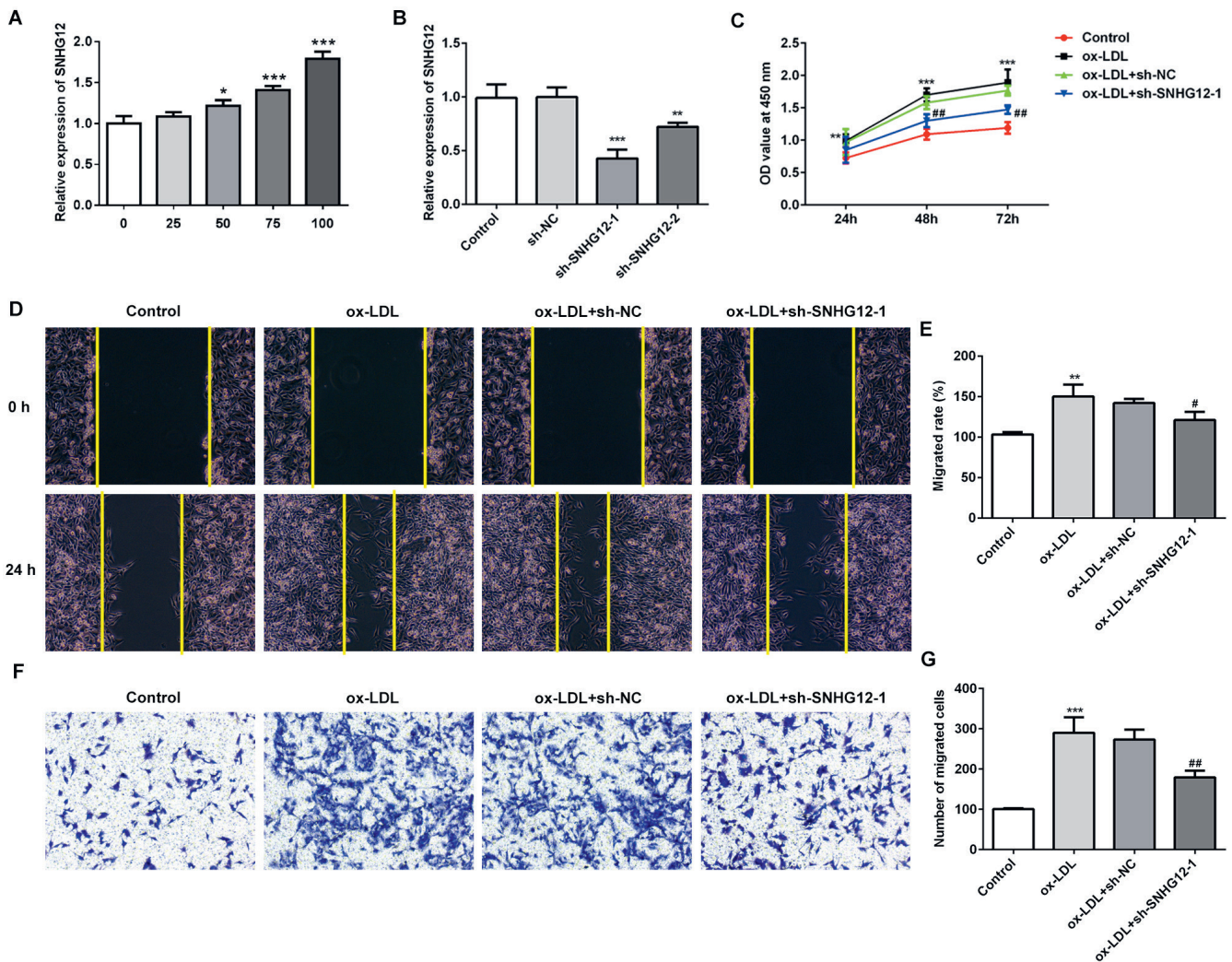
**Fig. 1.** Interference with *SNHG12* inhibits proliferation and migration of hVSMCs

A. hVSMCs were stimulated with different concentrations of ox-LDL (0 mg/L, 25 mg/L, 50 mg/L, 75 mg/L, 100 mg/L), and the expression of *SNHG12* was explored using RT-qPCR; *p < 0.05, ***p < 0.001 compared to 0 mg/L ox-LDL; B. The expression of *SNHG12* in hVSMCs transfected with sh-SNHG12-1 or sh-SNHG12-2 was estimated using RT-qPCR; **p < 0.01, ***p < 0.001 compared to the sh-NC group; C. hVSMCs were stimulated with 100 mg/L ox-LDL for 24 h, 48 h and 72 h, and the cell viability was explored using CCK-8 assay; **p < 0.01, ***p < 0.001 compared to the control group; ##p < 0.01 compared to the ox-LDL+sh-NC group. The capability of cell migration was assessed using wound healing assay (D and E) and transwell migration assay (F and G); **p < 0.01, ***p < 0.001 compared to the control group; #p < 0.05, ##p < 0.01 compared to the ox-LDL+sh-NC group; ×100 magnification.

the stability of target RNAs or inhibit their translation.[22] Therefore, target mRNAs are considered as silencing objects of miRNAs. *EIF5A* is a small molecule protein in eukaryotic cells, which plays an important role in cell growth, survival and senescence. It is especially essential for cell proliferation.[23] Of note, *EIF5A* was predicted as a potential target of *miR-766-5p* (Fig. 3A). Luciferase reporter gene analysis was employed to test the potential interaction between them. It was observed that *miR-766-5p* mimic apparently decreased the luciferase activity of *EIF5A*-WT in hVSMCs, and mutation of *EIF5A* abrogated the function of *miR-766-5p* mimic (Fig. 3B). Subsequently, overexpression of *miR-766-5p* reduced the transcription and translation of *EIF5A* (Fig. 3C,D). All of these data indicate that *EIF5A* may be a target mRNA of *miR-766-5p*.

## *SNHG12* regulates the proliferation and migration of ox-LDL-induced hVSMCs via regulating *EIF5A*

In order to further explore the interaction between *EIF5A* and *SNHG12*, gain-of-function and loss-of-function studies were applied in subsequent experiments. Overexpression plasmids were constructed and transfected into hVSMCs with or without sh-SNHG12-1, and high-expression of *EIF5A* validated the plasmids could overexpress *EIF5A* successfully. However, sh-SNHG12-1 drastically impeded the mRNA and protein levels of *EIF5A* (Fig. 4A,B). Cell viability was elevated in *EIF5A* overexpression group, while the effect was abolished by knockdown of *SNHG12* (Fig. 4C). Migratory capacity represented by wound width illustrated that *EIF5A* promoted hVSMCs migration, while
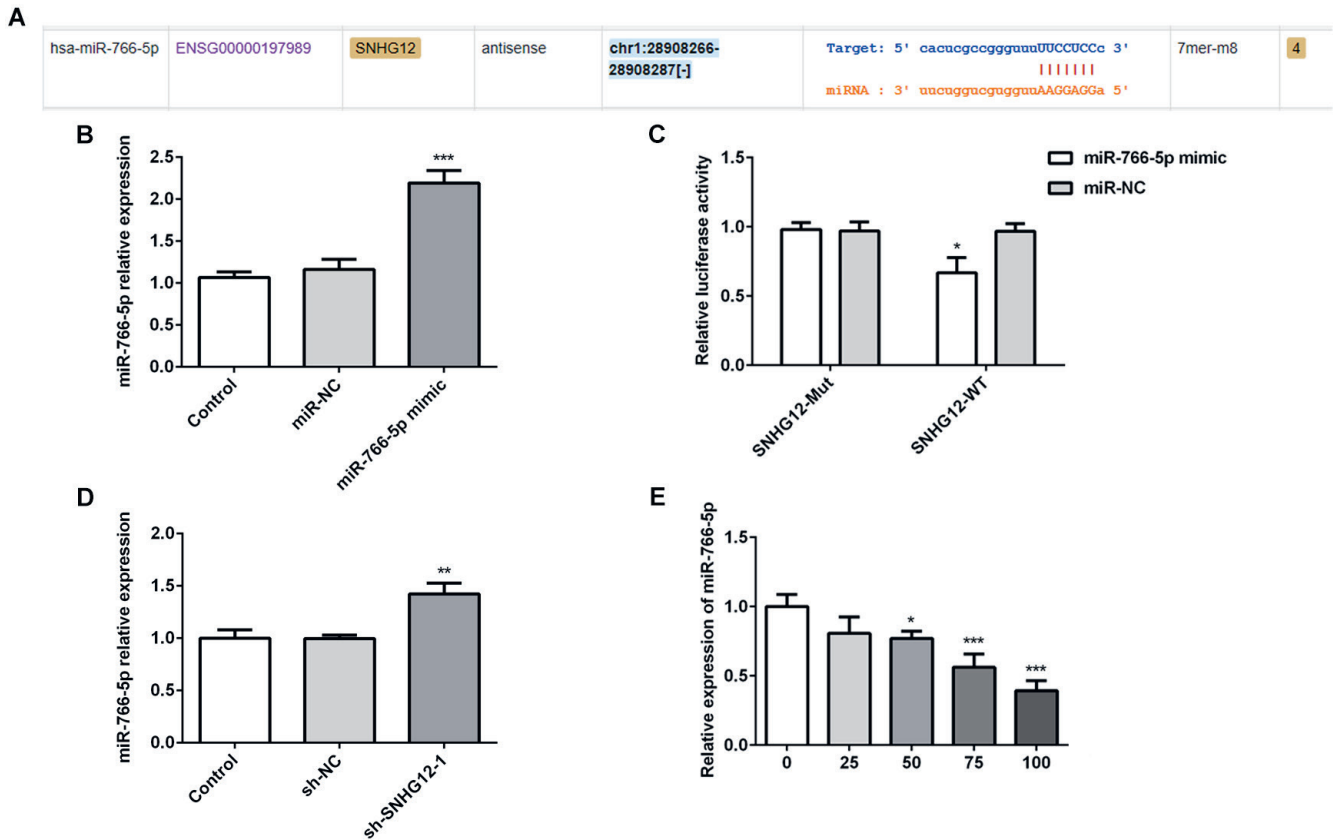
Fig. 2. *SNHG12* functions as a sponge of *miR-766-5p*

A. The potential binding sites were predicted using starBase v. 2.0; B. RT-qPCR was used to determine the expression of *miR-766-5p* in hVSMCs transfected with *miR-766-5p* mimic or miR-NC; ***p < 0.001 compared to miR-NC group; C. The interaction between *SNHG12* and *miR-766-5p* was validated using luciferase reporter gene assay; *p < 0.05 compared to miR-NC group; D. The expression of *miR-766-5p* in hVSMCs transfected with sh-SNHG12-1 or sh-NC; **p < 0.01 compared to the sh-NC group; E. RT-qPCR was used to determine the expression of *miR-766-5p* in hVSMCs exposed to ox-LDL (0 mg/L, 25 mg/L, 50 mg/L, 75 mg/L, 100 mg/L); *p < 0.05, ***p < 0.001 compared to 0 mg/L ox-LDL.
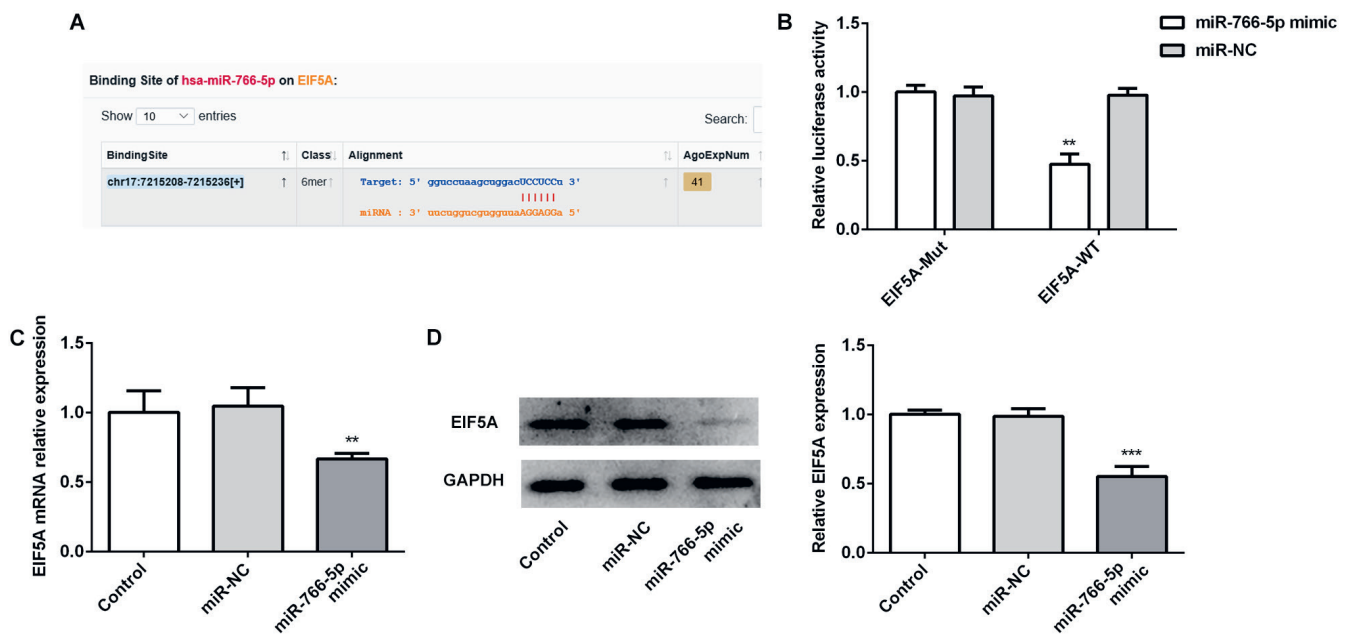


Fig. 3. *EIF5A* is target gene of *miR-766-5p*

A. The potential binding sites were predicted using starBase v. 2.0; B. The interaction between *miR-766-5p* and *EIF5A* was validated using luciferase reporter gene assay; **p < 0.01 compared to miR-NC group; C. RT-qPCR was used to determine the expression of *EIF5A* in hVSMCs transfected with *miR-766-5p* mimic or miR-NC; **p < 0.01 compared to the miR-NC group; D. western blotting was used to determine the protein levels of *EIF5A* in hVSMCs; ***p < 0.001 compared to the miR-NC group.
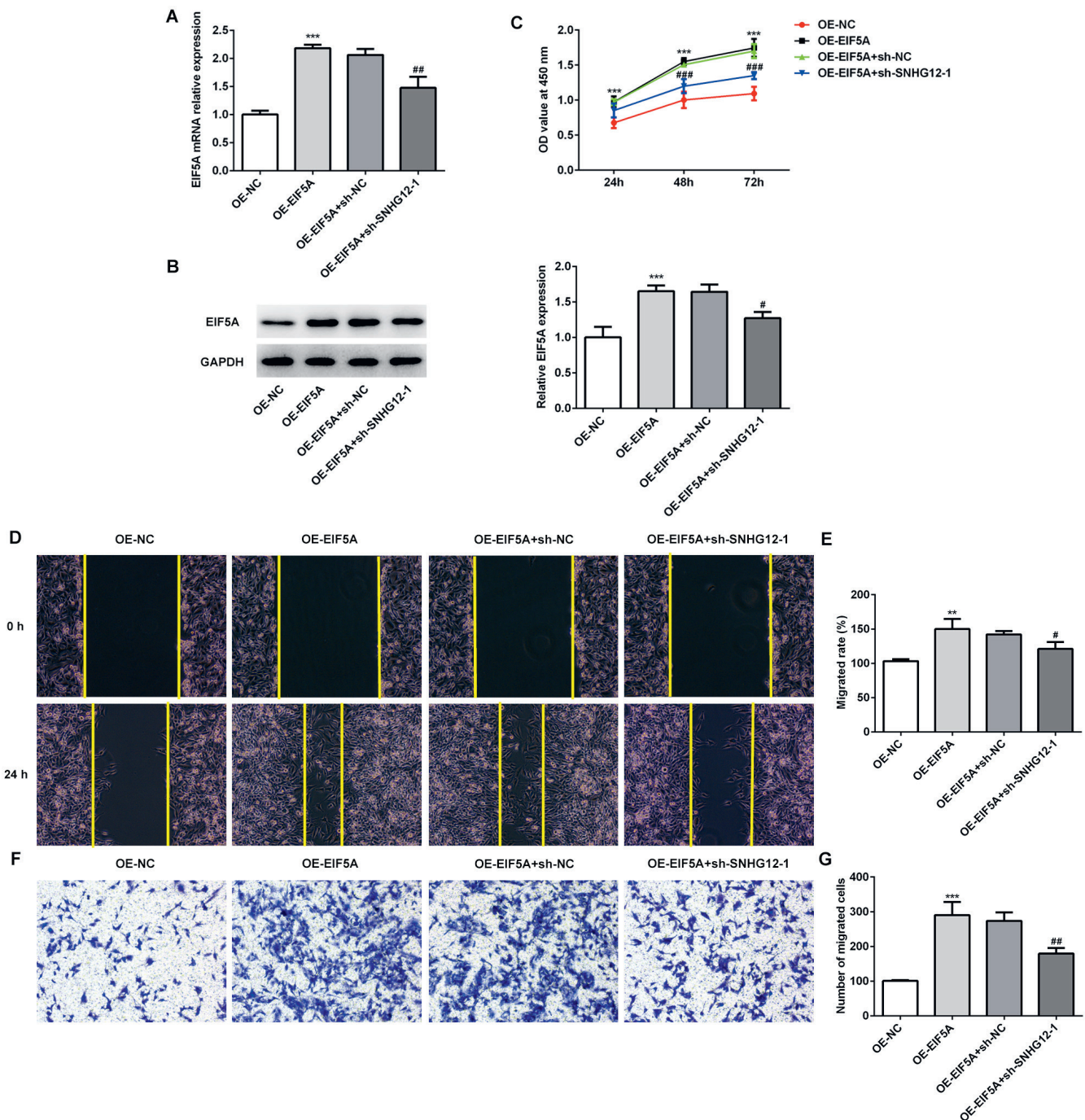
**Fig. 4.** *SNHG12* regulates the proliferation and migration of hVSMCs via mediation of *EIF5A*

A. The expression of *EIF5A* was examined using RT-qPCR; ***$p < 0.001$ compared to the OE-NC group; ##$p < 0.01$ compared to the OE-EIF5A+sh-NC group; B. western blot analysis was used to determine the protein levels of *EIF5A* in hVSMCs; ***$p < 0.001$ compared to the OE-NC group; #$p < 0.05$ compared to the OE-EIF5A+sh-NC group; C. The cell viability was estimated using CCK-8 assay; ***$p < 0.001$ compared to the OE-NC group; ###$p < 0.001$ compared to the OE-EIF5A+sh-NC group. The capability of cell migration was assessed using wound healing assay (D and E) and transwell migration assay (F and G); **$p < 0.01$, ***$p < 0.01$ compared to the control group; #$p < 0.05$, ##$p < 0.01$ compared to the ox-LDL+sh-NC group; ×100 magnification.

*SNHG12* knockdown exhibited an inhibition of cell migration (Fig. 4D,E). Consistently, transwell migration assays showed a similar result with that of the wound healing assay (Fig. 4F,G). Taken together, these results indicate that *SNHG12* mediated the migratory capacities of hVSMCs through regulating *EIF5A*.

## Discussion

In recent years, numerous studies have demonstrated that lncRNAs regulate various cellular process including cell proliferation, migration, invasion, and apoptosis.[24–26] It was reported that lncRNA MIAT activates the PI3K/Akt

signaling pathway, thereby exacerbating atherosclerotic damage in AS mice.[3] LncRNA activated by transforming growth factor (TGF) expression is significantly higher in AS patients compared with healthy patients, and it could enhance the expression of caspase-3 in human vascular endothelial cells (HUVECs).[27] Furthermore, the proliferation and migration of VSMCs were promoted by lncRNA 430945.[28]

The hVSMCs are the major cell type observed in blood vessel walls, and play a considerable role in the regulation of multiple physiological and pathological situations.[29] Aberrant proliferation and migration of VSMCs are key events in the progression of AS and restenosis after percutaneous coronary intervention.[30] A large amount of studies have suggested that ox-LDL exert a promotion effect in the development of AS by stimulating the proliferation of hVSMCs within the vessel wall; therefore, ox-LDL was widely used to stimulate hVSMCs for investigating the related mechanisms of AS.[31,32] Studies have implicated *SNHG12* in various cancers, and it functions as a potential candidate for cancer-directed interventions.[33,34] The altered expression of *SNHG12* is associated with cell viability, proliferation, metastasis, and invasion, thereby affecting the progression and diagnosis of cancer.[13] However, the function of *SNHG12* in AS has not yet been clearly elucidated. In this study, it was found that ox-LDL facilitated the expression of *SNHG12* in hVSMCs. Deletion of *SNHG12* impeded cell migration induced by ox-LDL.

Previous reports have described that lncRNAs interact with miRNA as ceRNAs and protect miRNAs from binding to and repressing target RNAs,[22,35] suggesting a complicated crosstalk among diverse RNA species. Accumulating reports have been made to understand the effect of miRNAs in VSMC biology, especially in cellular proliferation and migration.[36–38] In our study, luciferase reporter gene assays revealed an interplay between *SNHG12* and *miR-766-5p*, and *SNHG12* knockdown enhanced the expression of *miR-766-5p*. To further examine the target RNA regulated by lncRNA-miRNA, binding sites between *miR-766-5p* and *EIF5A* sequence were predicted using starBase v. 2.0. Subsequently, the interaction between *miR-766-5p* and *EIF5A* was further validated using luciferase reporter gene assay and RT-qPCR. Finally, we found that overexpression of *EIF5A* expedited the proliferation and migration of hVSMCs, whereas the effect was reversed by *SNHG12* silencing.

## Conclusions

The present study illustrates that *SNHG12* was highly expressed in ox-LDL-challenged hVSMCs. An intricate interplay among *SNHG12*, *miR-766-5p* and *EIF5A* was discovered, and all of these results indicated that *SNHG12*-knockdown inhibited the proliferation and migration of hVSMCs through targeting the *miR-766-5p/EIF5A* axis.

Further research is necessary for investigating the impact of *SNHG12/miR-766-5p/EIF5A* signaling pathway on other pathological alterations in AS progression.

The data supporting our findings are available from the corresponding author upon reasonable request.

### ORCID iDs

Wen Liu  https://orcid.org/0000-0003-0629-4305
Jianhuan Che  https://orcid.org/0000-0002-9764-8123
Yan Gu  https://orcid.org/0000-0003-3952-7611
Ling Song  https://orcid.org/0000-0002-3118-2906
Yingying Jiao  https://orcid.org/0000-0003-2704-5228
Shui Yu  https://orcid.org/0000-0003-1324-8745

### References

1. Geisler S, Coller J. RNA in unexpected places: Long non-coding RNA functions in diverse cellular contexts. *Nat Rev Mol Cell Biol*. 2013;14(11):699–712. doi:10.1038/nrm3679
2. Li S, Sun Y, Zhong L, et al. The suppression of ox-LDL-induced inflammatory cytokine release and apoptosis of HCAECs by long non-coding RNA-MALAT1 via regulating microRNA-155/SOCS1 pathway. *Nutr Metabol Cardiovasc Dis*. 2018;28(11):1175–1187. doi:10.1016/j.numecd.2018.06.017
3. Sun G, Li Y, Ji Z. Up-regulation of MIAT aggravates the atherosclerotic damage in atherosclerosis mice through the activation of PI3K/Akt signaling pathway. *Drug Deliv*. 2019;26(1):641–649. doi:10.1080/10717544.2019.1628116
4. Zhou T, Ding JW, Wang XA, Zheng XX. Long noncoding RNAs and atherosclerosis. *Atherosclerosis*. 2016;248:51–61. doi:10.1016/j.atherosclerosis.2016.02.025
5. Yao X, Yan C, Zhang L, Li Y, Wan Q. LncRNA ENST00113 promotes proliferation, survival, and migration by activating PI3K/Akt/mTOR signaling pathway in atherosclerosis. *Medicine (Baltimore)*. 2018;97(16):e0473. doi:10.1097/MD.0000000000010473
6. Turner AW, Wong D, Khan MD, Dreisbach CN, Palmore M, Miller CL. Multi-omics approaches to study long non-coding RNA function in atherosclerosis. *Front Cardiovasc Med*. 2019;6:9. doi:10.3389/fcvm.2019.00009
7. Yang H, Jiang Z, Wang S, et al. Long non-coding small nucleolar RNA host genes in digestive cancers. *Cancer Med*. 2019;8(18):7693–7704. doi:10.1002/cam4.2622
8. Jin XJ, Chen XJ, Zhang ZF, et al. Long noncoding RNA *SNHG12* promotes the progression of cervical cancer via modulating miR-125b/STAT3 axis. *J Cell Physiol*. 2019;234(5):6624–6632. doi:10.1002/jcp.27403
9. Cheng G, Song Z, Liu Y, et al. Long noncoding RNA *SNHG12* indicates the prognosis of prostate cancer and accelerates tumorigenesis via sponging miR-133b. *J Cell Physiol*. 2020;235(2):1235–1246. doi:10.1002/jcp.29039
10. Song J, Wu X, Ma R, Miao L, Xiong L, Zhao W. Long noncoding RNA *SNHG12* promotes cell proliferation and activates Wnt/beta-catenin signaling in prostate cancer through sponging microRNA-195. *J Cell Biochem*. 2019;120(8):13066–13075. doi:10.1002/jcb.28578
11. Zhang R, Liu Y, Liu H, et al. The long non-coding RNA *SNHG12* promotes gastric cancer by activating the phosphatidylinositol 3-kinase/AKT pathway. *Aging*. 2019;11(23):10902–10922. doi:10.18632/aging.102493
12. Wu Z, Chen D, Wang K, Cao C, Xu X. Long non-coding RNA *SNHG12* functions as a competing endogenous RNA to regulate MDM4 expression by sponging miR-129-5p in clear cell renal cell carcinoma. *Front Oncol*. 2019;9:1260. doi:10.3389/fonc.2019.01260
13. Tamang S, Acharya V, Roy D, et al. *SNHG12*: An LncRNA as a potential therapeutic target and biomarker for human cancer. *Front Oncol*. 2019;9:901. doi:10.3389/fonc.2019.00901
14. Long FQ, Su QJ, Zhou JX, et al. LncRNA *SNHG12* ameliorates brain microvascular endothelial cell injury by targeting miR-199a. *Neur Regen Res*. 2018;13(11):1919–1926. doi:10.4103/1673-5374.238717
15. Yu B, Wang S. Angio-LncRs: LncRNAs that regulate angiogenesis and vascular disease. *Theranostics*. 2018;8(13):3654–3675. doi:10.7150/thno.26024

16. Wu G, Cai J, Han Y, et al. LincRNA-p21 regulates neointima formation, vascular smooth muscle cell proliferation, apoptosis, and atherosclerosis by enhancing p53 activity. *Circulation*. 2014;130(17):1452–1465. doi:10.1161/CIRCULATIONAHA.114.011675

17. Wang S, Zhang X, Yuan Y, et al. BRG1 expression is increased in thoracic aortic aneurysms and regulates proliferation and apoptosis of vascular smooth muscle cells through the long non-coding RNA HIF1A-AS1 in vitro. *Eur J Cardiothorac Surg*. 2015;47(3):439–446. doi:10.1093/ejcts/ezu215

18. Pan JX. LncRNA H19 promotes atherosclerosis by regulating MAPK and NF-kB signaling pathway. *Eur Rev Med Pharmacol Sci*. 2017;21(2):322–328. PMID:28165553

19. Livak KJ, Schmittgen TD. Analysis of relative gene expression data using real-time quantitative PCR and the 2(−Delta Delta C(T)) method. *Methods*. 2001;25(4):402–408. doi:10.1006/meth.2001.1262

20. Cao C, Zhang T, Zhang D, et al. The long non-coding RNA, SNHG6-003, functions as a competing endogenous RNA to promote the progression of hepatocellular carcinoma. *Oncogene*. 2017;36(8):1112–1122. doi:10.1038/onc.2016.278

21. Jia B, Xia L, Cao F. The role of *miR-766-5p* in cell migration and invasion in colorectal cancer. *Exp Ther Med*. 2018;15(3):2569–2574. doi:10.3892/etm.2018.5716

22. Salmena L, Poliseno L, Tay Y, Kats L, Pandolfi PP. A ceRNA hypothesis: The Rosetta Stone of a hidden RNA language? *Cell*. 2011;146(3):353–358. doi:10.1016/j.cell.2011.07.014

23. Mathews MB, Hershey JW. The translation factor eIF5A and human cancer. *Biochim Biophys Acta*. 2015;1849(7):836–844. doi:10.1016/j.bbagrm.2015.05.002

24. Ballantyne MD, Pinel K, Dakin R, et al. Smooth muscle enriched long noncoding RNA (SMILR) regulates cell proliferation. *Circulation*. 2016;133(21):2050–2065. doi:10.1161/CIRCULATIONAHA.115.021019

25. Nai Y, Pan C, Hu X, Ma Y. LncRNA LUCAT1 contributes to cell proliferation and migration in human pancreatic ductal adenocarcinoma via sponging miR-539. *Cancer Med*. 2020;9(2):757–767. doi:10.1002/cam4.2724

26. Zhang S, Chen P, Huang Z, et al. Sirt7 promotes gastric cancer growth and inhibits apoptosis by epigenetically inhibiting miR-34a. *Sci Rep*. 2015;5:9787. doi:10.1038/srep09787

27. Yu H, Ma S, Sun L, Gao J, Zhao C. TGF-β1 upregulates the expression of lncRNA-ATB to promote atherosclerosis. *Mol Med Rep.* 2019;19(5):4222–4228. doi:10.3892/mmr.2019.10109

28. Cui C, Wang X, Shang XM, et al. lncRNA 430945 promotes the proliferation and migration of vascular smooth muscle cells via the ROR2/RhoA signaling pathway in atherosclerosis. *Mol Med Rep*. 2019;19(6):4663–4672. doi:10.3892/mmr.2019.10137

29. Eun SY, Ko YS, Park SW, Chang KC, Kim HJ. IL-1beta enhances vascular smooth muscle cell proliferation and migration via P2Y2 receptor-mediated RAGE expression and HMGB1 release. *Vascul Pharmacol*. 2015;72:108–117. doi:10.1016/j.vph.2015.04.013

30. Fan TF, He JH, Yin YQ, et al. Dioscin inhibits intimal hyperplasia in rat carotid artery balloon injury model through inhibition of the MAPK-FoxM1 pathway. *Eur J Pharmacol*. 2019;854:213–223. doi:10.1016/j.ejphar.2019.03.050

31. Pirillo A, Norata GD, Catapano AL. LOX-1, OxLDL, and atherosclerosis. *Mediators Inflamm*. 2013;2013:152786. doi:10.1155/2013/152786

32. Yang N, Dong B, Song YQ, et al. Downregulation of miR-637 promotes vascular smooth muscle cell proliferation and migration via regulation of insulin-like growth factor-2. *Cell Mol Biol Lett*. 2020;25:30. doi:10.1186/s11658-020-00222-z

33. Wang O, Yang F, Liu Y, et al. C-MYC-induced upregulation of lncRNA *SNHG12* regulates cell proliferation, apoptosis and migration in triple-negative breast cancer. *Am J Transl Res*. 2017;9(2):533–545. PMID:28337281

34. Zhang H, Lu W. LncRNA *SNHG12* regulates gastric cancer progression by acting as a molecular sponge of miR320. *Mol Med Rep*. 2018;17(2):2743–2749. doi:10.3892/mmr.2017.8143

35. Tay Y, Rinn J, Pandolfi PP. The multilayered complexity of ceRNA crosstalk and competition. *Nature*. 2014;505(7483):344–352. doi:10.1038/nature12986

36. Choe N, Kwon JS, Kim JR, et al. The microRNA miR-132 targets Lrrfip1 to block vascular smooth muscle cell proliferation and neointimal hyperplasia. *Atherosclerosis*. 2013;229(2):348–355. doi:10.1016/j.atherosclerosis.2013.05.009

37. Li FP, Lin DQ, Gao LY. LncRNA TUG1 promotes proliferation of vascular smooth muscle cell and atherosclerosis through regulating miRNA-21/PTEN axis. *Eur Rev Med Pharmacol Sci*. 2018;22(21):7439–7447. doi:10.26355/eurrev_201811_16284

38. Huang SC, Wang M, Wu WB, et al. Mir-22-3p inhibits arterial smooth muscle cell proliferation and migration and neointimal hyperplasia by targeting HMGB1 in arteriosclerosis obliterans. *Cell Physiol Biochem*. 2017;42(6):2492–2506. doi:10.1159/000480212

# Ginsenoside Rg1 induces senescence of leukemic stem cells by upregulating p16INK4a and downregulating hTERT expression

Yan-Long Tang[1,B–F], Xiao-Bo Wang[2,B–D,F], Yue Zhou[2,A–F], Ya-Ping Wang[3,B,C,F], Ji-Chao Ding[2,B,C,F]

[1] Department of Radiology, Affiliated Hospital of Dali University, China

[2] Department of Histology and Embryology, Dali University, China

[3] Department of Histology and Embryology, Chongqing Medical University, China

A – research concept and design; B – collection and/or assembly of data; C – data analysis and interpretation;
D – writing the article; E – critical revision of the article; F – final approval of the article

**Address for correspondence**
Yue Zhou
E-mail: zhouxille@yeah.net

**Conflict of interest**
None declared

## Abstract

**Background.** Leukemic stem cells (LSCs) play an important role in the pathogenesis of leukemia. This research attempted to clarify effects of the telomere system on ginsenoside Rg1-induced senescence of LSCs.

**Objectives.** This research attempted to clarify effects of the telomere system on ginsenoside Rg1-induced senescence of LSCs.

**Materials and methods.** $CD34^+CD38^-$ LSCs were isolated, sorted, and divided into a control group and a Rg1 group (treated with 40 μmol/L Rg1). Cell Counting Kit-8 (CCK-8) was used to evaluate cell proliferation, and flow cytometry was used to assess the cell cycle of $CD34^+CD38^-$ LSCs. The senescence-associated β-galactosidase (SA-β-Gal) staining and CFU-Mix assay were conducted to measure senescence of $CD34^+CD38^-$ LSCs. The mRNA transcription and protein expression of p16INK4a and human telomerase reverse transcriptase (hTERT) were determined using a real-time polymerase chain reaction (RT-PCR) and western blot assay, respectively.

**Results.** The Rg1 treatment significantly attenuated proliferative activity and decreased the proliferative index (PI) of $CD34^+CD38^-$ LSCs compared to those of the control group ($p < 0.05$). It remarkably increased positive SA-β-Gal staining rate, and suppressed formation of the CFU-Mix of $CD34^+CD38^-$ LSCs compared with those of the control group ($p < 0.05$). The Rg1 treatment markedly boosted telomere effector, p16INK4a, in $CD34^+CD38^-$ LSCs compared with that of control group ($p < 0.05$). Such treatment obviously reduced telomere regulator, hTERT, in $CD34^+CD38^-$ LSCs compared with the control group ($p < 0.05$).

**Conclusions.** Ginsenoside Rg1-induced senescence of $CD34^+CD38^-$ LSCs through upregulating p16INK4a and downregulating hTERT expression, both of which are associated with telomere systems. The present study would be beneficial for the treatment of leukemia by providing a promising strategy to induce senescence of $CD34^+CD38^-$ LSCs.

**Key words:** senescence, telomere, ginsenoside Rg1, leukemic stem cells

# Background

Leukemic stem cells (LSCs), important pathogenic factors of leukemia, play an important role in the initiation of leukemia.[1,2] The clinical recurrence or relapse of leukemia is correlated with decreased therapeutic response for LSCs.[3] Strong resistance of LSCs to traditional, cell cycle-dependent drugs, it leads to a poor therapeutic effect, easy recurrence and drug resistance.[4] Drug resistance has become a difficult problem in the treatment of leukemia.[5] Therefore, it will be a breakthrough in the treatment of leukemia to find drugs that can specifically target LSCs and effectively inhibit the proliferation of LSCs without damaging normal tissue cells.

Cell aging or senescence is closely related to a tumor and is considered to be one of the mechanisms of tumor self-inhibition.[6] Therefore, inducing tumor cell senescence is considered to be an effective way to treat cancer. The CD34+CD38− LSCs are the first identified LSCs; therefore, their inhibition might be beneficial to the cell senescence of tumor cells in leukemia patients.[7,8] Ginsenoside Rg1 (shorter: Rg1) is an important pharmacological active component of *Panax ginseng* and functions as an anti-tumor agent by promoting the proliferation of blood cells.[9] It can effectively promote the proliferation of normal hematopoietic stem/progenitor cells in the blood system and delay their aging.[10] Moreover, Rg1 can inhibit the proliferation and induce the senescence of leukemia K562 cells within an abnormal blood system.[11]

The human telomerase reverse transcriptase (hTERT) is an important catalytic component for regulating telomerase activity and, therefore, could be effective in inhibiting telomerase activity, thereby preventing the progression of the cell cycle, and suppressing tumor growth.[12,13] The p16INK4A is considered to be a cyclin-dependent kinase inhibitor illustrating many biological functions, such as inhibition of the cell cycle.[14,15] Therefore, we speculated that hTERT and p16INK4A might be involved in the aging or senescence of the LSC, and furthermore, participate in tumor growth.

# Objectives

In this study, Rg1 was applied to the CD34+CD38− LSCs, and the Rg1-induced targeted regulation and mechanism in CD34+CD38− LSCs were discussed. This study provides an experimental basis for the application of aging, promotes novel research methods in cancer treatment and provides new ideas for the research of leukemia balanced utilizing effective components of natural drugs.

# Materials and methods

## Experiment grouping

According to the previous study by our team,[1] the CD34+CD38− LSCs were successfully sorted and identified by staining with an allophycocyanine (APC)-labeled anti-CD38 antibody and a FITC-labeled anti-CD34 antibody. Therefore, the formerly sorted CD34+CD38− LSCs were used in this study.

In our present research, the CD34+CD38− LSCs were grouped into a control group and a Rg1 group (subdivided into 20 μmol/L, 40 μmol/L and 80 μmol/L groups). In the control group, the CD34+CD38− LSCs were cultured in the Iscove's modified Dulbecco's medium (IMDM; Gibco, Grand Island, USA) supplemented with 10% fetal bovine serum (FBS; Gibco) and 5% $CO_2$ at 37°C for 48 h. In the Rg1 group, the CD34+CD38− LSCs were cultured as those in the control group, but also treated with Rg1 (dissolved in dimethyl sulfoxide (DMSO)) for 48 h at final dosages of 20 μmol/L, 40 μmol/L and 80 μmol/L. Moreover, an equal volume of DMSO was also added to the cell medium of the control group. The ginsenoside Rg1, with purity of more than 95% (Cat. No. 060427), was purchased from Jinlin Hongjiu Biotech (Changchun, China).

## Measurement for proliferative activity with CCK-8 assay

The proliferative activity for the CD34+CD38− LSCs was measured with the Cell Counting Kit-8 (CCK-8) method using a commercial CCK-8 Kit (Cat. No. C0037; Beyotime, Shanghai, China), and introduced protocol of the manufacturer. In short, the density of cells was adjusted to $1 \times 10^8$ cells per well (96-well plates) and cultured for 48 h at conditions of 5% $CO_2$ and 37°C. Then, the above cells were incubated with the CCK-8 reagent at a final dosage of 20 μL/well for 2 h. Optical density (OD) values for the cells in 96-well plates were determined with a professional enzyme-linked immunosorbent assay (ELISA) reader (ELx808; Bio-Tek, Winooski, USA) at 450 nm. The cell proliferation inhibitive rate (%) calculation was described in our previous study.[1]

## Evaluation for cell cycle with flow cytometry assay

The CD34+CD38− LSCs were cultured, harvested, washed using phosphate-buffered saline (PBS), fixed with 70% ethanol (cold), and incubated with bovine pancreatic ribonuclease (1 mg/mL medium; Sigma-Aldrich, St. Louis, USA), as described in our previous study.[16] The CD34+CD38− LSCs were stained using propidium-iodide (with a dosage of 50 μg/mL) for 30 min in the dark, and then analyzed with a flow cytometer (FACS Aria IIU; Becton Dickinson Biosciences, Oxford, UK). Finally, the cell cycle was analyzed with the Multi-Cycle software (Phoenix, Tokyo, Japan).

## Colony formation assay

In the present study, the colony formation assay was carried out as described in previous studies, with some modifications.[1,17] Briefly, the $CD34^+CD38^-$ LSCs were seeded onto 96-well plates, cultured and incubated with methylcellulose (final concentration of 0.8%; Sigma-Aldrich) with 5% $CO_2$ at 37°C for 2 weeks. A total of 50 or more colony formation units (CFU) of cells were defined as 1 mixed CFU (CFU-Mix). The formed CFU-Mix was counted with a light microscope (BX51; Olympus Corp., Tokyo, Japan).

## Determination for senescence with SA-β-Gal staining

The senescence-associated β-galactosidase (SA-β-Gal) staining was conducted as reported in our previous study.[12] The SA-β-Gal staining was carried out according to the protocol of the SA-β-Gal Staining Kit (Cell Signaling Technology, Beverly, USA). In short, the cells were stained with the SA-β-Gal reagent, seeded on slices, and sealed using 70% glycerol (Sigma-Aldrich). Eventually, slices carrying 400 or more LSCs were selected, and the positive-staining LSCs were counted under the inverted microscope.

## Evaluation for p16[INK4a] and hTERT expression using western blot assay

Total protein in $CD34^+CD38^-$ LSCs was extracted with the protein lysate buffer (Applygen Tech. Inc., Beijing, China). Concentrations for the total proteins were evaluated using the BCA Protein Detection Kit (Cat. No. P0010S; Beyotime) according to the protocol of the manufacturer. The same dosage of proteins was separated with the SDS-PAGE and transferred onto a polyvinylidene difluoride (PVDF) membrane (Beyotime), and then incubated using 5% skimmed milk. The PVDF membrane was incubated with rabbit anti-human p16[INK4a] antibody (Cat. No. ab108349), rabbit anti-human hTERT antibody (Cat. No. ab32020) and rabbit anti-human GAPDH antibody (Cat. No. ab8245) at 4°C overnight. Subsequently, the PVDF membranes were washed using phosphate-buffered saline with Tween (PBST) buffer and incubated with the horseradish peroxidase (HRP)-conjugated goat anti-rabbit antibody (Cat. No. ab6721) at room temperature for 1.5 h. All of the above antibodies were purchased form Abcam (Cambridge, USA). The bands in the PVDF membranes were visualized using the enhanced ECL Western Blotting Substrate (Cat. No. 32106; Thermo Fisher Scientific, Rockford, USA) and analyzed with the Gel Imaging System GelDoc It TS2L (Bio-Rad, Hercules, USA).

## Evaluation for p16[INK4a] and hTERT mRNA transcription with RT-PCR assay

The cells were lysed using TRIzol solution, and total RNAs were extracted and reversely transcribed to the complementary DNA (cDNAs) under the following conditions: 42°C for 30 min, 99°C for 5 min and 5°C for 5 min. The mRNA transcriptions of p16[INK4a], hTERT and *GAPDH* were amplified using a real-time polymerase chain reaction (RT-PCR) assay, under the following conditions: 95°C for 2 min, 40 cycles of 95°C for 15 s, 60°C for 1 min, and termination at 72°C for 10 min. Here, the *GAPDH* was defined as the internal control for amplifying hTERT mRNA, and actin was defined as the internal control for amplifying p16[INK4a]. The primers for amplifying the above targeting genes are illustrated in Table 1. The RT-PCR data were analyzed with the previous reported $2^{-\Delta Ct}$ method.[18]

## Statistical analyses

Data are presented as mean ± standard deviation (SD) and analyzed using IBM SPSS v. 19.0 (IBM Corp., Armonk, USA). Data were analyzed using a one-way analysis of variance (ANOVA) test followed by Tukey's post hoc test for comparing the differences between the groups. A p-value less than 0.05 was defined as a statistically significant.

# Results

## Rg1 treatment attenuated proliferative activity of $CD34^+CD38^-$ LSCs

The CCK-8 assay findings showed that the Rg1 treatment (all dosages of 20 μmol/L, 40 μmol/L and 80 μmol/L) significantly attenuated the proliferative activity compared with the control group (Table 2, all $p < 0.05$). The inhibitive rates of $CD34^+CD38^-$ LSCs were increased with increases in Rg1 treatment concentrations, with an obvious Rg1 concentration-dependent manner. The condition

Table 1. The specific primers for the PCR assay

| Primers | Sense (5'-3') | Anti-sense (5'-3') | Length [bp] |
|---|---|---|---|
| p16[INK4a] | AAGACATCGTGCGATATTTGCG | TGAGCTGAAGCTATGCCCGTC | 121 |
| β-actin | TGACGTGGACATCCGCAAAG | CTGGAAGGTGGACAGCGAGG | 205 |
| hTERT | TTGGAATCAGACAGCACTTG | GTAGTCCATGTTCACAATCG | 155 |
| *GADPH* | AGATCCCTCCAAAATCAAGTGG | GGCAGAGATGATGACCCTTTT | 130 |

Table 2. Inhibiting rate of Rg1 on proliferation of CD34⁺CD38⁻ LSCs in vitro (±SD, n = 8)

| Groups | Dosage [μmol/L] | Inhibitive rate [%] | | |
|---|---|---|---|---|
| | | 24 h | 48 h | 72 h |
| Control | — | 1.57 ±0.24 | 5.68 ±0.36 | 12.47 ±1.21 |
| Rg1 | 20 | 13.63 ±1.02* | 24.16 ±1.21* | 31.44 ±2.02* |
| Rg1 | 40 | 28.13 ±1.44*,# | 52.01 ±2.14*,# | 62.47 ±2.03*,# |
| Rg1 | 80 | 38.76 ±2.01*,Δ | 64.46 ±3.12*,Δ | 76.04 ±0.92*,Δ |

*$p < 0.05$ compared to the control group; #$p < 0.05$ compared to the 20 μmol/L group; Δ$p < 0.05$ compared to the 40 μmol/L group.

Table 3. Effect of Rg1 on distribution of cell cycle to CD34⁺CD38⁻ LSCs (±SD, n = 8)

| Groups | Dosage [μmol/L] | $G_0/G_1$ phase [%] | $G_2/M$ phase [%] | S phase [%] | PI |
|---|---|---|---|---|---|
| Control | — | 70.35 ±5.02 | 17.24 ±2.12 | 12.41 ±1.35 | 29.65 ±1.06 |
| Rg1 | 40 | 86.89 ±4.32* | 6.12 ±1.03* | 6.99 ±1.06* | 13.11 ±1.17* |

*$p < 0.05$ compared to the control group.

of the 40 μmol/L Rg1 treatment for 48 h (with an inhibitive rate of 52.01%), demonstrated a half-proliferation inhibition. Therefore, the regimen of 40 μmol/L Rg1 for 48 h in treating CD34⁺CD38⁻ LSCs was used for the following experiments and tests (in the Rg1 group).

## Rg1 treatment decreased proliferative index (PI) of CD34⁺CD38⁻ LSCs

The cell cycle findings indicated that CD34⁺CD38⁻ LSCs in the G0/G1 phase were remarkably increased, and in the G2/M phase and S phase were significantly decreased in the Rg1 group compared with the control group (Table 3, all $p < 0.05$). Through calculating the cell amounts in G0/G1, G2/M and S phases, we found that the Rg1 treatment markedly decreased the proliferative index (PI) compared with the control group (Table 3, $p < 0.05$).

## Rg1 treatment raised positive SA-β-Gal staining rate of CD34⁺CD38⁻ LSCs

According to the SA-β-Gal staining images, there were obviously SA-β-Gal-stained CD34⁺CD38⁻ LSCs in the Rg1 group, with no obvious staining in the control group (Fig. 1A). The statistical analysis illustrated that the SA-β-Gal staining rate in the Rg1 group (44.74%) was significantly higher compared with the control group (12.03%) (Fig. 1B, $p < 0.05$).

## Rg1 treatment suppressed formation of CFU-Mix of CD34⁺CD38⁻ LSCs

As a marker for cell aging, CFU-Mix, is also observed in the CD34⁺CD38⁻ LSCs (Fig. 2A).[19] The results exhibited that the Rg1 treatment markedly suppressed the formation of the CFU-Mix of CD34⁺CD38⁻ LSCs compared with the control group (Fig. 2B, $p < 0.05$).
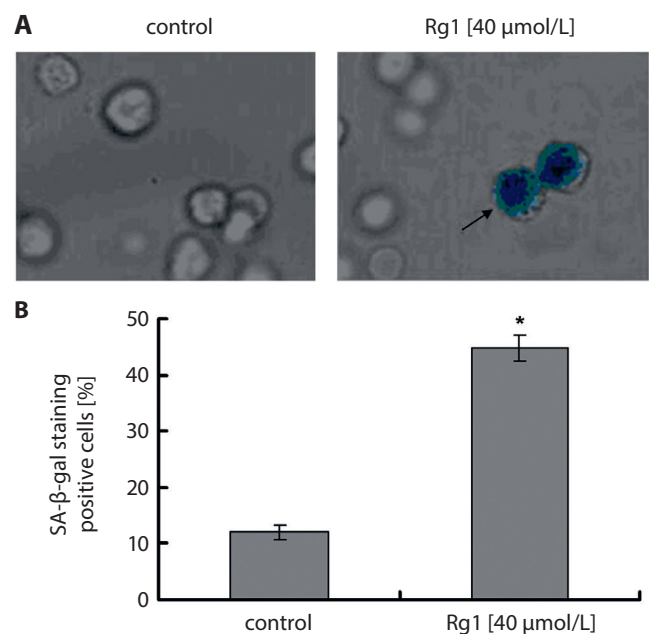


Fig. 1. SA-β-Gal staining for the CD34⁺CD38⁻ LSCs (± SD, n = 8). A. Negative SA-β-Gal staining of cells in control group; B. Positive SA-β-Gal staining of cells in Rg1 group. Black arrow represents the positive SA-β-Gal staining cells; ×400 magnification; *$p < 0.05$ compared to the control group

## Rg1 treatment boosted telomere effector, p16^INK4a, in CD34⁺CD38⁻ LSCs

The telomere damage system associated effector, p16^INK4a was also determined using both a RT-PCR assay (Fig. 3) and a western blot assay (Fig. 4A).[20] The findings showed that the Rg1 treatment obviously boosted both p16^INK4a mRNA transcription (Fig. 3) and p16^INK4a protein expression (Fig. 4B) in CD34⁺CD38⁻ LSCs compared with the control group ($p < 0.05$). These results suggest that CD34⁺CD38⁻ LSCs undergoing Rg1 treatment demonstrate obvious aging characteristics of stem cells.

**A**



**B**
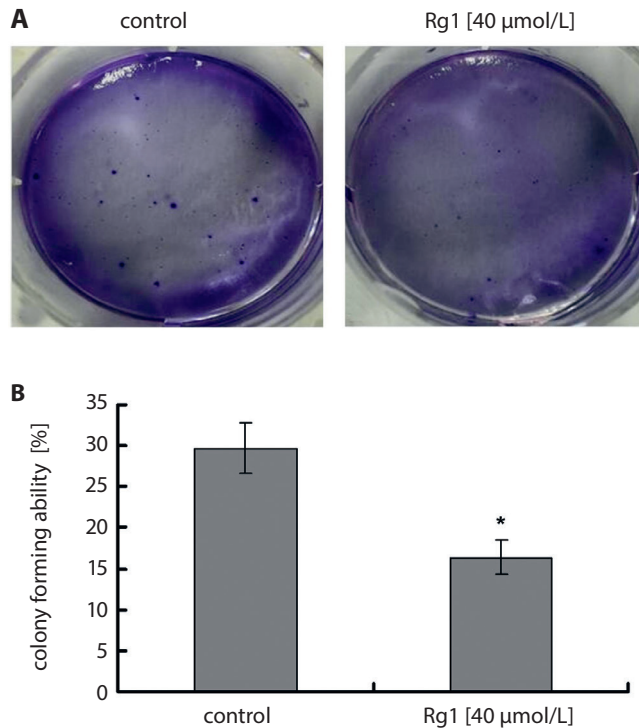


Fig. 2. Effects of Rg1 on the colony formation of CFU-Mix of CD34^{+}CD38^{−} LSCs (± SD, n = 8). A. CFU-Mix formation in control group; B. CFU-Mix formation in Rg1 group; *p < 0.05 compared to the control group
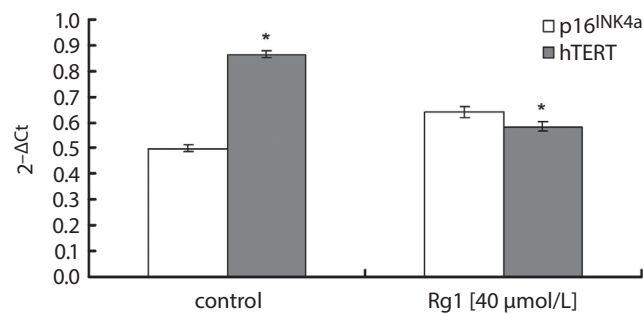


Fig. 3. Effects of the Rg1 on the p16[INK4a] mRNA transcription and hTERT mRNA transcription in CD34^{+}CD38^{−} LSCs (± SD, n = 8). The mRNA transcriptions were determined using the RT-PCR assay; *p < 0.05 compared to the control group

## Rg1 treatment reduced telomere regulatory biomarker, hTERT, in CD34^{+}CD38^{−} LSCs

The telomere regulatory biomarker, hTERT,[21] was evaluated using a RT-PCR (Fig. 3) and a western blot assay (Fig. 5A). As the results demonstrated, Rg1 treatment remarkably reduced the hTERT mRNA transcription (Fig. 3) and hTERT protein expression (Fig. 5B) when compared with the control group (p < 0.05). These results imply that CD34^{+}CD38^{−} LSCs undergoing Rg1 treatment indirectly attenuate telomere activity by reducing hTERT expression.

**A**



**B**
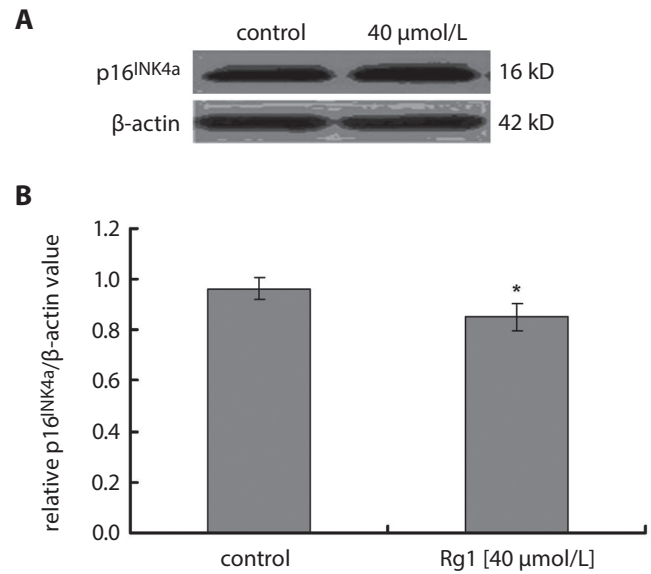


Fig. 4. Effects of Rg1 on the p16[INK4a] protein expression in CD34^{+}CD38^{−} LSCs (± SD, n = 8). A. Western blot image of the p16[INK4a] protein expression; B. Rg1 treatment increased p16[INK4a] protein expression; *p < 0.05 compared to the control group

**A**



**B**
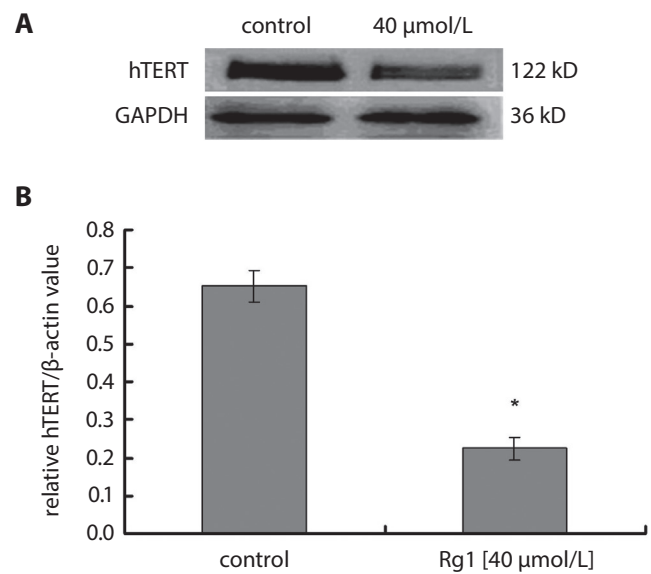


Fig. 5. Effects of Rg1 on the hTERT protein expression in CD34^{+}CD38^{−} LSCs (± SD, n = 8). A. Western blot image of the hTERT protein expression; B. Rg1 treatment decreased hTERT protein expression; *p < 0.05 compared to the control group

## Discussion

The LSCs have been proven as a risk factor for acute myeloid leukemia (AML) and are associated with chemotherapy resistance and relapse of disease.[22,23] Therefore, discovering a novel reagent or drug targeting LSCs might hold promise for the clinical treatment of AML. According to former studies,[24,25] Traditional Chinese medicine (TCM) normally demonstrates drug acceptance when applied in the disease therapy. Therefore, we speculated

that TCM might play a feasible role in treating the senescence of CD34+CD38− LSCs in certain signaling pathways.

Ginsenoside Rg1, in TCM, could benefit the Qi and nourish the blood, as described by Chinese medicine theory,[26] as well as protect against injury, aging and oxidants, and promote immunity, as described by modern medicine theory.[27] Many reports have documented and proved the anti-senescence function of Rg1 through different pathways, including activating the SIRT1/TSC2 signaling pathway,[1] the SIRT3/SOD2 signaling pathway[16] and the SIRT6/NF-kB signaling pathway,[15] all of which target CD34+CD38− LSCs. In this study, we clarified a novel signaling pathway that promotes the effects of Rg1 on senescence of CD34+CD38− LSCs.

We found that Rg1 treatment remarkably attenuated CD34+CD38− LSCs proliferation and obviously decreased proliferative index (PI) by modulating cell cycle, which is consistent with the findings of previous studies.[1,28] Therefore, the Rg1 significantly inhibits the proliferation and blocks the cell cycle of CD34+CD38− LSCs. The previous study[29] reported that SA-β-Gal staining could reflect the senescence of CD34+CD38− LSCs. Our results indicated that Rg1 treatment increased the positive SA-β-Gal staining rate of CD34+CD38− LSCs and suppressed the formation of the CFU-Mix of CD34+CD38− LSCs. These results suggest that Rg1 inhibits the CFU-Mix formation and senescence of CD34+CD38− LSCs, which is consistent with the previous study.[1]

The activation of the telomerase could protect against telomere damage by delaying the senescence of cells and mediating the apoptosis.[30] Therefore, the status of telomere might be correlated with the senescence of cells. The p16 plays a critical role in the telomere damage-associated senescence by limiting the apoptosis.[31] Meanwhile, the telomerase reverse transcriptase (TERT) modulates the telomere-associated senescence by triggering the DNA-damage response of cells.[32] Previous research[33,34] also documents that ginsenoside Rg1 could ameliorate proliferation of hematopoietic progenitor cells/hematopoietic stem cells (HPCs/HSCs) through reducing the expression of p16[INK4a]. Therefore, in the present study, expressions of both telomere damage system-associated effector (p16[INK4a])[20] and telomere regulatory biomarker (hTERT)[21] in CD34+CD38− LSCs administered with Rg1 were determined. Our findings illustrated that Rg1 treatment boosted p16[INK4a] expression and reduced hTERT expression in the CD34+CD38− LSCs. These results suggest that Rg1 triggers the senescence of CD34+CD38− LSCs via upregulating p16[INK4a] expression and downregulating hTERT expression.

## Limitations

In this study, whether ginsenoside Rg1 plays role in Rg1-triggered enhancive effects on CD34+CD38− LSCs growth have not been clarified, which is a limitation of this study.

## Conclusions

Our findings indicate that Rg1 could suppress proliferation and decrease the proliferative index of CD34+CD38− LSCs. Ginsenoside Rg1 demonstrated positive SA-β-Gal staining and inhibited formation of the CFU-Mix, both of which are indicators for senescence of cells. Also, Rg1 boosted p16[INK4a] expression and reduced hTERT expression in CD34+CD38− LSCs. In summary, ginsenoside Rg1 induces the senescence of CD34+CD38− LSCs through upregulating p16[INK4a] expression and downregulating hTERT expression, both of which are associated with the telomere system. The present study would be beneficial in the treatment of AML by providing a promising strategy to induce senescence of CD34+CD38− LSCs.

### ORCID iDs

Yan-Long Tang   https://orcid.org/0000-0002-3840-3353
Xiao-Bo Wang   https://orcid.org/0000-0002-7534-6503
Yue Zhou   https://orcid.org/0000-0002-5315-3639
Ya-Ping Wang   https://orcid.org/0000-0003-2712-6220
Ji-Chao Ding   https://orcid.org/0000-0002-9166-3330

### References

1. Tang YL, Zhang CG, Liu H, et al. Ginsenoside Rg1 inhibits cell proliferation and induces markers of cell senescence in CD34+CD38− leukemia stem cells derived from KG1-alpha acute myeloid leukemia cells by activating the Sirtuin 1 (SIRT1)/tuberous sclerosis complex 2 (TSC2) signaling pathway. *Med Sci Monit*. 2020;26:e918207. doi:10.12659/MSM.918207
2. Wawrzyniak-Dzierzek E, Gajek K, Slezak A, et al. Pediatric unmanipulated haploidentical hematopoietic stem cell transplantation with post-transplant cyclophosphamide and reduced intensity, TBI-free conditoning regimens in salvage transplantations. *Adv Clin Exp Med*. 2019;28(9):1223–1228. doi:10.17219/acem/104688
3. Siveen KS, Uddin S, Mohammad RM. Targeting acute myeloid leukemia stem cell signaling by natural products. *Mol Cancer*. 2017;16(1):13. doi:10.1186/s12943-016-0571-x
4. Riether C, Schurch CM, Flury C, et al. Tyrosine kinase inhibitor-induced CD70 expression mediates drug resistance in leukemia stem cells by activating Wnt signaling. *Sci Transl Med*. 2015;7(298):298ra119. doi:10.1126/scitranslmed.aab1740
5. Cucchi DGJ, Bachas C, van den Heuvel-Eibrink MM, et al. Harnessing gene expression profiles for the identification of ex vivo drug response genes in pediatric acute myeloid leukemia. *Cancers (Basel)*. 2020;12(5):E1247. doi:10.3390/cancers12051247
6. Hu X, Zhang H. Doxorubicin-induced cancer cell senescence shows a time delay effect and is inhibited by epithelial-mesenchymal transition (EMT). *Med Sci Monit*. 2019;25(1):3617–3623. doi:10.12659/MSM.914295
7. Strickland SA, Mohan SR, Savona MR. Unfavorable-risk acute myeloid leukemia dissected. *Curr Opin Hematol*. 2016;23(2):144–149. doi:10.1097/MOH.0000000000000225
8. Navarrete-Reyes AP, Soto-Perez-de-Celis E, Hurria A. Cancer and ageing: A complex biological association. *Rev Invest Clin*. 2016;68(1):17–24. PMID:27028173
9. Chu SF, Zhang JT. New achievements in ginseng research and its future prospects. *Chin J Integr Med*. 2009;15(6):403–408. doi:10.1007/s11655-009-0403-6
10. Chen C, Mu XY, Zhou Y, et al. Ginsenoside Rg1 enhances the resistance of hematopoietic stem/progenitor cells to radiation-induced aging in mice. *Acta Pharmacol Sin*. 2014;35(1):143–150. doi:10.1038/aps.2013.136
11. Chen X, Zhang J, Fang Y, Zhao C, Zhu Y. Ginsenoside Rg1 delays tert-butyl hydroperoxide-induced premature senescence in human WI-38 diploid fibroblast cells. *J Gerontol A Biol Sci Med Sci*. 2008;63(3):253–264. doi:10.1093/gerona/63.3.253

12. Cohen SB, Graham ME, Lovrecz GO, Bache N, Robinson PJ, Reddel RR. Protein composition of catalytically active human telomerase from immortal cells. *Science.* 2007;315(5820):1850–1853. doi:10.1126/science.1138596

13. George J, Banik NL, Ray SK. Knockdown of hTERT and concurrent treatment with interferon-gamma inhibited proliferation and invasion of human glioblastoma cell lines. *Int J Biochem Cell Biol.* 2010;42(7):1164–1173. doi:10.1016/j.biocel.2010.04.002

14. Zhang CY, Bao W, Wang LH. Downregulation of p16 (ink4a) inhibits cell proliferation and induces G1 cell cycle arrest in cervical cancer cells. *Int J Mol Med.* 2014;33(6):1577–1585. doi:10.3892/ijmm.2014.1731

15. Yang X, Sun Y, Li H, et al. C-terminal binding protein-2 promotes cells proliferation and migration in breast cancer via suppression of p16[INK4A]. *Oncotarget.* 2017;8(16):26154–26168. doi:10.18632/oncotarget.15402

16. Zhou Y, Wang YP, He YH, Ding JC. Ginsenoside Rg1 performs anti-aging functions by suppressing mitochondrial pathway-mediated apoptosis and activating sirtuin 3 (SIRT3)/superoxide dismutase 2 (SOD2) pathway in Sca-1+ HSC/HPC cells of an aging rat model. *Med Sci Monit.* 2020;26:e920666. doi:10.12659/MSM.920666

17. Xu B, Wang S, Li R, et al. Disulfiram/copper selectively eradicates AML leukemia stem cells in vitro and in vivo by simultaneous induction of ROS-JNK and inhibition of NF-kB and Nrf 2. *Cell Death Dis.* 2017;8:e2797. doi:10.1038/cddis.2017.176

18. Livak KJ, Schmittgen TD. Analysis of relative gene expression data using real-time quantitative PCR and the 2(–Delta Delta C(T)) method. *Methods.* 2001;25(2):402–408. doi:10.1006/meth.2001.1262

19. Tang YL, Zhou Y, Wang XP, Wang JW, Ding JC. SIRT6/NF-kB signaling axis in ginsenoside Rg1-delayed hematopoietic stem/progenitor cell senescence. *Int J Clin Exp Pathol.* 2015;8(5):5591–5596. PMID:26191269

20. Jacobs JJ, de Lange T. p16[INK4a] as a second effector of the telomere damage pathway. *Cell Cycle.* 2005;4(10):1364–1368. doi:10.4161/cc.4.10.2104

21. Yuan X, Xu D. Telomere reverse transcriptase (TERT) in action: Cross-talking with epigenetics. *Int J Mol Sci.* 2019;20(13):3338. doi:10.3390/ijms20133338

22. Gluexam T, Grandits AM, Schlerka A, et al. CGRP signaling via CALCRL increases chemotherapy resistance and stem cell properties in acute myeloid leukemia. *Int J Mol Sci.* 2019;20(23):5826. doi:10.3390/ijms20235826

23. Li H, Guo L, Jie S, et al. Berberine inhibits SDF-1-induced AML cells and leukemic stem cells migration via regulation of SDF-1 level in bone marrow stromal cells. *Biomed Pharmacother.* 2008;62(9):573–678. doi:10.1016/j.biopha.2008.08.003

24. Lou JS, Yao P, Tsim KWK. Cancer treatment by using traditional Chinese medicine: Probing acute compounds in anti-multidrug resistance during drug therapy. *Curr Med Chem.* 2018;25(38):5128–5141. doi:10.2174/0929867324666170920161922

25. Lin Z, Chen B, Wu T, Xu X. Highly tumorigenic diffuse large B cell lymphoma cells are produced by coculture with stromal cells. *Acta Haematol.* 2018;139(4):201–216. doi:10.1159/000488385

26. Qi R, Jiang R, Xiao H, et al. Ginsenoside Rg1 protects against d-galactose induced fatty liver disease in a mouse model via FOXO1 transcription factor. *Life Sci.* 2020;254(1):117776. doi:10.1016/j.lfs.2020.117776

27. Xiong W, Li J, Jiang R, Li D, Liu Z, Chen D. Research on the effect of ginseng polysaccharide on apoptosis and cell cycle of human leukemia cell line K562 and its molecular mechanisms. *Exp Ther Med.* 2017;13(3):924–934. doi:10.3892/etm.2017.4087

28. Lahiani MH, Eassa S, Parnell C, et al. Carbon nanotubes as carriers of Panax ginseng metabolites and enhancers of ginsenosides Rb 1 and Rg1 anti-cancer activity. *Nanotechnology.* 2017;28(1):015101. doi:10.1088/0957-4484/28/1/015101

29. Tominaga T, Shimada R, Okada Y, Kawamata T, Kibayashi K. Senescence-associated-beta-galactosidase staining following traumatic brain injury in the mouse cerebrum. *PLoS One.* 2019;14(3):e0213673. doi:10.1371/journal.pone.0213673

30. Panneer Selvam S, Roth BM, Nganga R, et al. Balance between senescence and apoptosis is regulated by telomere damage-induced association between p16 and caspase-3. *J Biol Chem.* 2018;293(25):9784–9800. doi:10.1074/jbc.RA118.003506

31. Lou C, Deng A, Zheng H, et al. Pinitol suppresses TNF-alpha-induced chondrocyte senescence. *Cytokine.* 2020;130:155047. doi:10.1016/j.cyto.2020.155047

32. Ling X, Yang W, Zou P, et al. TERT regulates telomere-related senescence and apoptosis through DNA damage response in male germ cells exposed to BPDE in vitro and to B[a]P in vivo. *Environ Pollut.* 2018;235:836–849. doi:10.1016/j.envpol.2017.12.099

33. Wang ZL, Chen LB, Qiu Z, et al. Ginsenoside Rg1 ameliorates testicular senescence changes in D gal induced aging mice via anti-inflammatory and antioxidative mechanisms. *Mol Med Rep.* 2018;17:6269–6276. doi:10.3892/mmr.2018.8659

34. Cai SZ, Zhou Y, Liu J, et al. Alleviation of ginsenoside Rg1 on hematopoietic homeostasis defects caused by lead-acetate. *Biomed Pharmacother.* 2018;97:1204–1211. doi:10.1016/j.biopha.2017.10.148

# EGCG decreases myocardial infarction in both I/R and MIRI rats through reducing intracellular Ca$^{2+}$ and increasing TnT levels in cardiomyocytes

Qingxian Tu[B–D,F], Qianfeng Jiang[A–C,E,F], Min Xu[B,C,E,F], Yang Jiao[B,C,E,F], Huishan He[B,C,F], Shajin He[B,F], Weijin Zheng[B,F]

Department of Cardiovascular Medicine, The Third Affiliated Hospital of Zunyi Medical University (The First People's Hospital of Zunyi), China

A – research concept and design; B – collection and/or assembly of data; C – data analysis and interpretation;
D – writing the article; E – critical revision of the article; F – final approval of the article

**Address for correspondence**
Qianfeng Jiang
E-mail: yuupingwang@sina.com

## Abstract

**Background.** Myocardial ischemia/reperfusion injury (MIRI) usually induces serious health problems.

**Objectives.** This study attempted to explore protective effects of (—)-epigallocatechin-3-gallate (EGCG) on MIRI and the associated mechanism.

**Materials and methods.** Ischemia/reperfusion of an isolated rat heart (I/R model) and the MIRI model were used in this study. Myocardial infarction was measured with staining with 2,3,5-triphenyltetrazolium chloride (TTC). Ca$^{2+}$ and troponin T (TnT) concentrations in coronary perfusion fluid were evaluated using the chromatometry method. Ca$^{2+}$ concentration in cardiomyocytes was determined with detecting Ca$^{2+}$ fluorescence intensity. The ultrastructure of cardiomyocytes was observed using transmission electron microscopy (TEM). β-nicotinamide adenine dinucleotide (NAD$^+$) of cardiomyocytes was also determined.

**Results.** The EGCG (I/R+EGCG) significantly reduced myocardial infarction size of isolated rat heart compared to I/R rats (p < 0.05), remarkably increased Ca$^{2+}$ and decreased TnT concentrations in coronary perfusion fluid of I/R rats compared to the I/R model (p < 0.05), as well as markedly decreased intracellular Ca$^{2+}$ concentration and promoted NAD$^+$ concentration in cardiomyocytes compared to I/R rats (p < 0.05). It also obviously maintained the mitochondrial structure in cardiomyocytes of I/R rats and improved the ultrastructure of cardiomyocytes of MIRI rats. Lonidamine (LND) treatment (I/R+EGCG+LND group) significantly blocked the effects of EGCG on I/R injury compared to the I/R+EGCG group (p < 0.05). The EGCG (MIRI+EGCG) significantly decreased myocardial infarction size compared to MIRI rats (p < 0.05) and remarkably enhanced Ca$^{2+}$ and reduced TnT concentrations in the pulmonary artery compared to that of MIRI rats (p < 0.05).

**Conclusions.** The EGCG decreased myocardial infarction size in both I/R models and MIRI models by reducing intracellular Ca$^{2+}$ concentration, increasing TnT concentration, promoting NAD$^+$ concentration, and improving the ultrastructure of cardiomyocytes.

**Key words:** myocardial infarction, protective effect, cardiomyocytes, EGCG, myocardial ischemia/reperfusion injury

608

Q. Tu et al. EGCG reduces myocardial I/R of MIRI rats

# Background

Myocardial ischemia/reperfusion injury (MIRI) caused by cardiac surgery or myocardial infarction usually induces serious health problems.[1,2] It commonly accompanies coronary heart disorder and has been proven to be a leading factor for heart failure clinically.[3,4] It may also aggravate myocardial dysfunction and induce damage of cardiac cells, causing an overload of calcium, cell apoptosis and inflammatory response in heart tissues.[5] At present, there are many proven risk factors for MIRI, such as excess of reactive oxygen species (ROS) and release of inflammation-associated cytokines or factors, all of which eventually induce cardiomyocyte death resulting in damage to myocardial functions.[6,7] Although plenty of research[8,9] has reported strategies for preventing MIRI and decreasing myocardial infarct size, the clinical outcomes or efficacy for animal models are still unsatisfactory. Therefore, it is critical to discover a promising strategy for preventing MIRI with clinical applications.

# Objectives

The (–)-epigallocatechin-3-gallate (EGCG) is an important bioactive ingredient derived from green tea, which has anti-oxidant and free radical scavenging properties.[10,11] Previous studies[10,12] have reported that EGCG plays a series of cardiovascular protective roles, including alleviating heart ischemia/reperfusion (I/R) injury, reducing myocardial ischemia associated dysfunction of the heart, and protecting cardiac muscle of ischemic heart in vivo and in vitro. Kim et al.[13] reported that EGCG modulated $Ca^{2+}$ influx by eliciting extracellular $Ca^{2+}$ in cells. The present study attempted to determine the protective effects of EGCG on I/R injury of the heart and clarify whether $Ca^{2+}$ influx is involved in the protective effect of EGCG.

# Materials and methods

## Animals

Twenty-four specific pathology-free (SPF) rats weighing 230 ±20 g were provided by the Experimental Animal Department of Zunyi Medical College, China. All rats had free access to water and food and were housed at 25°C with a light/dark cycle of 12 h/12 h. All of the animal experiments or tests complied with the National Institutes of Health (NIH) Guidelines for Usage of Laboratory Animals revised in 1996. This study was approved by the Ethical Committee of The Third Affiliated Hospital of Zunyi Medical University (The First People's Hospital of Zunyi), China.

## Ischemia/reperfusion model of isolated rat heart (I/R model)

The ischemia/reperfusion model of isolated rat heart (I/R model) of isolated rat heart was generated as previously described,[14] with some modifications. Twelve Sprague Dawley rats were anesthetized by intraperitoneal injection with pentobarbital sodium (50 mg/kg body weight) and treated with heparin (3000 U/kg body weight) to establish the I/R model. Post-anesthesia, the anterior abdominal wall, diaphragm, and chest were fully cut open to expose the heart. About 5–6 mm remote from the beginning of the aorta, the aorta and the other blood vessels were cut off, and the heart was quickly harvested and pre-cooled at 4°C in KH buffer. Next, the heart was suspended on a Langendorff system through the aortic cannula and fixed with wires. A mixture of 95% $O_2$ and 5% $CO_2$ (37°C) was continuously injected into the KH buffer and the heart was perfused at a constant rate of 8 mL/min in a non-circular manner. A small incision was made above the left auricle, and a latex balloon connected to the multi-channel physiological recorder was inserted into the left ventricle through the left atrium and mitral valve. The end diastolic pressure of the left ventricle was adjusted between 8 mm Hg and 12 mm Hg. For the whole process, the volume of the balloon was kept constant. The whole operation, starting from the heart in vitro to the beginning of perfusion, should be completed within 1 min. Attention is needed to prevent air and tissue fragments from entering the coronary artery and causing embolism. The heart started beating a few seconds after perfusion began. The KH buffer was used to balance perfusion for 15 min, and treatment was then performed according to the trial grouping scheme described in the Trial groups and drug regimen subsection. Finally, the heart was ischemic for 30 min and reperfused for 120 min.

## MIRI rat model

The MIRI rat model was created as described in a previous study[15] with a few modifications. In brief, a total of 6 Sprague Dawley rats were anesthetized by intraperitoneal injection with pentobarbital sodium (50 mg/kg body weight), intubated using 16-gauge cannulas and connected to ventilators (Zhenghua Bio. Tech., Anhui, China). The MIRI was generated by carrying out coronary artery ligation. Through the left thoracotomy, the heart of the rat was fully exposed to demonstrate the left anterior descending (LAD) coronary artery, which was then ligated for 30 min and followed by 120 min of reperfusion.

## Trial groups and drug regimen

There were 3 groups of rats in this study: 12 I/R rats, 6 MIRI rats and 6 control (or sham) rats (a total of 24 rats).

The I/R rats were subdivided into an I/R group (n = 3), I/R+EGCG group (n = 3; I/R rats were perfused with 10 mg

of EGCG for 30 min, induced to global ischemia for 30 min and reperfused for 120 min), I/R+lonidamine (LND) group (n = 3; I/R rats were induced to global ischemia for 30 min, perfused with 30 μM LND for 30 min and reperfused for 120 min), and I/R+EGCG+LND group (n = 3; I/R rats were perfused with 10 mg of EGCG for 30 min, induced to global ischemia for 30 min, perfused with 30 μM LND for 20 min, and reperfused for 120 min).

The MIRI rats were divided into a MIRI group (n = 3; as described above) and MIRI+EGCG group (n = 3; 30 min before MIRI modeling, the femoral vein was injected with EGCG at a dosage of 10 mg/kg body weight).

The control group was also divided into 2 subgroups. Three rats control group rats were perfused with KH buffer, while 3 other were perfused with normal saline.

## Measurement of myocardial infarction

Hearts of the rats were rapidly injected with 1% 2,3,5-triphenyltetrazolium chloride (TTC; Sigma-Aldrich, St. Louis, USA; pH 7.4) at 120 min of reperfusion and then stained for 15 min in a 37°C water bath in the dark. At the end of staining, the dye was stopped by washing with distilled water and then the heart was refrigerated at –20°C for 20 min. After fixation, the heart was cut into sections of a 1–2-millimeter thickness. The myocardial infarction area appeared grayish white, while the non-myocardial infarction area was dark red. Finally, myocardial infarction was analyzed using Image Pro-Plus v. 6.0 image analysis software (Media Cybernetics Inc., Bethesda, USA). Myocardial infarction in the rats was represented as the ratio of infarct area (IA)/ischemic area at risk (AAR).

## Evaluation of $Ca^{2+}$ and troponin T concentrations in coronary perfusion fluid

The $Ca^{2+}$ and troponin T (TnT) concentrations in coronary perfusion fluid were evaluated using the chromatometry method in this study. A total of 1 mL of coronary perfusion fluid of the rats in each group was collected, treated with anticoagulant, and centrifuged at 4°C and 1000 rpm for 8 min. The isolated serum was stored at –70°C until the experiment. The $Ca^{2+}$ concentration in coronary perfusion fluid was examined using the calcium colorimetric assay kit (Cat. No. K380-250; BioVision, Milpitas, USA) as instructed by the manufacturer. The TnT concentration in coronary perfusion fluid was examined using the TnT assay kit (Cat. No. 48T/96T; RapidBio, Calabasas, USA) according to the protocol of the manufacturer.

## Determination of $Ca^{2+}$ concentration in cardiomyocytes

Cardiomyocytes were obtained by homogenizing the heart tissues. After culture of the cardiomyocytes, the medium was removed and washed with Hank's balanced salt solution (HBSS; Gibco, Grand Island, USA). Cardiomyocytes were incubated with Fluo-4/AM (at a concentration of 20 μM; Cat. No. S1060; Beyotime, Shanghai, China) and Pluronic F-127 (at a concentration of 1 μM; Cat. No. ST501; Beyotime) at 37°C for 20 min. Next, cells were washed twice with phosphate-buffered saline (PBS) and cultured for 20–30 min again to confirm that Fluo-4/AM was completely transformed into Fluo-4. The green fluorescence intensity of the cardiomyocytes was detected using laser scanning confocal microscopy (ELX800; Bio-Tek Inc., Winooski, USA). A total of 25 cardiomyocytes were randomly selected as the regions of interest (ROIs). The green fluorescence intensity was analyzed using Las AF software (Leica, Wetzlar, Germany) to evaluate the change in intracellular calcium concentration. The fluorescence intensity of the cardiomyocytes in the control group was assigned a value of 100%. The $Ca^{2+}$ fluorescence intensity in each experimental group was represented as the percentage of the fluorescence intensity of cardiomyocytes.

## Measurement of $NAD^+$

The $NAD^+$ was measured using the commercial $NAD^+$/NADH cell-based assay kit (Cat. No. 600480-1; Cayman Chemical, Ann Arbor, USA) as instructed by the manufacturer. In brief, heart was homogenized using the $NAD^+$ extraction buffer (at a concentration of 100 μL/5 mg heart tissues). The resulting heart extracts were incubated in a 60°C water bath for 5 min, treated with NADH extraction buffer (100 μL) and then centrifuged for 5 min at 12,000 rpm. The supernatants were subsequently mixed with the cell-based assay alcohol dehydrogenase and cell-based assay $NAD^+$ diaphorase. The optical density at a wavelength of 565 nm was measured and recorded at 0 min (OD0) and 15 min (OD15) using a spectrophotometer. The standard curve was drawn and the content of $NAD^+$ was analyzed. The $NAD^+$ concentration was calculated using the following formula: $NAD^+$ (nM) = [(corrected absorbance-(y-intercept))/slope].

## Transmission electron microscopy (TEM)

The cardiomyocytes were fixed using 2.5% glutaraldehyde (Cat. No. G5882; Sigma-Aldrich) at 4°C for 2 h and 1% osmium tetrachloride (Cat. No. S837067; Sigma-Aldrich) at 4°C for 25–30 min, and then washed using PBS 2 times (10 min each time). Subsequently, the cardiomyocytes were dehydrated using a graded series of acetone solutions (50% acetone 1 time, 70% acetone 1 time, 90% acetone 2 times, and 100% acetone 3 times, 12 min per time), cleared in propylene oxide solution, embedded in 3–4 mL of acetone-EPON812-embedding agent for 30 min, and then in pure-embedding agent for 2 h for complete embedding. The embedded samples were baked at 60°C for 24 h to obtain the embedded hard blocks, which were

then cut into sections with a thickness of 1 µm and dried. The sections were stained using methylene blue dye solution (Cat. No. M9140; Sigma-Aldrich) at 60°C for 30 s and then complex dye solution (0.25% sodium borate : 0.5% basic fuchsin = 1 : 1) for 10 s. Subsequently, the sections were re-cut into ultra-thin sections with a thickness of 50 nm. The ultra-thin sections were laid onto 0.45% Formvar pretreated copper grids and stained with uranyl acetate dye solution for 10 min and lead dye solution for 12 min at room temperature. Finally, the ultra-thin sections were observed under a Philips TECNAI-10 transmission electron microscope (TEM; Philips, Amsterdam, the Netherlands).

## Statistical analyses

Data are reported as mean ± standard deviation (SD) and analyzed using IBM SPSS software v. 20.0 (IBM Corp., Armonk, USA). Differences between data were analyzed using analysis of variance (ANOVA) with the Bonferroni post hoc test. A p-value <0.05 indicated statistically significant differences.

# Results

## EGCG reduced myocardial infarction size of the I/R model of isolated rat heart

Myocardial infarction was determined in the I/R model of isolated rat heart (Fig. 1A). The results indicated that the myocardial infarction size of the I/R group was significantly increased compared to the control group (p = 0.000). We found that EGCG treatment (I/R+EGCG group) remarkably reduced the myocardial infarction size compared to the I/R group (Fig. 1B, p = 0.001). Furthermore, LND treatment (I/R+EGCG+LND group) blocked the reductive effects of EGCG (I/R+EGCG group) on myocardial infarction size of the I/R model of isolated rat heart (Fig. 1B, p = 0.003).

## EGCG increased $Ca^{2+}$ and decreased TnT concentrations in the coronary perfusion fluid of I/R rats

The results showed that the $Ca^{2+}$ concentration of the I/R group was significantly lower than in the control group (Fig. 2A, p = 0.000). However, EGCG treatment (I/R+EGCG group) remarkably increased $Ca^{2+}$ concentration compared with the I/R group (Fig. 2A, p = 0.000). The LND treatment (I/R+EGCG+LND group) significantly decreased $Ca^{2+}$ concentration compared to the I/R+EGCG group (Fig. 2A, both p = 0.000).

At the same time, TnT concentration for the I/R group was significantly higher compared to the control group (Fig. 2B, p = 0.000). However, EGCG treatment (I/R+EGCG group) significantly decreased TnT concentration compared with the I/R group (Fig. 2B, p = 0.000). The LND+EGCG treatment (I/R+EGCG+LND group) significantly increased TnT concentration compared to the I/R+EGCG group (Fig. 2B, both p = 0.000).
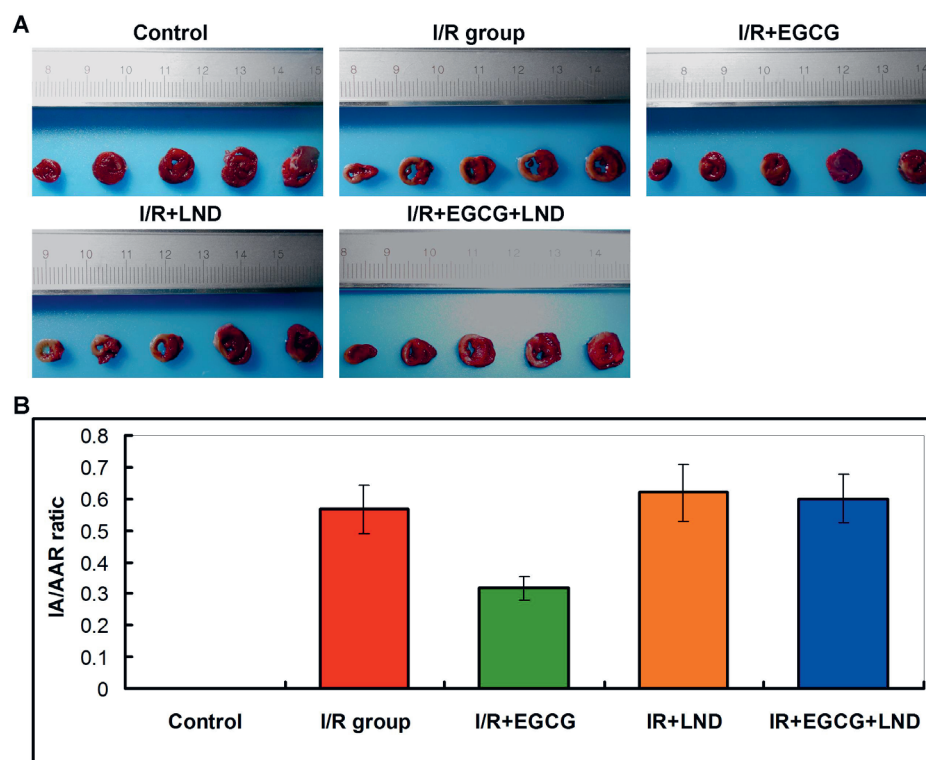


Fig. 1. Effects of EGCG treatment on myocardial infarction in the I/R model of isolated rat heart. A. Images of myocardial infarction in I/R rats undergoing EGCG and/or LDN treatment; B. Determination of the effects of EGCG and/or LDN treatment on myocardial infarction size (IA/AAR ratio) according to statistical analysis. For the I/R group compared to the control group p = 0.000; for the I/R+EGCG group compared to the I/R group p = 0.001; for the I/R+EGCG+LND group compared to the I/R+EGCG group p = 0.003

**A**

**B**
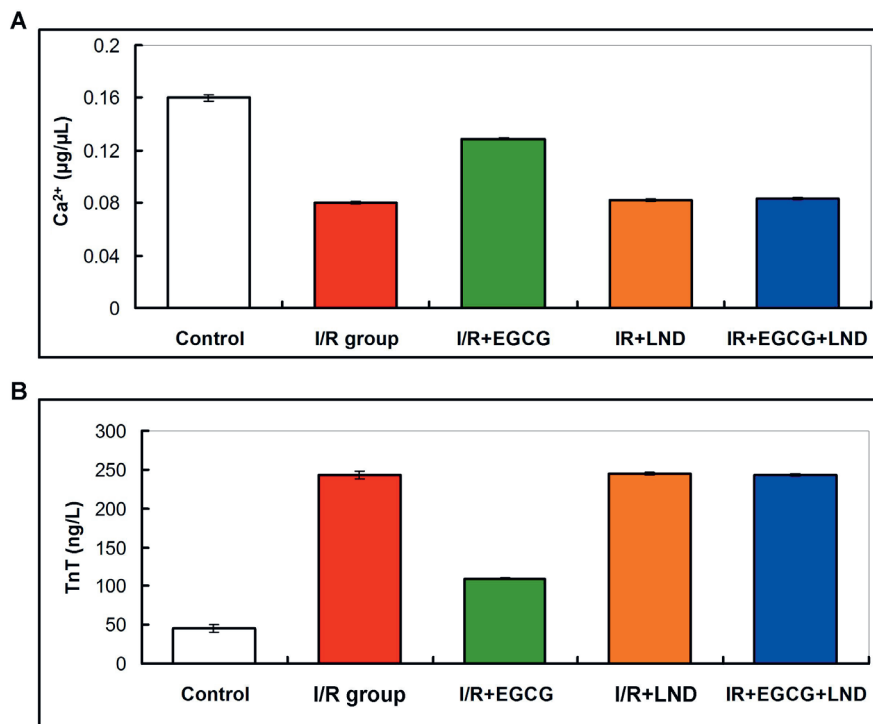
Fig. 2. Enhancive effects of EGCG on $Ca^{2+}$ concentration and reductive effects of EGCG on TnT concentration in the coronary perfusion fluid of I/R rats. A. EGCG treatment enhanced $Ca^{2+}$ concentration in I/R rats. For the I/R group compared to the control group p = 0.000; for the I/R+EGCG group compared to the I/R group p = 0.000; for the I/R+EGCG+LND group compared to the I/R+EGCG group p = 0.000; B. EGCG treatment decreased TnT concentration in I/R rats. For the I/R group compared to the control group p = 0.000; for the I/R+EGCG group compared to the I/R group p = 0.000; for the I/R+EGCG+LND group compared to the I/R+EGCG group p = 0.000

## EGCG decreased intracellular $Ca^{2+}$ concentration in cardiomyocytes of I/R rats

Intracellular $Ca^{2+}$ in cardiomyocytes was evaluated using green fluorescence staining in this study (Fig. 3A). The fluorescence findings showed that the intracellular $Ca^{2+}$ concentration in cardiomyocytes of the I/R group was significantly increased compared with the control group (Fig. 3B, p = 0.000), but decreased in the EGCG treatment group (I/R+EGCG group) compared with the I/R group (Fig. 3B, p = 0.000). The LND treatment (I/R+LND group) also increased $Ca^{2+}$ concentration compared with the I/R group (Fig. 3B, p = 0.000). In addition, LND+EGCG treatment (I/R+EGCG+LND group) significantly increased $Ca^{2+}$ concentration compared to the I/R+EGCG group (Fig. 3B, p = 0.000).

## EGCG promoted $NAD^+$ concentration in the cardiomyocytes of I/R rats

According to the $NAD^+$ measurement findings, rats in the control group exhibited the highest concentration of $NAD^+$ (Fig. 4). The $NAD^+$ concentration in the I/R+EGCG group was significantly higher than the I/R group (Fig. 4, p = 0.003). The LND treatment (I/R+LND group) slightly increased $NAD^+$ concentration compared to the I/R group (Fig. 4, p = 0.113). However, LND+EGCG treatment (I/R+EGCG+LND group) significantly decreased $NAD^+$ concentration compared to the I/R+EGCG group (Fig. 4, p = 0.006).

## EGCG maintained mitochondrial structure in cardiomyocytes of I/R rats

Cardiomyocytes derived from I/R rats were pre-treated using EGCG and/or LND. As shown in Fig. 5, cardiomyocytes derived from rats in the control group demonstrated tightly arrayed cristae structures; by contrast, after I/R injury, the mitochondrial structures were destructed and vacuoles were formed (Fig. 5). However, EGCG treatment (I/R+EGCG group) remarkably improved the mitochondrial structures and only a few smaller vacuoles were observed (Fig. 5). Moreover, there were no obvious improvements in mitochondrial structures in the I/R+LND and I/R+EGCG+LND groups (Fig. 5).

## EGCG decreased myocardial infarction size in the MIRI rat model

The myocardial infarction size in MIRI rats was also determined in this study (Fig. 6A). Statistical analysis showed no infarction in the sham group rats (Fig. 6B). The myocardial infarction size (IA/AAR ratio) in the MIRI group was significantly higher compared to the sham group (Fig. 6, p = 0.000). The EGCG treatment (MIRI+EGCG group) remarkably decreased the IA/AAR ratio compared to that of the MIRI group (Fig. 6, p = 0.019).

## EGCG enhanced $Ca^{2+}$ and reduced TnT concentrations in the pulmonary artery of MIRI rats

At 120 min post-perfusion, the $Ca^{2+}$ and TnT concentrations in the pulmonary artery of MIRI rats were measured.

612

Q. Tu et al. EGCG reduces myocardial I/R of MIRI rats

**A**



**B**
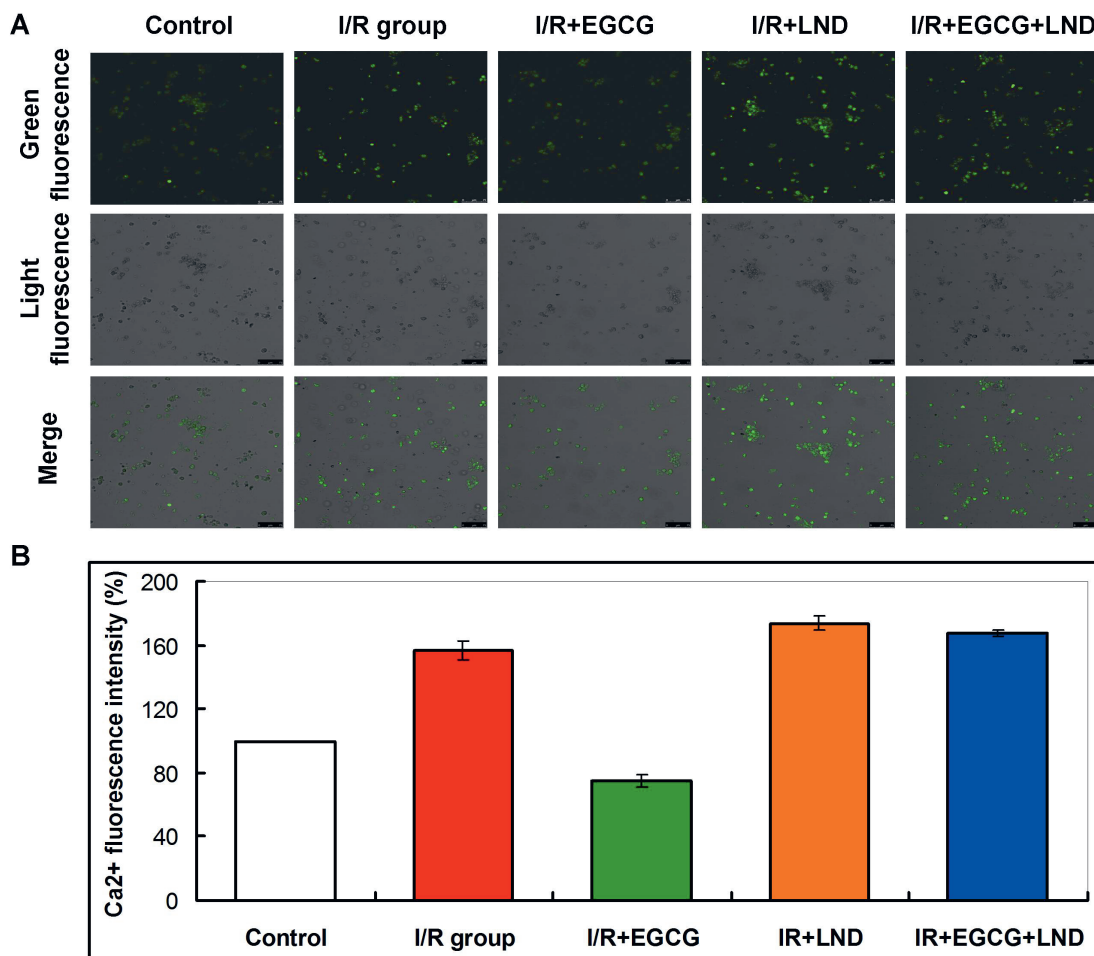


Fig. 3. EGCG decreased intracellular $Ca^{2+}$ concentration in the cardiomyocytes of I/R rats according to $Ca^{2+}$ fluorescence staining results. A. Green fluorescence staining for $Ca^{2+}$ in the cardiomyocytes of I/R rats. Green fluorescence-stained cells represent $Ca^{2+}$ in cardiomyocytes; B. Statistical analysis of $Ca^{2+}$ concentration. For the I/R group compared to the control group p = 0.000; for the I/R+EGCG group compared to the I/R group p = 0.002; for the I/R+EGCG+LND group compared to the I/R+EGCG group p = 0.006
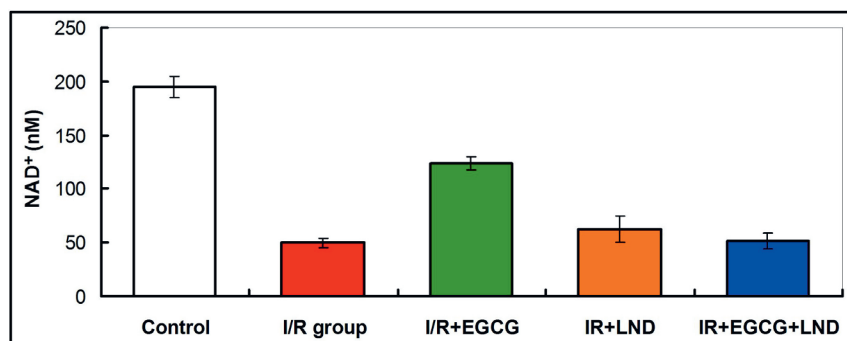


Fig. 4. Evaluation of $NAD^+$ concentration in the cardiomyocytes of I/R rats administered EGCG and/or LND. For the I/R group compared to the control group p = 0.000: for the I/R+EGCG group compared to the I/R group p = 0.000; for the IR+LDN group compared to the I/R group p = 0.113; for the IR+EGCG+LND group compared to the I/R+EGCG group p = 0.000

The results showed that the $Ca^{2+}$ concentration was significantly lower (Fig. 7A, p = 0.000) and the TnT concentration was significantly higher (Fig. 7B, p = 0.000) in the MIRI group compared to the sham group. However, the EGCG treatment (MIRI+EGCG group) obviously enhanced the $Ca^{2+}$ concentration (Fig. 7A, p = 0.000) and significantly reduced the TnT concentration (Fig. 7B, p = 0.001) compared to the MIRI group.

## EGCG improved the ultrastructure of cardiomyocytes of MIRI rats

Cardiomyocytes derived from sham group rats demonstrated a normal and tightly arrayed ultrastructure (Fig. 8).

However, the ultrastructure of cardiomyocytes from MIRI rats was destroyed (Fig. 8). Interestingly, EGCG treatment (I/R+EGCG group) significantly improved the ultrastructure of cardiomyocytes (Fig. 8).

## Discussion

Clinically, blood flow restoration via the coronary artery can reduce the infarct area and aggravate the outcome post-myocardial infarction; however, reperfusion usually induces damage for the ultrastructure of cardiomyocytes in cell metabolism diseases, followed by inflammation of heart tissues.[6,16] The present research discovered that EGCG can
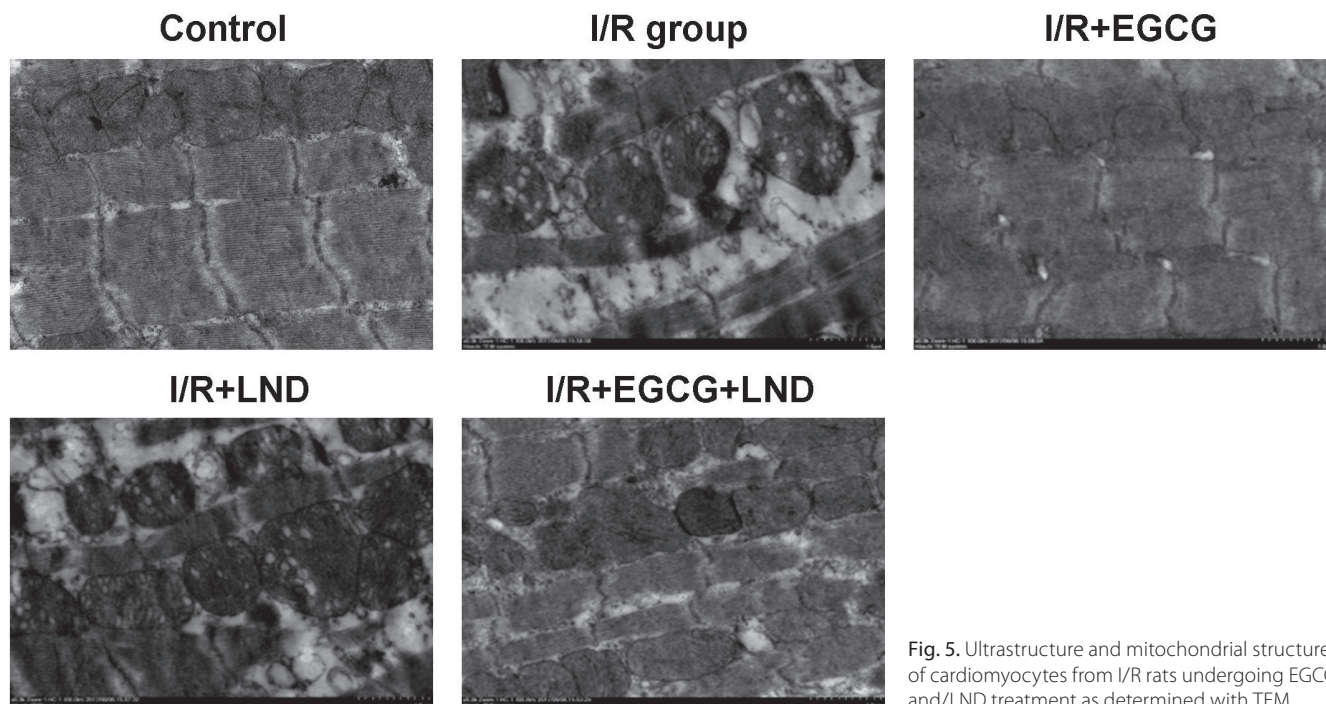
**Fig. 5.** Ultrastructure and mitochondrial structure of cardiomyocytes from I/R rats undergoing EGCG and/LND treatment as determined with TEM
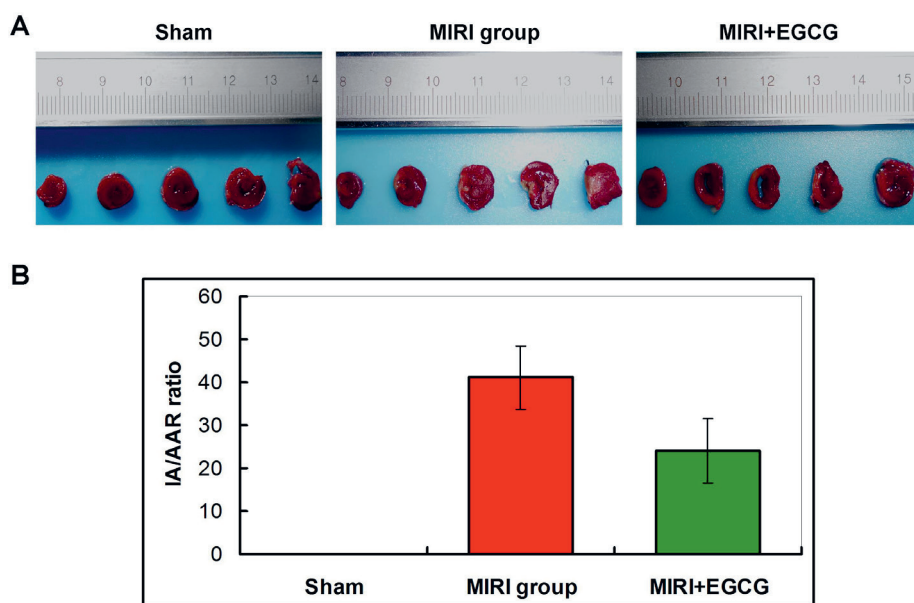


**Fig. 6.** EGCG treatment decreased myocardial infarction in MIRI rats. A. Images of myocardial infarction in MIRI rats undergoing EGCG treatment; B. Statistical analysis of the effects of EGCG treatment on myocardial infarction size (IA/AAR ratio) in MIRI rats. For the MIRI group compared to the sham group p = 0.000; for the MIRI+EGCG group compared to the MIRI group p = 0.019

significantly inhibit myocardial infarction in I/R or MIRI rats by modulating $Ca^{2+}$ and TnT levels in cardiomyocytes.

The EGCG, which is characterized by a series of biological and pharmacological properties, plays promising protective roles in cardiovascular disorders.[11,17] However, previous studies[18,19] have not clarified the specific mechanisms of the protective functions of EGCG on myocardial I/R injury. Therefore, the present research attempted to explore the protective effects of EGCG on myocardial infarction of rat hearts using both I/R models and MIRI models.

In the present research, both I/R models and MIRI models were created as described in previous studies.[14,15] The treatment dose was 10 mg of EGCG for perfusing the heart for 30 min in both I/R and MIRI rats, which was determined from pre-experimental findings of animal studies by our team. Our findings showed that both I/R and MIRI rats demonstrated serious myocardial infarction compared with rats in the control/sham group. Interestingly, EGCG treatment significantly inhibited myocardial infarction in both I/R and MIRI rats, which suggests that EGCG plays critical roles in protecting against I/R injury. For the I/R and MIRI models used in this study, we must acknowledge that the sample size (rat numbers) of each group is relatively small, which is a limitation of this study.

Previous studies[20,21] have reported that myocardial I/R injury is related to the overload of intracellular $Ca^{2+}$.

**A**



**B**
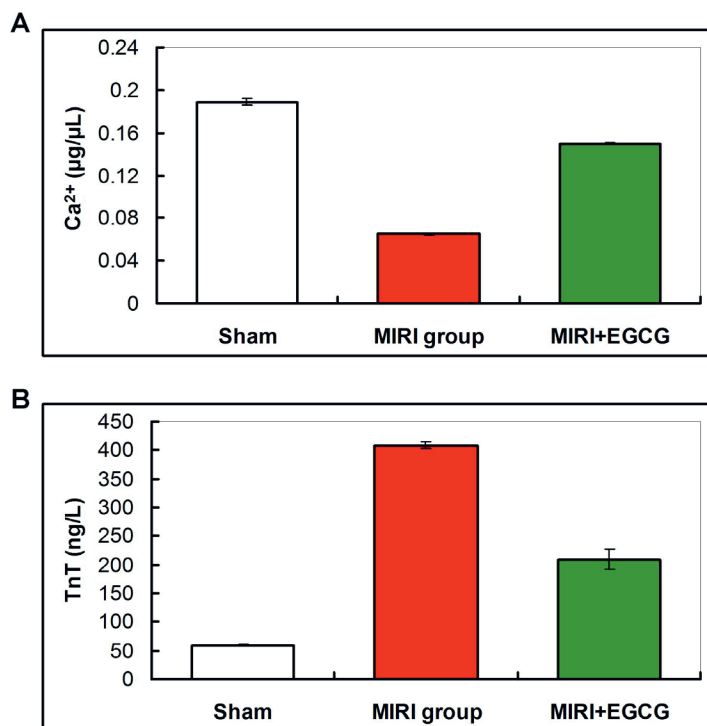


Fig. 7. $Ca^{2+}$ was enhanced and TnT was reduced in the pulmonary artery of MIRI rats undergoing administration of EGCG. A. EGCG administration enhanced $Ca^{2+}$ concentration in MIRI rats. For the MIRI group compared to the sham group p = 0.000; for the MIRI+EGCG group compared to the MIRI group p = 0.000; B. EGCG administration decreased TnT concentration in MIRI rats. For the MIRI group compared to the sham group p = 0.000; for the MIRI+EGCG group compared to the MIRI group p = 0.001

**Sham**      **MIRI group**      **MIRI+EGCG**
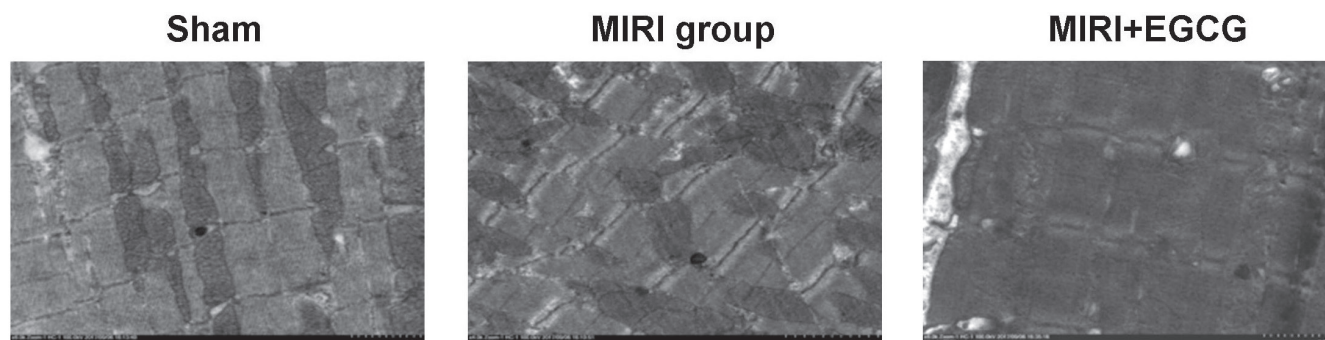


Fig. 8. TEM images illustrating the ultrastructure of cardiomyocytes in MIRI rats

Intracellular $Ca^{2+}$ homeostasis maintains the cardiac functions of the heart, and imbalance of homeostasis is commonly correlated with I/R associated injury.[22] Therefore, we examined the $Ca^{2+}$ levels in coronary perfusion fluid of I/R rats and intracellular $Ca^{2+}$ levels in cardiomyocytes of MIRI rats. The results showed that EGCG treatment significantly increased $Ca^{2+}$ concentration in coronary perfusion fluid of I/R rats and enhanced $Ca^{2+}$ concentration in the pulmonary artery of MIRI rats. Moreover, we found that EGCG decreased the intracellular $Ca^{2+}$ concentration in cardiomyocytes of I/R rats. The EGCG modulated concentration changes of $Ca^{2+}$ suggest that EGCG treatment significantly inhibited the overload of intracellular $Ca^{2+}$ in the cardiomyocytes of I/R rats and MIRI rats. Furthermore, we found that EGCG enhanced the intracellular concentration of TnT, which is a molecule reflecting cardiac functions,[23,24] in cardiomyocytes of I/R and MIRI rats. Our findings show that EGCG treatment significantly decreased TnT concentration in the coronary perfusion fluid of I/R rats and increased intracellular TnT concentration

in the pulmonary artery of MIRI rats, which hint that EGCG treatment remarkably improved heart functions in I/R and MIRI rats.

The content of $NAD^+$ in the myocardium can reflect the opening of mitochondrial permeability transition pores (mPTP): the lower the content of $NAD^+$, the greater the degree of mPTP opening and the more serious the myocardial injury.[25] Thus, we evaluated $NAD^+$ levels in the cardiomyocytes of both EGCG-administered I/R rats and MIRI rats. The results illustrated that EGCG treatment promoted $NAD^+$ concentration in the cardiomyocytes of I/R rats, which suggests that the I/R model-induced myocardial injury was suppressed and cardiac functions were improved. In fact, during myocardial I/R injury, excessive $Ca^{2+}$ is produced and transferred into the mitochondrial matrix, which then causes mPTP opening, production of ROS and ultimately cardiac dysfunction.[26] Our findings prove that EGCG-induced $NAD^+$ changes are consistent with variation in intracellular $Ca^{2+}$ in the cardiomyocytes of I/R and MIRI rats. The EGCG also maintained the ultrastructure

of mitochondria in cardiomyocytes of I/R and MIRI rats, which suggests that EGCG-triggered cardiac function improvement also involves improvement in the ultrastructure of mitochondria. However, the specific mechanism has not been clarified in this study. Moreover, LND participates in the modulation of conventional chemotherapy and radiotherapy for tumors.[27] In recent years, LND, as a mPTP opener, has been proven to reduce cardiac protection in I/R injury.[28] Therefore, LND was employed as a negative regulator for improvement of I/R injury in this study. However, we found no or only slight effects of LND treatment on myocardial infarction size, intracellular $Ca^{2+}$, decreased TnT concentration, and the ultrastructure of cardiomyocytes in I/R isolated heart rat models. Moreover, LND treatment significantly blocked the effects of EGCG on cardiac protection in the I/R rat models. This result suggests that EGCG might modulate improvement in I/R injury mediated by mPTP pathways, which should be explored in future research.

## Limitations

The sample size in this study was relatively small, but it would be enlarged in the further study. Moreover, except for the $Ca^{2+}$ and TnT participating in EGCG effects, the specific molecule signaling pathway has not been clarified in this study.

## Conclusions

EGCG treatment decreased myocardial infarction size in both I/R and MIRI rat models by decreasing intracellular $Ca^{2+}$ concentration, increasing TnT concentration, promoting $NAD^+$ concentration, and improving the ultrastructure of cardiomyocytes. The EGCG treatment used in this study is a potential source of therapeutic strategies for ischemic stroke-associated diseases.

## ORCID iDs

Qingxian Tu ⬤ https://orcid.org/0000-0002-1592-3380
Qianfeng Jiang ⬤ https://orcid.org/0000-0002-0800-2954
Min Xu ⬤ https://orcid.org/0000-0002-4912-2821
Yang Jiao ⬤ https://orcid.org/0000-0002-7947-9960
Huishan He ⬤ https://orcid.org/0000-0003-4664-8913
Shajin He ⬤ https://orcid.org/0000-0001-6462-1058
Weijin Zheng ⬤ https://orcid.org/0000-0001-7994-6541

## References

1. Bartekova M, Barancik M, Ferenczyova K, Dhalla NS. Beneficial effects of N-acetylcysteine and N-mercaptopropionylglycine on ischemia reperfusion injury in the heart. *Curr Med Chem*. 2018;25(3):355–366. doi:10.2174/0929867324666170608111917
2. Kunecki M, Roleder T, Biernat J, et al. Opioidergic conditioning of the human heart muscle in nitric oxide-dependent mechanism. *Adv Clin Exp Med*. 2018;27(8):1069–1073. doi:10.17219/acem/70192
3. Qiao X, Jia S, Ye J. PTPIP51 regulates mouse cardiac ischemia/reperfusion through mediating the mitochondria-SR junction. *Sci Rep*. 2017;7:45379. doi:10.1038/srep45379
4. Ferdinandy P, Schulz R, Baxter GF. Interaction of cardiovascular risk factors with myocardial ischemia/reperfusion injury, preconditioning, and postconditioning. *Pharmacol Rev*. 2007;59(4):418–458. doi:10.1124/pr.107.06002
5. Li Y, Wang X, Lou C. Gastrodin pretreatment impact on sarcoplasmic reticulum calcium transport ATPase (SERCA) and calcium phosphate (PLB) expression in rats with myocardial ischemia reperfusion. *Med Sci Monit*. 2016;22:3309–3315. doi:10.12659/MSM.896835
6. Han MX, Xu XW, Lu SQ, Zhang GX. Effect of olprinone on ischemia-reperfusion induced myocardial injury in rats. *Biomed Pharmacother*. 2019;111:1005–1012. doi:10.1016/j.biopha.2019.01.010
7. Kwak W, Ha YS, Soni N, et al. Apoptosis imaging studies in various animal models using radio-iodinated peptide. *Apoptosis*. 2014;20(1):1–12. doi:10.1007/s10495-014-1059-z
8. Translating cardioprotection for patient benefit: Position paper from the working group of cellular biology of the heart of the European Society of Cardiology. *Cardiovasc Res*. 2013;98(1):7–27. doi:10.1093/cvr/cvt004
9. You L, Pan YY, An MY, et al. The cardioprotective effects of remote ischemic conditioning in a rat model of acute myocardial infarction. *Med Sci Monit*. 2019;25:1769–1779. doi:10.12659/MSM.914916
10. Hsieh SR, Hsu CS, Lu CH, Chen WC, Chiu CH, Liou YM. Epigallocatechin-3-gallate-mediated cardioprotection by Akt/GSK-3beta/caveolin signaling in H9C2 rat cardiomyoblasts. *J Biomed Sci*. 2013;20(1):86. doi:10.1186/1423-0127-20-86
11. Wu Y, Xia ZY, Zhao B, et al. (−)-epigallocatechin-3-gallate attenuates myocardial injury induced by ischemia/reperfusion in diabetic rats and in H9C2 cells under hyperglycemic conditions. *Int J Mol Med*. 2017;40(2):389–399. doi:10.3892/ijmm.2017.3014
12. Salameh A, Schuster R, Dahnert I, Seeger J, Dhein S. Epigallocatechin gallate reduces ischemia/reperfusion injury in isolated perfused rabbit hearts. *Int J Med Sci*. 2018;19(2):628. doi:10.3390/ijms19020628
13. Kim HJ, Yum KS, Sung JH, et al. Epigallocatechin-3-gallate increases intracellular [$Ca^{2+}$] in U87 cells mainly by influx of extracellular $Ca^{2+}$ and partly by release of intracellular stores. *Naunyn Schmiedebergs Arch Pharmacol*. 2004;369(2):260–267. doi:10.1007/s00210-003-0852-y
14. Lasukova TV, Zykova MV, Belousov MV, Gorbunov AS, Logvinova LA, Dygai AM. The role of NO synthase in the cardioprotective effect of substances of humic origin on the model of ischemia and reperfusion of isolated rat heart. *Bull Exp Biol Med*. 2019;166(5):598–601. doi:10.1007/s10517-019-04399-y
15. Lin D, Ma J, Xue Y, Wang Z. Penehyclidine hydrochloride preconditioning provides cardioprotection in a rat model of myocardial ischemia/reperfusion injury. *PLoS One*. 2015;10(12):e0138051. doi:10.1371/journal.pone.0138051
16. Cabrera-Fuentes HA, Aragones J, Bernhagen J, et al. From basic mechanisms to clinical applications in heart protection, new players in cardiovascular diseases and cardiac theranostics: Meeting report from the third international symposium on new frontiers in cardiovascular research. *Basic Res Cardiol*. 2016;111(6):69. doi:10.1007/s00395-016-0586-x
17. Yamazaki KG, Romero-Perez D, Barraza-Hidalgo M, et al. Short- and long-term effects of (−)-epicatechin on myocardial ischemia-reperfusion injury. *Am J Physiol Heart Circ Physiol*. 2008;295(2):H761–H767. doi:10.1152/ajpheart.00413.2008
18. Kim SJ, Li M, Jeong CW, et al. Epigallocatechin-3-gallate, a green tea catechin, protects the heart against regional ischemia-reperfusion injuries through activation of RISK survival pathways in rats. *Arch Pharm Res*. 2014;37(8):1079–1085. doi:10.1007/s12272-013-0309-x
19. Gebka A, Rajtar-Salwa R, Dziewierz A, Petkow-Dimitrow P. Painful and painless myocardial ischemia detected by elevated level of high-sensitive troponin in patients with hypertrophic cardiomyopathy. *Postep Kardiol Inter*. 2018;14(2):195–198. doi:10.5114/aic.2018.76413
20. Dykens JA. Isolated cerebral and cerebellar mitochondria produce free radicals when exposed to elevated $Ca^{2+}$ and $Na^+$: Implications for neurodegeneration. *J Neurochem*. 1994;63(2):584–591. doi:10.1046/j.1471-4159.1994.63020584.x
21. Nath K, Guo L, Nancolas B, et al. Mechanism of antineoplastic activity of lonidamine. *Biochem Biophys Acta*. 2016;1866(2):151–162. doi:10.1016/j.bbcan.2016.08.001
22. Rizzuto R, De Stefani D, Raffaello A, Mammucari C. Mitochondria as sensors and regulators of calcium signalling. *Nat Rev Mol Cell Biol*. 2012;13(9):566–578. doi:10.1038/nrm3412

23. Li C, Zong W, Zhang M, et al. Increased ratio of circulating T-helper 1 to T-helper 2 cells and severity of coronary artery disease in patient with acute myocardial infarction: A prospective observational study. *Med Sci Monit*. 2019;25:6034–6042. doi:10.12659/MSM.913891

24. Bian WS, Tian FH, Jiang LH, et al. Influence of miR-34a on myocardial apoptosis in rats with acute myocardial infarction through the ERK1/2 the ERK1/2 pathway. *Eur Rev Med Pharmacol Sci*. 2019;23(7):3034–3041. doi:10.26355/eurrev_201904_17585

25. Jia P, Liu C, Wu N, Jia D, Sun Y. Agomelatine protects against myocardial ischemia reperfusion injury by inhibiting mitochondrial permeability transition pore opening. *Am J Transl Res*. 2018;10(5):1310–1323. PMID:29887947

26. Giorgi C, Baldassari F, Bononi A, et al. Mitochondrial Ca(2+) and apoptosis. *Cell Calcium*. 2012;52(1):36–43. doi:10.1016/j.ceca.2012.02.008

27. Di Cosimo S, Ferretti G, Papaldo P, Carlini P, Fabi A, Cognetti F. Lonidamine: Efficacy and safety in clinical trials for the treatment of solid tumors. *Drugs Today (Barc)*. 2003;39(3):157–174. doi:10.1358/dot.2003.39.3.799451

28. Hao J, Li WW, Du H, et al. Role of vitamin C in cardioprotection of ischemia/reperfusion injury by activation of mitochondrial KATP channel. *Chem Pharm Bull (Tokyo)*. 2016;64(6):548–557. doi:10.1248/cpb.c15-00693

Original papers

# The effect of erythrocyte transfusion on macrophage pyroptosis and inflammation in a sepsis model

Yong Cheng[1,B,C,E,F], Zhen-Zhou Li[1,2,A–F], Huan Wang[1,A–F], Jin-Huo Wang[1,B,C,E,F],
Xiao-Fang Zhou[1,B,C,E,F], Jia-Ming Xu[1,B,C,E,F], Xun Zhou[1,C,E,F], Jian-Rong Guo[1,2,C,E,F]

[1] Department of Anesthesiology, Shanghai Gongli Hospital, The Second Military Medical University, China

[2] Ningxia Medical University, Gongli Hospital of Shanghai Pudong New Area Training Base, Shanghai, China

A – research concept and design; B – collection and/or assembly of data; C – data analysis and interpretation;
D – writing the article; E – critical revision of the article; F – final approval of the article

**Address for correspondence**
Jian-Rong Guo
E-mail: gjr8259@yeah.net

## Abstract

**Background.** Sepsis is one of most common causes of death in the intensive care unit (ICU) due to infection and inflammation. The Duffy antigen receptor for chemokines (DARC) regulates pro-inflammatory cytokines, thus playing an important role in inflammation.

**Objectives.** This study aimed to elucidate the correlation among erythrocyte transfusion, macrophage pyroptosis and inflammation in the progression of sepsis.

**Materials and methods.** Alanine aminotransferase (ALT/GPT) activity was measured with the ALT/GPT activity measurement kit (Jiancheng Bio, Nanjing, China) according to the kit manual. The ET-1 concentration was measured with enzyme-linked immunosorbent assay (ELISA) using the endothelin-1 (ET-1) measurement kit (Jiancheng Bio) according to the kit manual. Apoptosis was evaluated using flow cytometry-based Annexin V staining assay. The cells were collected using centrifugation and resuspended in binding buffer. Ultrastructural analysis of pyroptotic body, the levels of interleukin (IL)-1β, IL-18, IL-33, MIP-2, CXCL8, reactive oxygen species (ROS), and LTB4 were measured with ELISA.

**Results.** Our results showed that septic rats had impaired hepatic function and ET-1 levels. Erythrocyte transfusion upregulated DARC expression in the sepsis model. Erythrocyte transfusion also affected pyroptosis in macrophages, reduced the production of inflammatory cytokines, such as IL-1β, IL-18 and IL-33, and alleviated cytotoxicity in the sepsis model.

**Conclusions.** Erythrocyte transfusion may function as a therapeutic tool against sepsis by regulating pyroptosis, inflammation and cytotoxicity.

**Key words:** transfusion, erythrocyte, pyroptosis, sepsis, DARC

618

Y. Cheng et al. Erythrocyte transfussion-affected pyroptosis

# Background

The Duffy antigen receptor for chemokines (DARC) is an atypical receptor that regulates pro-inflammatory cytokines.[1] It is expressed in multiple tissues, including kidney and brain.[2,3] It has also been reported that DARC plays a role in erythrocyte function. For example, DARC found on the surface of erythrocytes facilitates chemokine reception.[4] *Staphylococcus aureus* has been shown to target DARC to lyse erythrocytes within the mammalian host.[5] The DARC is also engaged in *Plasmodium* spp.-induced red blood cell invasion.[6] Furthermore, DARC regulates inflammatory responses in adipose tissues,[7] asthma[1] and fractures.[8] Thus, DARC may act as a critical regulator in inflammation-related pathological processes.

Sepsis is one of the most common causes of death among hospitalized patients in the intensive care unit (ICU).[9] It has multiple effects on erythrocytes.[10] Sepsis alters erythrocyte morphology and blood flow in capillary networks.[11] The mechanism underlying the effect of sepsis on erythrocytes remains unclear; however, several factors such as inflammation and oxidative stress are involved in this process.[12] Previous studies have explored the effect of erythrocyte transfusion in patients with sepsis.[13] However, the mechanism is still controversial. More and more studies demonstrate that oxygen delivery remains sufficient during sepsis while erythrocyte transfusion increases the oxygen-carrying capacity of the blood flow.[14]

Pyroptosis is a programmed and inflammatory form of cell death, which is different from the long-standing form of cell death. It is one of the mechanisms of programmed cell death (PCD). Pyroptotic cells undergo nuclear condensation and chromatin DNA fragmentation,[15] releasing pro-inflammatory mediators.[16] Pyroptosis contributes to the pathogenesis of several diseases, including cancer,[17] atherosclerosis,[18] liver disease,[19] etc. In sepsis, pyroptosis is a hallmark that marks progress and recovery.[20,21] In this study, we found that erythrocyte transfusion affected pyroptosis in macrophages and attenuated inflammation in a sepsis model. This work elucidated the correlation among erythrocyte transfusion, macrophage pyroptosis and inflammation in the progression of sepsis, thereby presenting a potential therapeutic method for treating sepsis.

# Materials and methods

## Establishment of a rat sepsis model

Two-month-old male Sprague Dawley rats (250 g) were purchased from Shanghai Model Organisms (Shanghai, China). Rats were housed under pathogen-free conditions with a 12-hour light/dark cycle. Rats received a single intraperitoneal injection of 10 mg/kg of lipopolysaccharide (LPS; Sigma-Aldrich, St. Louis, USA). Control animals received an equal volume of intraperitoneal saline.

## Measurement of ALT/GPT activity

Alanine aminotransferase (ALT/GPT) activity was measured with the ALT/GPT activity measurement kit (Jianchen Bio, Nanjing, China) according to the kit manual.

## Measurement of endothelin-1 concentration

The endothelin-1 (ET-1) concentration was measured using enzyme-linked immunosorbent assay (ELISA) using the ET-1 measurement kit (Jiancheng Bio) according to the kit manual.

## Erythrocytes isolation and transfusion

Whole blood was centrifuged at 500 × g for 10 min at 4°C. The supernatant containing plasma was aspirated and erythrocyte pellets were rinsed with wash buffer. Then, erythrocytes were again centrifuged at 500 × g for 10 min at 4°C and rinsed with wash buffer. Freshly collected erythrocytes were transfused into the sepsis model via tail vein injection.

## Flow cytometry

Erythrocytes membrane protein DARC was determined using anti-DARC-FITC antibody (Abcam, Cambridge, UK). Followed by the fixation with 2% paraformaldehyde for 15 min, citrated blood was incubated with HEPES for 2 min. The antibody was added to the sample and incubated for 45 min in the dark. Cells were washed and suspended in Dulbecco's phosphate-buffered saline (DPBS). Flow cytometry was performed using a BD Accuri C6 (Becton Dickinson Biosciences, Franklin Lakes, USA). Data were analyzed using CFlow Plus software v. 1.0.227.04 (Becton Dickinson). Macrophage population was differentiated using flow cytometry (FCM) as previously described.[22]

## Annexin V staining assay

Apoptosis was evaluated using FCM-based Annexin V staining assay. Briefly, cells were collected using centrifugation and resuspended in binding buffer. Then, 5 μL of Annexin V-FITC and 5 μL of propidium iodide (PI) were added to the cells and incubated at room temperature for 5 min in the dark. Finally, Annexin V-FITC binding was analyzed (Ex = 488 nm; Em = 350 nm) using FITC signal detector and PI staining using a phycoerythrin emission signal detector.

## Ultrastructural analysis of pyroptotic body

Ultrastructural alteration in the pyroptotic body was detected with a scanning electron microscope (SEM). Samples were prepared as previously reported.[23] Images were captured under the JEOL NeoScope JCM-7000 Scanning Electron Microscope (JEOL Ltd., Tokyo, Japan).

## ELISA

The levels of interleukin (IL)-1β, IL-18, IL-33, macrophage inflammatory protein 2 (MIP-2), Invitrogen anti-IL-8 (CXCL8) (Invitrogen, Carlsbad, USA), reactive oxygen species (ROS), and leukotriene B4 (LTB4) were measured with ELISA. The ELISA kit (Jiancheng Bio) was used to detect the changes in the concentration of the abovementioned cytokines. The measurement was performed according to the kit manual.

## Cytotoxicity assay

The concentration of LDH was measured with the LDH detection kit (Jiancheng Bio) according to the kit manual.

## Statistical analyses

Data were expressed as mean ± standard error of the mean. Statistical significance was determined using unpaired Student's t-test or one-way analysis of variance (ANOVA) followed by the Bonferroni post hoc test using GraphPad Prism software v. 5.0 (GraphPad Software, San Diego, USA). A p-value <0.05 was considered statistically significant.
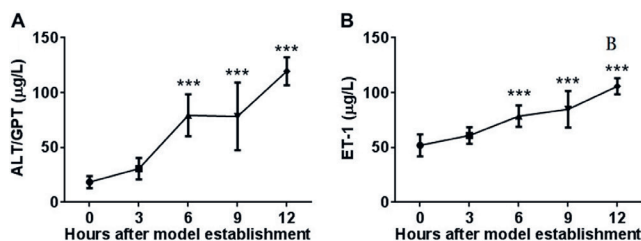


Fig. 1. The alteration in the levels of ALT/GPT (A) and ET-1 (B) in septic rats. The statistical difference was determined using a one-way ANOVA followed by the Bonferroni post hoc test; ***$p < 0.001$ compared to 0 h after model establishment

# Results

## Septic rats showed impaired hepatic function and altered endothelin-1 levels

Firstly, we examined the hepatic function and ET-1 levels in the sepsis model. The concentration of ALT/GPT was significantly higher in septic rats at 6 h, 9 h and 12 h after model establishment (Fig. 1A, $p < 0.001$, n = 3) compared with those measured at the 0 h. Meanwhile, ET-1 concentration at 6 h, 9 h and 12 h after model establishment (Fig. 1B, $p < 0.001$, n = 3) was also significantly higher than at the 0 h. Thus, the sepsis model was successfully established.

## Erythrocyte transfusion affected macrophages in septic rats

Secondly, we injected rats with erythrocytes to evaluate the potential benefit of erythrocyte transfusion. Flow cytometry results showed that the expression of DARC in septic rats injected with erythrocytes (Fig. 2A) was upregulated compared to the control animals (Fig. 2B). Flow cytometry
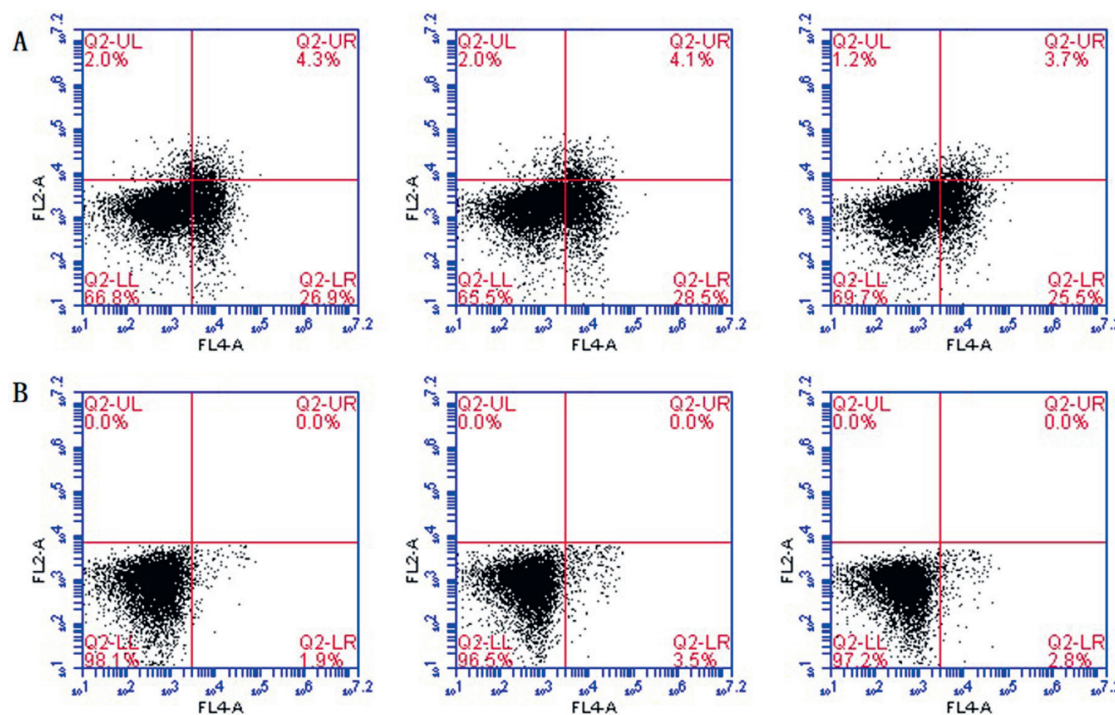


Fig. 2. Flow cytometry showed that (A) erythrocyte injection enhanced DARC level in septic rats in comparison to those injected with saline (B)
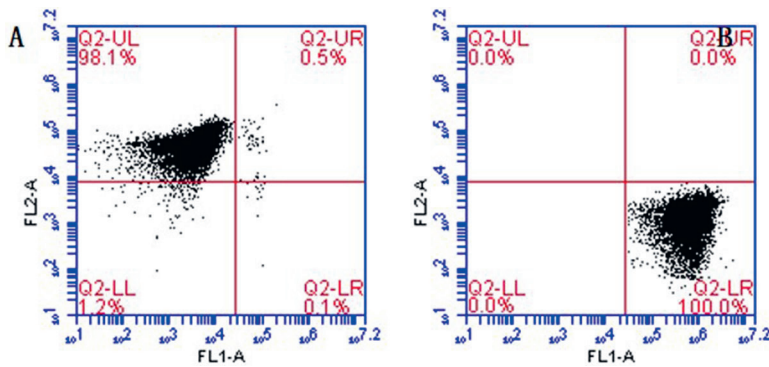
Fig. 3. Flow cytometry indicated that the ratio of macrophages was significantly different between sepsis model rats injected with erythrocytes (A) or saline (B)
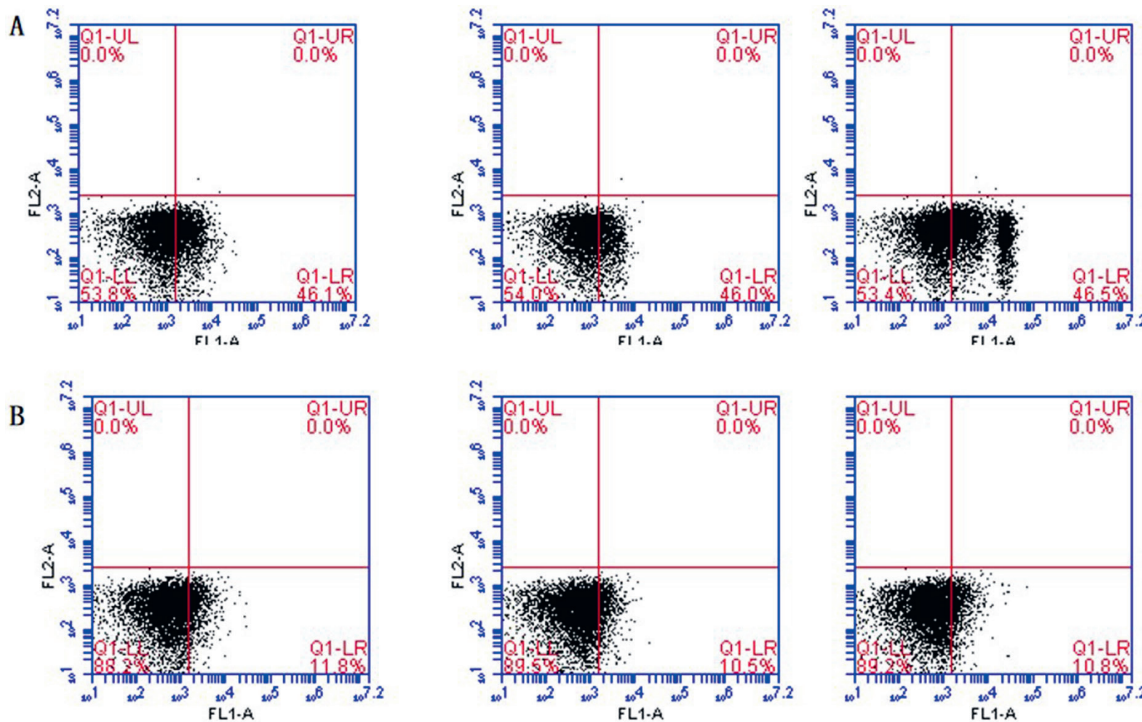


Fig. 4. Flow cytometry showed the alteration in the ratio of apoptotic cells in the blood collected from erythrocyte-injected (A) and saline-injected septic rats (B)

analysis also indicated that the ratio of macrophages in the blood collected from rats treated with erythrocyte transfusion was different from that of the control group (Fig. 3A,B). Furthermore, macrophages of erythrocyte-injected rats underwent more severe apoptosis compared to those administered with saline (Fig. 4A,B). Ultrastructural alteration in the pyroptotic body was detected using SEM. Compared to the saline controls, erythrocyte-injected rats had fewer pyroptotic bodies in macrophages (Fig. 5A,B). Thus, erythrocyte transfusion could attenuate the pyroptosis of macrophages in septic rats.

## Erythrocyte transfusion attenuated inflammation in septic rats

Thirdly, we explored whether erythrocyte transfusion could affect inflammatory responses in the sepsis model. The ELISA results showed that the concentration of inflammatory factors (i.e., IL-1β, IL-18, IL-33) and other inflammation-related proteins (i.e., MIP-2, CXCL8, ROS, LTB4) was significantly lower in septic rats injected with

erythrocytes as compared with the control animals (Fig. 6). Thus, erythrocyte transfusion suppressed inflammation in the sepsis model.

## Erythrocyte transfusion inhibited LDH activity in the sepsis model

To further analyze the effect of erythrocyte transfusion, lactate dehydrogenase (LDH) activity in the sepsis model was measured. The LDH activity of septic rats injected with erythrocytes was significantly lower compared with the control group (Fig. 7), suggesting that erythrocyte transfusion alleviated cytotoxicity in the sepsis model.

## Discussion

The DARC is a transmembrane protein expressed on erythrocytes.[24] Since erythrocytes function as a primary reservoir of macrophage migration inhibitory factor in the whole blood, DARC might be correlated with
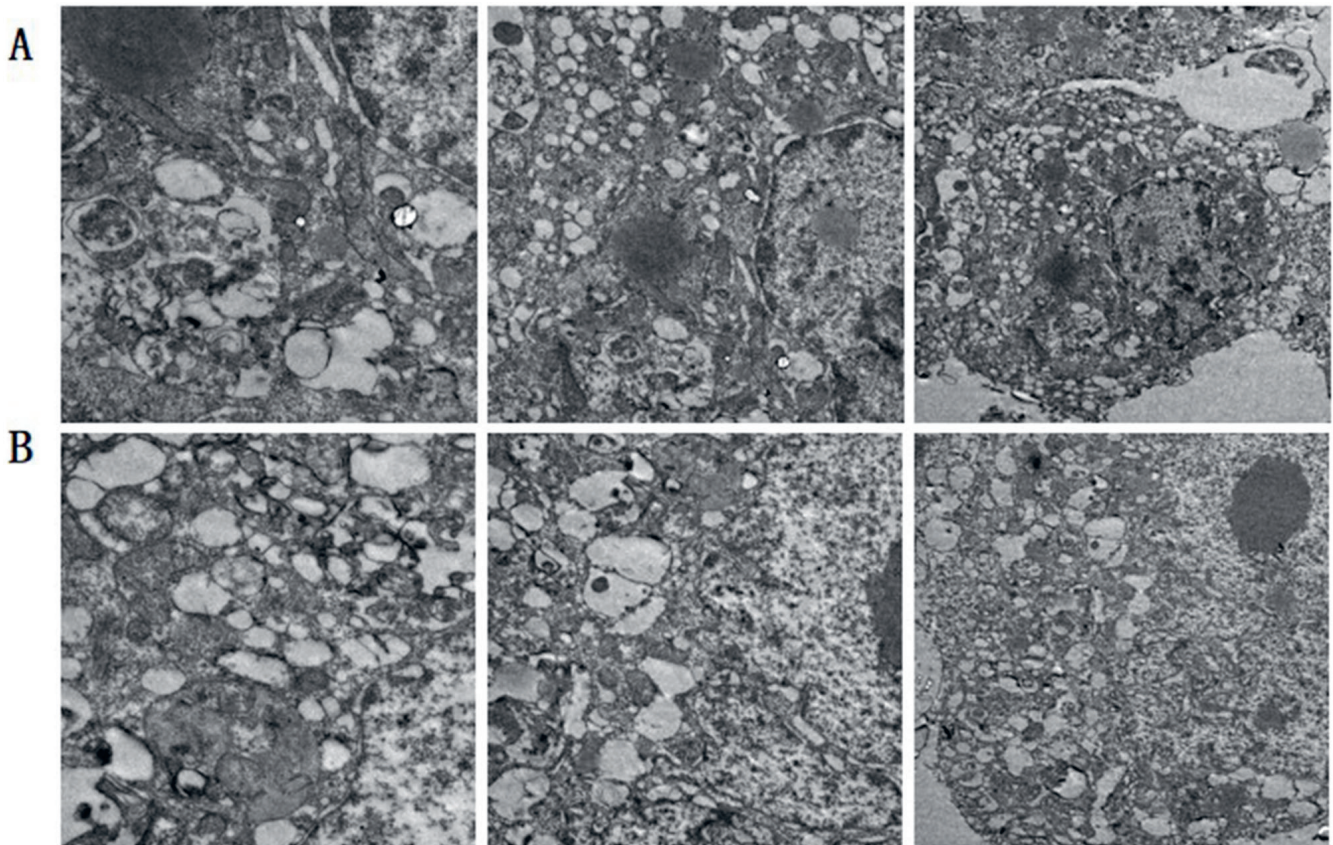
**Fig. 5.** Ultrastructural alteration of the pyroptotic body of macrophages collected from erythrocyte-injected (A) and saline-treated (B) septic rats was detected with SEM
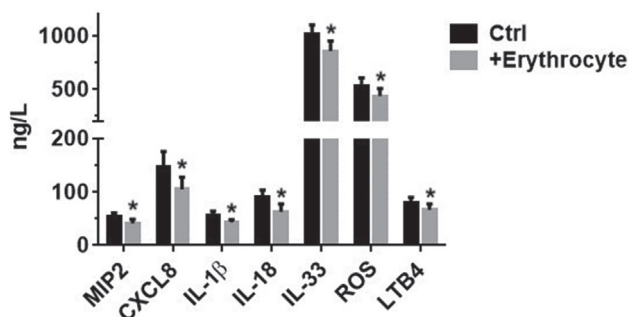


**Fig. 6.** ELISA showed that the levels of MIP-2, CXCL8, IL-1β, IL-18, IL-33, ROS, and LTB4 were different between erythrocyte-injected (A) and saline-treated (B) septic rats; * $p < 0.05$



**Fig. 7.** LDH activity was affected in septic rats injected with erythrocytes

inflammation.[25] We found that the expression of DARC was upregulated in septic rats injected with erythrocytes when compared to the control model animals (Fig. 2). These findings provide direct evidence that DARC is involved in the therapeutic effect of erythrocyte transfusion in sepsis. Furthermore, we showed that erythrocyte transfusion decreased the level of pro-inflammatory factors (Fig. 6), indicating that transfused erythrocytes attenuate inflammation in sepsis. This is the first demonstration of its kind that shows the therapeutic effects of erythrocytes in sepsis treatment. Considering that inflammation is one of the biomarkers in sepsis,[26] a decrease in the level of pro-inflammatory factors may be a promising strategy in treating sepsis.

Further investigations of the levels of lactate and C-reactive protein (CRP), and procalcitonin, neutrophil and monocyte activation are needed to comprehensively evaluate the effect of erythrocyte transfusion on sepsis.

Erythrocyte transfusion alleviated pyroptosis in the sepsis model (Fig. 5). Unlike apoptosis and necrosis, pyroptosis is accompanied by the release of pro-inflammatory mediators.[27] Attenuation in pyroptosis inhibited the release of pro-inflammatory factors, which is consistent with our findings that erythrocyte transfusion inhibited the level of pro-inflammatory factors in septic rats (Fig. 6). However, the underlying mechanism of sepsis-induced inflammation is still unclear. Several factors may contribute to potential mechanisms, including cAMP metabolism,[28] NLRP3 activation[29] and inflammasome activation.[30] All of these require further investigation.

## Limitations

The results in this paper showed that septic rats had impaired hepatic function and altered ET-1 levels. Erythrocyte transfusion upregulated DARC expression in the sepsis model. Erythrocyte transfusion also affected pyroptosis in macrophages, reduced the production of inflammatory cytokines, such as IL-1β, IL-18 and IL-33, and alleviated cytotoxicity in the sepsis model.

Macrophages polarize to the classical M1 macrophage activation pathway and promote inflammatory cytokine response. Studies on the interaction between stored RBCs infusion and macrophages mainly focus on macrophages in peripheral blood. However, due to time constraints and small sample size, sepsis is affected by a variety of factors. Considering that the purpose of the study is to group and compare according to a single index, and other factors among the groups have not been corrected, a more rigorous, multi-center, large sample and further analysis are still needed to improve the accuracy and universality of the research results.

## Conclusions

Erythrocyte transfusion may function as a therapeutic tool against sepsis by regulating pyroptosis, inflammation and cytotoxicity.

### ORCID iDs

Yong Cheng https://orcid.org/0000-0002-7424-9373
Zhen-Zhou Li https://orcid.org/0000-0003-3774-7565
Huan Wang https://orcid.org/0000-0003-3646-2656
Jin-Huo Wang https://orcid.org/0000-0002-8060-8045
Xiao-Fang Zhou https://orcid.org/0000-0002-9300-4478
Jia-Ming Xu https://orcid.org/0000-0002-3167-1064
Xun Zhou https://orcid.org/0000-0002-2000-1284
Jian-Rong Guo https://orcid.org/0000-0002-3995-2995

## References

1. Chapman DG, Mougey EB, van der Velden JL, et al. The Duffy antigen receptor for chemokines regulates asthma pathophysiology. *Clin Exp Allergy*. 2017;47(9):1214–1222. doi:10.1111/cea.12949
2. Hadley TJ, Lu ZH, Wasniowska K, et al. Postcapillary venule endothelial cells in kidney express a multispecific chemokine receptor that is structurally and functionally identical to the erythroid isoform, which is the Duffy blood group antigen. *J Clin Invest*. 1994;94(3):985–991. doi:10.1172/JCI117465
3. Horuk R, Martin AW, Wang Z, et al. Expression of chemokine receptors by subsets of neurons in the central nervous system. *J Immunol*. 1997;158(6):2882–2890. PMID:9058825
4. Yamamoto A, Saito N, Ogasawara S, et al. Intracellular storage of Duffy antigen-binding chemokines by Duffy-positive red blood cells. *Clin Lab*. 2017;63(4):717–723. doi:10.7754/Clin.Lab.2016.161027
5. Spaan AN, Reyes-Robles T, Badiou C, et al. *Staphylococcus aureus* targets the Duffy antigen receptor for chemokines (DARC) to lyse erythrocytes. *Cell Host Microbe*. 2015;18(3):363–370. doi:10.1016/j.chom.2015.08.001
6. Batchelor JD, Malpede BM, Omattage NS, DeKoster GT, Henzler-Wildman KH, Tolia NH. Red blood cell invasion by *Plasmodium vivax*: Structural basis for DBP engagement of DARC. *PLoS Pathog*. 2014;10(1):e1003869. doi:10.1371/journal.ppat.1003869
7. Benson TW, Weintraub DS, Crowe M, et al. Deletion of the Duffy antigen receptor for chemokines (DARC) promotes insulin resistance and adipose tissue inflammation during high fat feeding. *Mol Cell Endocrinol*. 2018;473:79–88. doi:10.1016/j.mce.2018.01.006
8. Rundle CH, Mohan S, Edderkaoui B. Duffy antigen receptor for chemokines regulates post-fracture inflammation. *PLoS One*. 2013;8(10):e77362. doi:10.1371/journal.pone.0077362
9. Vincent JL, Rello J, Marshall J, et al. International study of the prevalence and outcomes of infection in intensive care units. *JAMA*. 2009;302(21):2323–2329. doi:10.1001/jama.2009.1754
10. Bateman RM, Sharpe MD, Singer M, Ellis CG. The effect of sepsis on the erythrocyte. *Int J Mol Sci*. 2017;18(9):1932. doi:10.3390/ijms18091932
11. Ellis CG, Bateman RM, Sharpe MD, Sibbald WJ, Gill R. Effect of a maldistribution of microvascular blood flow on capillary $O_2$ extraction in sepsis. *Am J Physiol Heart Circ Physiol*. 2002;282:H156–H164. doi:10.1152/ajpheart.2002.282.1.H156
12. Semba RD, Patel KV, Ferrucci L, et al. Serum antioxidants and inflammation predict red cell distribution width in older women: The Women's Health and Aging Study I. *Clin Nutr*. 2010;29(5):600–604. doi:10.1016/j.clnu.2010.03.001
13. Chan YL, Han ST, Li CH, Wu CC, Chen KF. Transfusion of red blood cells to patients with sepsis. *Int J Mol Sci*. 2017;18(9):1946. doi:10.3390/ijms18091946
14. Mira JP, Fabre JE, Baigorri F, et al. Lack of oxygen supply dependency in patients with severe sepsis: A study of oxygen delivery increased by military antishock trouser and dobutamine. *Chest*. 1994;106(5):1524–1531. doi:10.1378/chest.106.5.1524
15. Bergsbaken T, Cookson BT. Macrophage activation redirects yersinia-infected host cell death from apoptosis to caspase-1-dependent pyroptosis. *PLoS Pathog*. 2007;3(11):e161. doi:10.1371/journal.ppat.0030161
16. Bergsbaken T, Fink SL, Cookson BT. Pyroptosis: Host cell death and inflammation. *Nat Rev Microbiol*. 2009;7(2):99–109. doi:10.1038/nrmicro2070
17. Xia X, Wang X, Cheng Z, et al. The role of pyroptosis in cancer: Pro-cancer or pro-"host"? *Cell Death Dis*. 2019;10(9):650. doi:10.1038/s41419-019-1883-8
18. Xu YJ, Zheng L, YW Hu, Wang Q. Pyroptosis and its relationship to atherosclerosis. *Clin Chim Acta*. 2018;476:28–37. doi:10.1016/j.cca.2017.11.005
19. Guo H, Xie M, Zhou C, Zheng M. The relevance of pyroptosis in the pathogenesis of liver diseases. *Life Sci*. 2019;223:69–73. doi:10.1016/j.lfs.2019.02.060
20. Wang D, Zheng J, Hu Q, et al. Magnesium protects against sepsis by blocking gasdermin D N-terminal-induced pyroptosis. *Cell Death Differ*. 2019;27(2):466–481. doi:10.1038/s41418-019-0366-x
21. Zhang FL, Zhou BW, Yan ZZ, et al. 6-gingerol attenuates macrophages pyroptosis via the inhibition of MAPK signaling pathways and predicts a good prognosis in sepsis. *Cytokine*. 2019;125:154854. doi:10.1016/j.cyto.2019.154854
22. Vermaelen K, Pauwels R. Accurate and simple discrimination of mouse pulmonary dendritic cell and macrophage populations by flow cytometry: Methodology and new insights. *Cytometry A*. 2004;61(2):170–177. doi:10.1002/cyto.a.20064
23. Fischer ER, Hansen BT, Nair V, Hoyt FH, Dorward DW. Scanning electron microscopy. *Curr Protoc Microbiol*. 2012;25(1):2B.2.1–2B.2.47. doi:10.1002/9780471729259.mc02b02s25
24. Miller LH, Mason SJ, Dvorak JA, McGinniss MH, Rothman IK. Erythrocyte receptors for (*Plasmodium knowlesi*) malaria: Duffy blood group determinants. *Science*. 1975;189(4202):561–563. doi:10.1126/science.1145213
25. Karsten E, Hill CJ, Herbert BR. Red blood cells: The primary reservoir of macrophage migration inhibitory factor in whole blood. *Cytokine*. 2018;102:34–40. doi:10.1016/j.cyto.2017.12.005
26. Faix JD. Biomarkers of sepsis. *Crit Rev Clin Lab Sci*. 2013;50(1):23–36. doi:10.3109/10408363.2013.764490
27. Robinson N, Ganesan R, Hegedus C, Kovacs K, Kufer TA, Virag L. Programmed necrotic cell death of macrophages: Focus on pyroptosis, necroptosis, and parthanatos. *Redox Biol*. 209;26:101239. doi:10.1016/j.redox.2019.101239
28. Chen R, Zeng L, Zhu S, et al. cAMP metabolism controls caspase-11 inflammasome activation and pyroptosis in sepsis. *Sci Adv*. 2019;5(5):eaav5562. doi:10.1126/sciadv.aav5562
29. Li N, Zhou J, Wu H, et al. STING-IRF3 contributes to lipopolysaccharide-induced cardiac dysfunction, inflammation, apoptosis and pyroptosis by activating NLRP3. *Redox Biol*. 2019;24:101215. doi:10.1016/j.redox.2019.101215
30. Kumar V. Inflammasomes: Pandora's box for sepsis. *J Inflamm Res*. 2018;11:477–502. doi:10.2147/JIR.S178084

# Investigation of the role of *miR-221* in diabetic peripheral neuropathy and related molecular mechanisms

Xiaole Wu[1,2,A–F], Xiaoyu Wang[3,B,C,E,F], Yiyu Yin[4,B,C,E,F], Lei Zhu[5,B,C,E,F], Fengchao Zhang[2,B,C,E,F], Jianping Yang[1,C,E,F]

[1] Department of Anesthesiology, The First Affiliated Hospital of Soochow University, Suzhou, China

[2] Department of Anesthesiology, Xuzhou Children's Hospital, Xuzhou Medical University, China

[3] Department of Thoracic Surgery, Xuzhou Children's Hospital, Xuzhou Medical University, China

[4] Department of General Surgery, Xuzhou Children's Hospital, Xuzhou Medical University, China

[5] Intensive Care Unit, Xuzhou Children's Hospital, Xuzhou Medical University, China

A – research concept and design; B – collection and/or assembly of data; C – data analysis and interpretation;
D – writing the article; E – critical revision of the article; F – final approval of the article

## Abstract

**Background.** Diabetic peripheral neuropathy (DPN) is one of the most common complications of diabetes, but the molecular mechanisms of DPN are still unclear.

**Objectives.** To investigate the role of *miR-221* in DPN and the related molecular mechanisms.

**Materials and methods.** Streptozotocin (STZ) was used to establish an in vivo DPN model. An in vitro DPN model was established using high glucose-induced SH-SY5Y cells. The pain condition of rats was measured by evaluating the 50% paw withdrawal threshold (PWT) and paw withdrawal latency (PWL). Serum exosomes were extracted and identified. Expression of *miR-221* in serum exosomes and serum *SOCS3* expression were determined using reverse-transcription quantitative polymerase chain reaction (RT-qPCR). Western blotting was used to measure the protein levels of *SOCS3*, bradykinin (BK) and prostaglandin E2 (PEG2). The dual luciferase reporter assay was performed to confirm *SOCS3* 3'-UTR as a target of *miR-221*. The serum or cell supernatant levels of PEG2, BK, interleukin (IL)-6, IL-1β, and tumor necrosis factor alpha (TNF-α) were measured using enzyme-linked immunosorbent assay (ELISA).

**Results.** Induction of the lenti-miR-221 inhibitor significantly decreased the expression of *miR-221* in DPN rats. Both 50% PWT and PWL values were markedly decreased in DPN rats. When *miR-221* was inhibited, the 50% PWT and PWL values were both significantly increased. Knockdown of *miR-221* significantly increased the expression of *SOCS3* and decreased the expression of NF-κB. Furthermore, knockdown of *miR-221* remarkably decreased the expression of PEG2, BK, IL-6, IL-1β, and TNF-α in both STZ-treated DPN rats and high glucose-induced SH-SY5Y cells, which was reversed by inhibition of *SOCS3*. The dual luciferase reporter assay showed that *miR-221* directly targeted and negatively regulated *SOCS3*.

**Conclusions.** Inhibition of *miR-221* can reduce pain and decrease expression of inflammatory factors through targeting *SOCS3* in DPN.

**Key words:** exosomes, *miR-221*, *SOCS3*, diabetic peripheral neuralgia

624

X. Wu et al. Investigating the role of *miR-221* in DPN

# Background

Diabetic peripheral neuropathy (DPN) is one of the most common complications of diabetes. Almost 50% of diabetic patients develop DPN during their lifetime and about 10–26% of newly diagnosed diabetic patients suffer from DPN.[1,2] Compared to other types of peripheral neuropathy, the development of DPN is more rapid. Research has reported that DPN is the primary cause of diabetic foot ulcer and amputation, which lead to disability.[3–5] Generally, it is considered that DPN is the result of many factors related to the hyperglycemic condition. Many factors influence DPN incidence, including glycosylation of tissue protein, oxidative stress, mitochondrial damage, inflammation activation, and activation of the polyol pathway.[6–8] However, the molecular mechanisms of DPN are still unclear.

MicroRNA (miRNA) is a kind of endogenous non-coding RNA with a length of about 20–24 bases that plays wide roles in organisms.[9] Among miRNAs, *miR-221* plays important roles in many diseases. Oh et al. found that *miR-221* could inhibit oxidative stress through regulating DJ-1 in Parkinson's disease.[10] Fornari et al. demonstrated that *miR-221* could induce sorafenib resistance by inhibiting caspase-3-mediated apoptosis in hepatoma cells.[11] In addition, *miR-221* was found to be upregulated in diabetes and promote diabetes development.[12] However, the role of *miR-221* in DPN has not been elucidated yet.

# Objectives

In the present study, we aimed to investigate the role of *miR-221* in DPN. We demonstrated that inhibition of *miR-221* led to reduction of pain and decreased inflammatory factors through targeting *SOCS3* in the DPN model. This research might give deeper insights into the molecular mechanisms of DPN.

# Materials and methods

## Animals and treatment

For establishment of the DPN in vivo model, 40 male Sprague Dawley (SD) rats (215 ±15 g, 3-month old) were purchased from the Laboratory Animal Center of Xuzhou Medical University, China. The rats were kept in microisolator cages in a light-controlled room under a 12 h/12 h light/dark cycle and a controlled temperature (23–25°C), and had free access to food and water. All efforts were made to avoid unnecessary pain suffered by the animals. This study was approved by the Institutional Animal Care Committee at Xuzhou Children's Hospital.

Animals were divided into 4 groups (n = 10 per group): 1) control group; 2) streptozotocin (STZ)-induced DPN group; 3) DPN and *miR-221* inhibitor group; and 4) DPN and inhibitor negative control (NC) group. For establishment of the DPN model, rats received daily intraperitoneal injection of STZ (Sinopharm Group, Co. Ltd., Shanghai, China) at a dose of 60 mg/kg. After 7 days of injection, the blood glucose level of the rats was evaluated using a blood glucose meter (Abbott Laboratories, Chicago, USA), and a blood glucose level >16.7 mol/L was regarded as successful establishment of the diabetes model. After 14 days of injection, a von Frey fiber pain meter (Stoelting, Wood Dale, USA) was used for measurement of the 50% paw withdrawal threshold (PWT), and 50% PWT < 4 g was regarded as successful establishment of the DPN model. The rats in the control group received daily injections of normal saline with the same volume.

For the DPN and *miR-221* inhibitor or DPN and inhibitor NC group, the *miR-221* inhibitor was designed and synthesized by GeneChem Corp. (Shanghai, China). The sequence of the *miR-221* inhibitor was: 5′-GAAACCCAGCAGACAAUGUAGCU-3′. The construction and packaging of the lentivirus of the *miR-221* inhibitor (lenti-miR-221-inhibitor) and lenti-miR-NC were accomplished by GeneChem Corp. Briefly, miRNA oligos with the *miR-221* inhibitor/NC sequence were synthesized and subcloned into the pcDNA6.2™-GW/EmGFP-miR vector (Invitrogen, Carlsbad, USA). The lenti-miR-221-inhibitor/NC vector was obtained after att B and att P mediated recombination (BP reaction) between the miRNA vector and pDONR221 vector, and att L and att R mediated recombination (LR reaction) between the entry vectors and pLenti6.3/V5-dest. The lenti-miR-221-inhibitor/NC vector was then packaged with active titer $2 \times 10^8$ TU/mL. The rats the in DPN and *miR-221* inhibitor/NC group were DNP rats who received tail vein injection of 100 μL lenti-miR-221-inhibitor/NC vectors ($2 \times 10^8$ TU/mL). Treatment was conducted immediately after injection of STZ. All experiments were repeated in triplicate.

## Measurement of PWT and PWL

The PWT was measured using a von Frey fiber pain meter (Stoelting). Briefly, rats were placed in a transparent plexiglas box with a hole of $0.5 \times 0.5$ cm$^2$ in the bottom. The plantar of the rats was stimulated by gradually increasing the buckling force from 0.57 g. The force of the leg retraction reaction was regarded as the PWT and 50% PWT was calculated. Each animal was evaluated 5 times. The paw withdrawal latency (PWL) was measured using an automatic thermal pain stimulator (BMC-410C; Institute of Biomedical Engineering, Chinese Academy of Medical Sciences, Beijing, China). Briefly, rats were put on a glass plate and exposed to thermal radiation. The time from the beginning of irradiation to the emergence of leg raising avoidance was regarded as the PWL. Each animal was evaluated 5 times.

## Extraction and identification of serum exosomes

Blood samples were obtained from the rats after 14 days of treatment. Samples were centrifuged at 3000 × g at 4°C for 5 min. The serum exosomes were extracted using ExoQuick Exosome Precipitation Solution (ExoQuick; System Biosciences, Palo Alto, USA) in strict adherence with the manufacturer's instructions. For identification of the extracted exosomes, a flow cytometer (Beckman Coulter, Brea, USA) was used for measurement of the surface biomarkers CD63, CD90, CD45, and CD34. Briefly, acetaldehyde/sulfate latex beads (4 μM) were added into 30 μg extracted exosomes to achieve 100 μL. After adding 1 mL of phosphate-buffered saline (PBS) and incubation for 2 h, glycine (100 mmol) was added and the samples were incubated with primary antibodies of anti-CD63 (ab108950; Abcam, Cambridge, USA), anti-CD90 (ab226; Abcam), anti-CD45 (ab10558; Abcam), and anti-CD34 (ab81289; Abcam) at 4°C overnight. After incubation with the corresponding secondary antibody Goat Anti-Rabbit IgG H&L (horseradish peroxidase (HRP); ab205718; Abcam) at 37°C for 30 min, the biomarkers were analyzed using flow cytometry (FCM).

For observation of the morphology of the extracted exosomes, the exosomes were also observed using a transmission electron microscope (Hitachi, Tokyo, Japan).

## Cell culture and transfection

For the in vitro DPN model, the SH-SY5Y cell line from American Type Cell Culture (ATCC, Manassas, USA) was treated with 50 mmol/L of D-glucose (Sigma-Aldrich, St. Louis, USA). Cells were cultured in Dulbecco's modified Eagle's medium (DMEM; Gibco, Gaithersburg, USA) with 10% fetal bovine serum (FBS; Gibco), 100 IU/mL of penicillin, and 100 μg/mL of streptomycin at 37°C with 5% $CO_2$. Normal cells were treated with 5 mmol/L D-glucose.

For cell transfection, cells were transfected with *miR-221* inhibitor/mimics or inhibitor/mimics NC, as well as si-*SOCS3* or si-NC (all 5 nM) using Lipofectamine 3000 (Invitrogen, Carlsbad, USA) in serum-free Opti-MEM medium (Gibco) according to the manufacturer's instructions. The *miR-221* mimics/inhibitor, mimics/inhibitor NC, si-*SOCS3*, and si-NC were designed and synthesized by GeneChem Corp.

## RT-qPCR

Total *SOCS3* RNA was extracted from the serum samples or cells using TRIzol reagent (Thermo Fisher Scientific, Waltham, USA). The extraction of *miR-221* was performed using a mirVana miRNA isolation kit (Ambion, Austin, USA) strictly according to the manufacturer's instructions. RNA concentration was determined using a NanoDrop ND-1000 spectrophotometer (NanoDrop Technologies,

Wilmington, USA). The TaqMan® RNA Reverse Transcription Kit (Applied Biosystems, Foster City, USA) was used to convert RNA into cDNA. The TaqMan® MicroRNA Reverse Transcription Kit (Applied Biosystems) was used for reverse transcription of miRNA. The SYBR Premix Ex Taq™ II Kit (Solarbio Science & Technology Co. Ltd., Beijing, China) was used for reverse-transcription quantitative polymerase chain reaction (RT-qPCR) in an ABI StepOnePlus system (Applied Biosystems). The thermocycling conditions were as follows: initial activation step at 95°C for 15 min, 40 cycles, denaturation at 94°C for 15 s, annealing at 55°C for 30 s, and extension at 72°C for 30 s. Primers are listed Table 1. The relative RNA levels were calculated using the $2^{-\Delta\Delta Cq}$ method. *U6* and *GAPDH* were used as internal controls for *miR-221* and *SOCS3*, respectively.

Table 1. Sequences used in PCR

| Genes | Sequence |
|---|---|
| *miR-221* | F 5'-CAGCATACATGATTCCTTGTGA-3' R 5'-CTTTGGTGTTTGAGATGTTTGG-3' |
| *SOCS3* | F 5'- CCTGCGCCTCAAGACCTTC-3' R 5'-GTCACTGCGCTCCAGTAGAA-3' |
| *GAPDH* | F 5'-AGCGAGCATCCCCCAAAGTT -3' R 5'-GGGCACGAAGGCTCATCATT-3' |
| *U6* | F 5'-TGCGGGTGCTCGCTTCGGCAGC-3' R 5'-CCAGTGCAGGGTCCGAGGT-3' |

## Western blotting

Western blotting was used to measure the protein levels of *SOCS3*, bradykinin (BK) and prostaglandin E2 (PEG2). Proteins were extracted from serum samples or cells using radioimmunoprecipitation assay (RIPA) buffer (Vazyme Biotec Co. Ltd., Nanjing, China) and the concentrations were determined using a BCA assay kit (Sigma-Aldrich). After being subjected to 10% sodium dodecyl sulfate polyacrylamide gel electrophoresis (SDS-PAGE) and transferred to polyvinylidene difluoride (PVDF) film, samples were blocked using non-fat milk at room temperature for 1 h. The same samples were then incubated with primary antibodies of anti-*SOCS3* (ab16030; Abcam), PEG2 (ab2318; Abcam) and BK (ab47864, Abcam) at 4°C overnight followed by incubation with the corresponding secondary antibody (Goat Anti-Rabbit IgG H&L, ab205718; Abcam). The films were scanned using the Pierce ECL Western Blotting Substrate (Pierce, Shanghai, China) and analyzed using a Bio-Rad gel imaging system (Bio-Rad, Hercules, USA).

## Dual luciferase reporter assay

The dual luciferase reporter assay was performed to confirm the *SOCS3* 3'-UTR as a target of *miR-221*. Briefly, the wild-type (WT) *SOCS3* 3'-UTR or mutant (Mut) type

was amplified and sub-cloned into a pGL4.10 luciferase reporter vector and the cells were transfected with *miR-221* mimics, inhibitor or mimics/inhibitor NC using Lipofectamine 3000 (Invitrogen). Luciferase assays were performed using a Bright-Glo™ Luciferase Assay System (Promega, Madison, USA) after 48 h of transfection and the luciferase activity was normalized to the values of Renilla luciferase activity.

## Measurement of PEG2, BK, IL-6, IL-1β, and TNF-α

Serum or cell supernatant levels of PEG2, BK, interleukin (IL)-6, IL-1β, and tumor necrosis factor alpha (TNF-α) were measured with enzyme-linked immunosorbent assay (ELISA) according to the manufacturer's instructions using commercial kits: Prostaglandin E2 ELISA Kit (Abcam); Bradykinin ELISA Kit (Abcam); Interleukin 6 (Sandwich ELISA) ELISA Kit (LSBio, Inc.); Interleukin 1β (Sandwich ELISA) ELISA Kit (LSBio, Inc.); and TNF-α ELISA Kit (LSBio, Inc.).

## Statistical analyses

Data are expressed as the mean ± standard deviation (SD). Comparisons were conducted using one-way analysis of variance (ANOVA) followed by the Tukey's post hoc test. Findings were considered to be statistically significant when the p-value was less than 0.05. All analyses were performed using SPSS v. 18.0 (SPSS Inc., Chicago, USA).

# Results

## *MiR-221* was upregulated in serum-extracted exosomes in STZ-induced DPN rats

First, the exosomes extracted from the serum taken from the rats were identified. The morphology of the exosomes was photographed and the mean diameter was about 70 nm (Fig. 1A,B). Flow cytometry and western blotting results showed that CD63 and CD90 were positively expressed, while CD45 and CD34 were negatively expressed in the exosomes (Fig. 1C,D), indicating the successful extraction of the exosomes. Next, the expression of *miR-221* was determined using RT-qPCR. It was observed that *miR-221* was markedly upregulated in the serum exosomes of the DPN rats (Fig. 1E), suggesting that *miR-221* is abnormally expressed and might play a role in DPN.

## Inhibition of *miR-221* reduced the pain condition of STZ-induced DPN rats

To investigate the role of *miR-221* in DPN, we injected the lenti-miR-221 inhibitor into the rats and observed alterations in their pain condition. As shown in Fig. 2A, the blood glucose level increased remarkably in DPN rats compared with controls ($p < 0.05$). Induction of the lenti-miR-221 inhibitor significantly decreased the expression of *miR-221* in DPN rats compared with the NC group ($p < 0.05$, Fig. 2B). Both 50% PWT and PWL values were markedly decreased in DPN rats compared with controls



**A**

**B**

**C**

**D** CD90, CD63, CD34, CD45, GAPDH

**E**
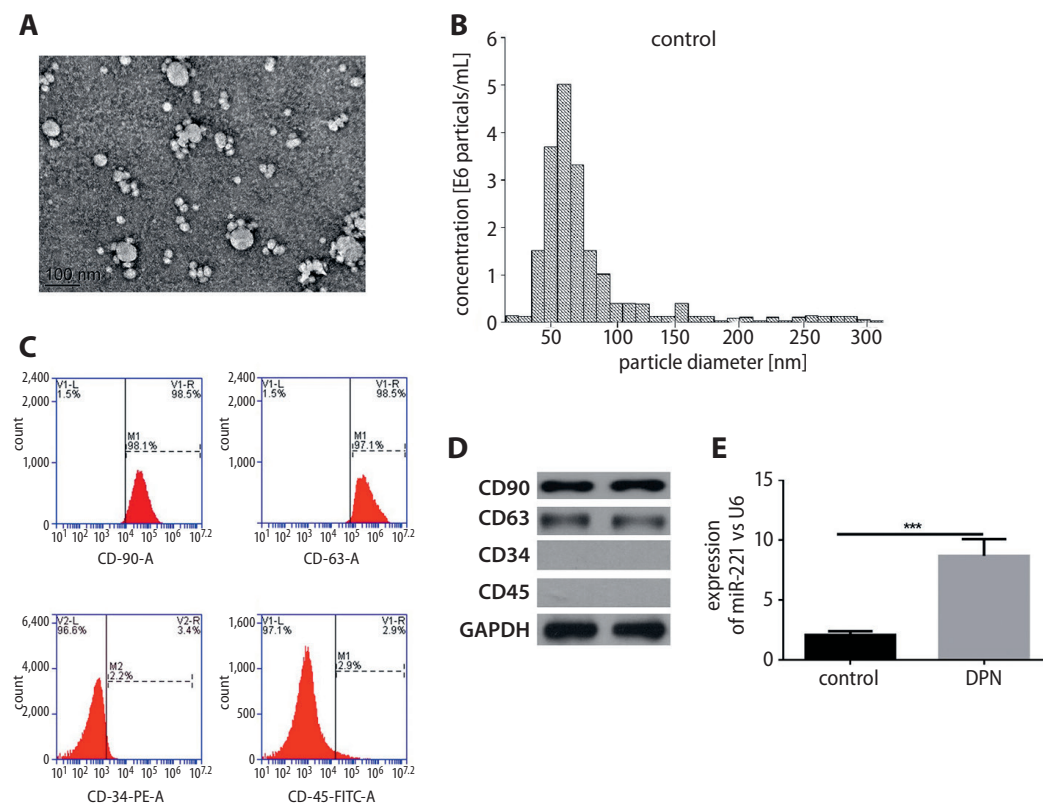
Fig. 1. *MiR-221* was upregulated in serum-extracted exosomes from STZ-induced DPN rats

A. Morphology of serum-extracted exosomes under TEM (100 nm); B. Distribution of the diameters of exosomes; C. FCM results for surface biomarkers of CD90, CD63, CD34, and CD45; D. Protein levels of CD90, CD63, CD34, and CD45 measured with western blotting; E. Expression of *miR-221* in serum-derived exosomes from DPN and control rats; *** $p < 0.001$.
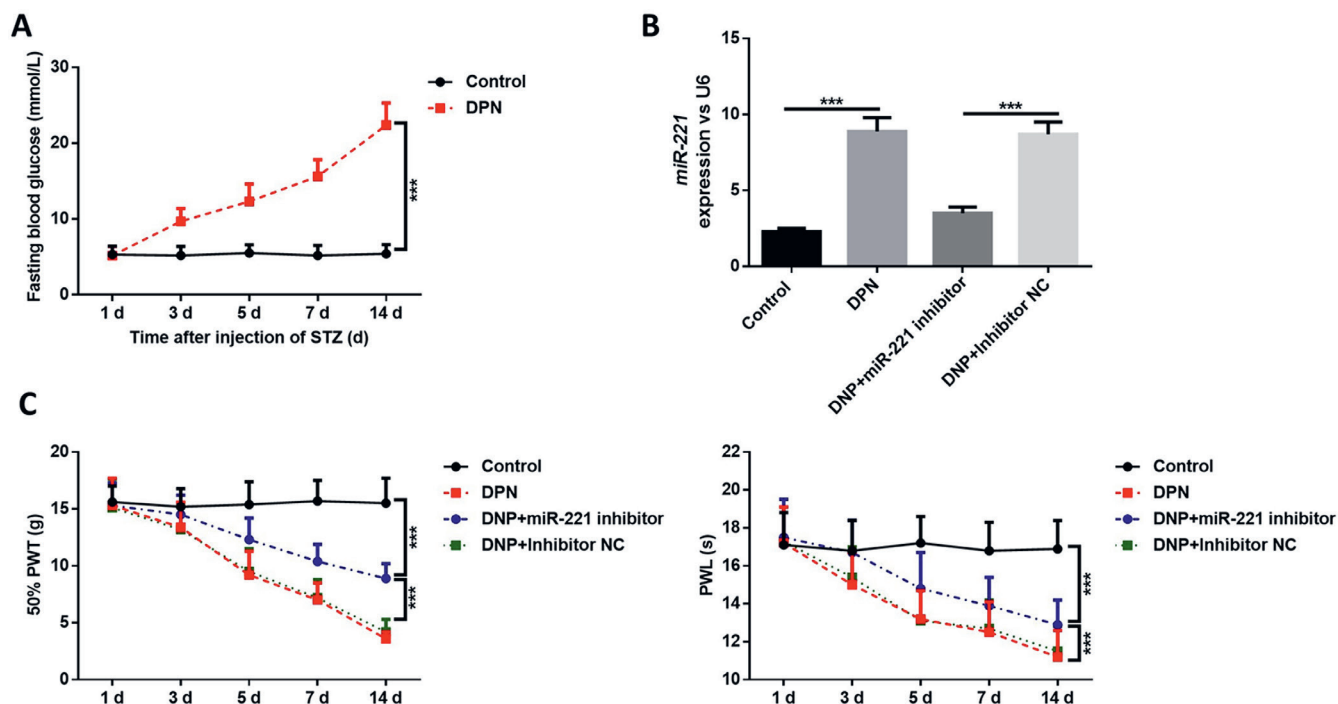
**Fig. 2.** Inhibition of *miR-221* reduced the pain condition of STZ-induced DPN rats

A. Blood glucose levels for DPN and control rats; B. Expression of *miR-221* in serum-derived exosomes from different groups of rats. C. 50% PWT and PWL were evaluated in different groups of rats; *** p < 0.001.

(p < 0.05, Fig. 2C). When *miR-221* was inhibited, both the 50% PWT and PWL values were significantly increased compared with the NC group (p < 0.05). These results indicated that inhibition of *miR-221* improved the pain condition of DPN rats.

## Inhibition of *miR-221* activated the expression of *SOCS3* but suppressed the expression of NF-κB and inflammation factors in STZ-induced DPN rats

To further reveal the effects of inhibiting *miR-221* in DPN, the serum protein levels of NF-κB and inflammation factors were evaluated. It was found that DPN treatment markedly decreased the expression of *SOCS3* and increased the expression of NF-κB (p < 0.05, Fig. 3A). However, knockdown of *miR-221* significantly reversed these effects. Furthermore, knockdown of *miR-221* remarkably decreased the expression of PEG2, BK, IL-6, IL-1β, and TNF-α compared with the NC group, which was increased by STZ treatment in DPN rats (p < 0.05, Fig. 3B). Taken together, these results indicate that knockdown of *miR-221* also decreased the expression of inflammation-related factors in DPN and that the downregulation of *SOCS3* might be involved in this process.

## *MiR-221* directly targeted and negatively regulated *SOCS3*

Next, the binding mode between *miR-221* and *SOCS3* was confirmed. The interaction between *miR-221* and *SOCS3* was predicted using TargetScan v. 7.2 (http://www.targetscan.org/vert_72) and is shown in Fig. 4A. The dual luciferase reporter assay showed that luciferase activity significantly decreased when transfected with *miR-221* mimics and significantly increased when transfected with the *miR-221* inhibitor in WT-*SOCS3* (p < 0.05 compared with the NC group, Fig. 3B). However, no significant difference was found in Mut-*SOCS3*. The mRNA and protein expressions of *SOCS3* were also determined. As shown in Fig. 3C,D, inhibition of *miR-221* markedly increased the expression of *SOCS3*, while overexpression of *miR-221* led to significant downregulation of *SOCS3* compared with the NC group (p < 0.05). These results indicate that *miR-221* directly targeted and negatively regulated *SOCS3*.

## Inhibition of *miR-221* suppressed inflammatory factors through regulation of *SOCS3* in high glucose-induced SY5Y cells

Lastly, *miR-221* and *SOCS3* were both suppressed in high glucose-induced SH-SY5Y cells and the expression of inflammatory factors was evaluated. It was found that the *SOCS3* mRNA and protein expressions

628

X. Wu et al. Investigating the role of *miR-221* in DPN
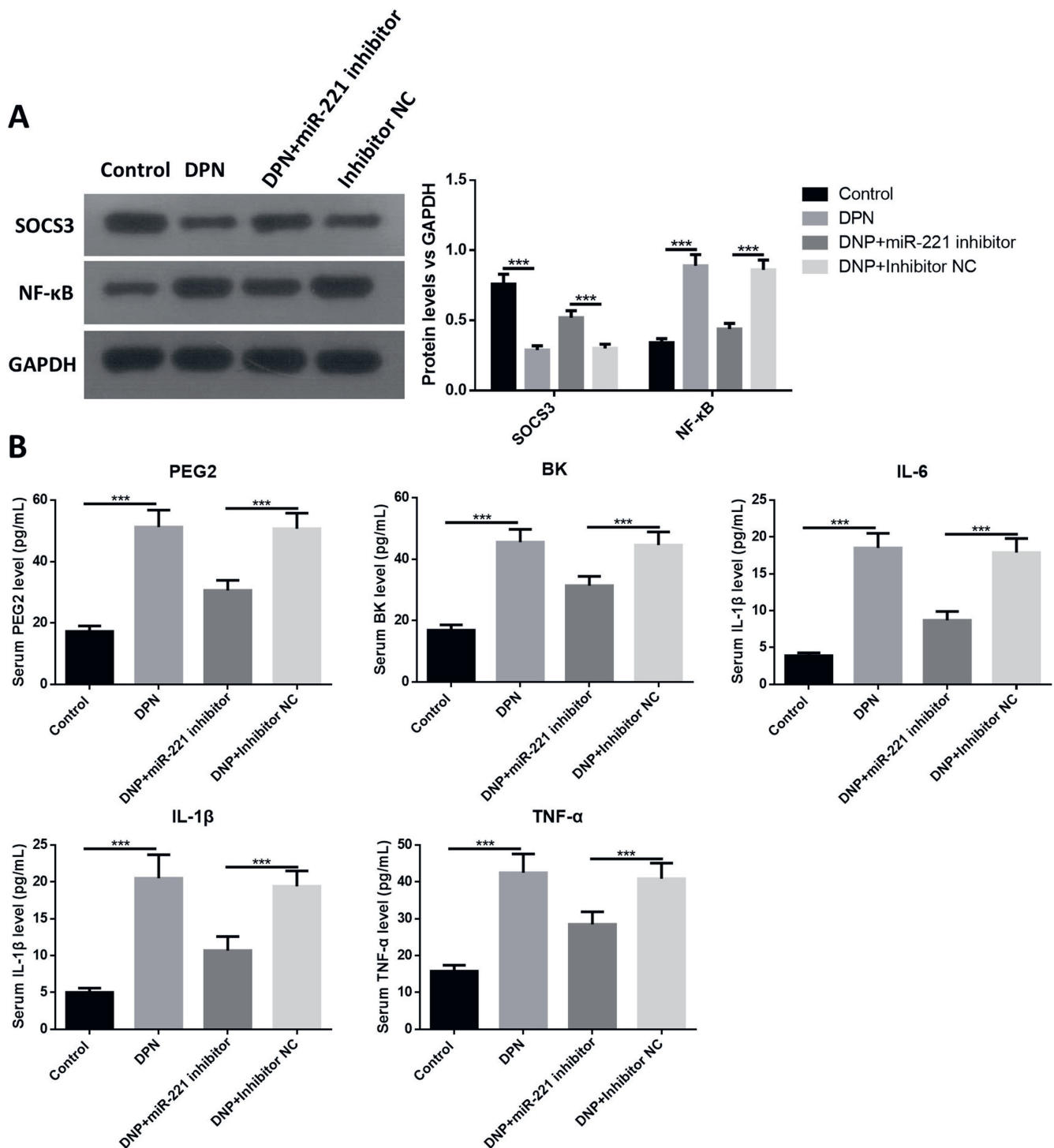


**Fig. 3.** Inhibition of *miR-221* activated the expression of *SOCS3* while suppressing the expression of NF-κB and inflammation factors in STZ-induced DPN rats

A. Serum protein levels of *SOCS3* and NF-κB in different groups of rats; B. Serum PEG2, BK, IL-6, IL-1β, and TNF-α measured using ELISA; *** p < 0.001.

were remarkably decreased in high glucose-induced cells compared with controls, while the expression of *miR-221* was remarkably upregulated in high glucose-induced cells (p < 0.05, Fig. 5A,B). However, the suppression of *miR-221* markedly downregulated the expression of *miR-221* and upregulated the expression of *SOCS3* in high glucose-induced cells (p < 0.05). Co-transfection of the *miR-221* inhibitor and si-*SOCS3* significantly

reversed the effects of the *miR-221* inhibitor. Furthermore, suppression of *miR-221* decreased the inflammatory levels of PEG2, BK, IL-6, IL-1β, and TNF-α, which were increased by high glucose. Inhibition of *SOCS3* significantly reversed this effect (Fig. 5C). These results suggest that knockdown of *miR-221* suppressed high glucose-induced inflammatory factors through up-regulation of *SOCS3*.

**A**

Position 1243-1250 of SOCS3 3' UTR

5' ...UGAC**AAUUUAC**AGGAAUGUAGCA...

|||||||

hsa-miR-222-3p

3'    UGGGUCAUCGGUCUACAUCGA

**B**



**C**



**D**



Fig. 4. *MiR-221* directly targeted and negatively regulated *SOCS3*

A. Binding mode between *miR-221* and *SOCS3* predicted by TargetScan v. 7.2; B. Luciferase activity assessed with the dual luciferase reporter assay; C. Expression of *miR-221* and *SOCS3* in different groups of SY5Y cells measured using RT-qPCR; *** p < 0.001.

## Discussion

The DPN is one of the most common complications of diabetes. However, the molecular mechanisms of DPN remain unclear. In the present study, we demonstrated for the first time that *miR-221* is upregulated in DPN in vivo and in vitro models, and that inhibition of *miR-221* improves DPN through targeting *SOCS3*.

The relationship between *miR-221* and diabetes has been noted in previous research. Lightell et al. demonstrated that *miR-221* and *miR-222* were upregulated in diabetes and that upregulation could promote intimal hyperplasia in diabetic mice.[12] Qian et al. showed that inhibition of cell autophagy induced by *miR-221* resulted in aggravation of diabetic cardiac hypertrophy.[13] All of these results suggest that *miR-221* is associated with aggravation of diabetes

Fig. 5. Inhibition of *miR-221* suppressed inflammatory factors through regulation of *SOCS3* in high glucose-induced SY5Y cells

A. Expression of *miR-221* and *SOCS3* in different groups of SY5Y cells measured using RT-qPCR; B. Protein levels of *SOCS3* in different groups of SY5Y cells measured using western blotting; C. Levels of PEG2, BK, IL-6, IL-1β, and TNF-α measured using ELISA; *** p < 0.001.

and its complications. In recent research, it was found that lncRNA GAS5 suppressed the proliferation and fibrosis of glomerular mesangial cells in diabetic nephropathy rats by targeting *miR-221* and negatively regulated its expression.[14] In a clinical study, Liu et al. demonstrated that *miR-221* is also upregulated in diabetic retinopathy (DR) and has potential as a biomarker for DR.[15] In a 2020 study, Fan et al. found that *miR-221* and *miR-222* could suppress the ability of islet cells to secrete insulin in a mouse model.[16] These studies further indicate that *miR-221* plays a role as a promotor in diabetes. However, the role of *miR-221* in DPN has not been shown. In the present study, we confirmed that miR-221 was upregulated in a DPN rat model and that inhibition of *miR-221* improved the pain condition of DPN rats and inhibited inflammatory factors.

The relationships among *miR-221*, inflammation and pain have been previously reported. It was found that *miR-221* can activate NF-κB by inhibition of A20, and that NF-κB is a key factor in inducing inflammatory factors.[17] Wang et al. demonstrated that inhibition of *miR-221* improved lipopolysaccharide (LPS)-induced inflammation in lung injury by suppressing SOCS1/NF-κB signaling.[18] In a study of pain condition, Xia et al. found that inhibition of *miR-221* improved neuropathic pain by inhibition of suppressor of cytokine signaling 1.[19] In our study, we also demonstrated that inhibition of *miR-221* improved pain condition in DPN rats and suppressed levels of inflammatory factors.

The *SOCS3* is considered an inflammation suppressor and is also associated with diabetes. Research has shown that *SOCS3* can suppress the expression of the inflammatory factors IL-1, IL-6 and tumor growth factor beta (TGF-β), as well as the inflammation signaling-related factors NF-κB and TGF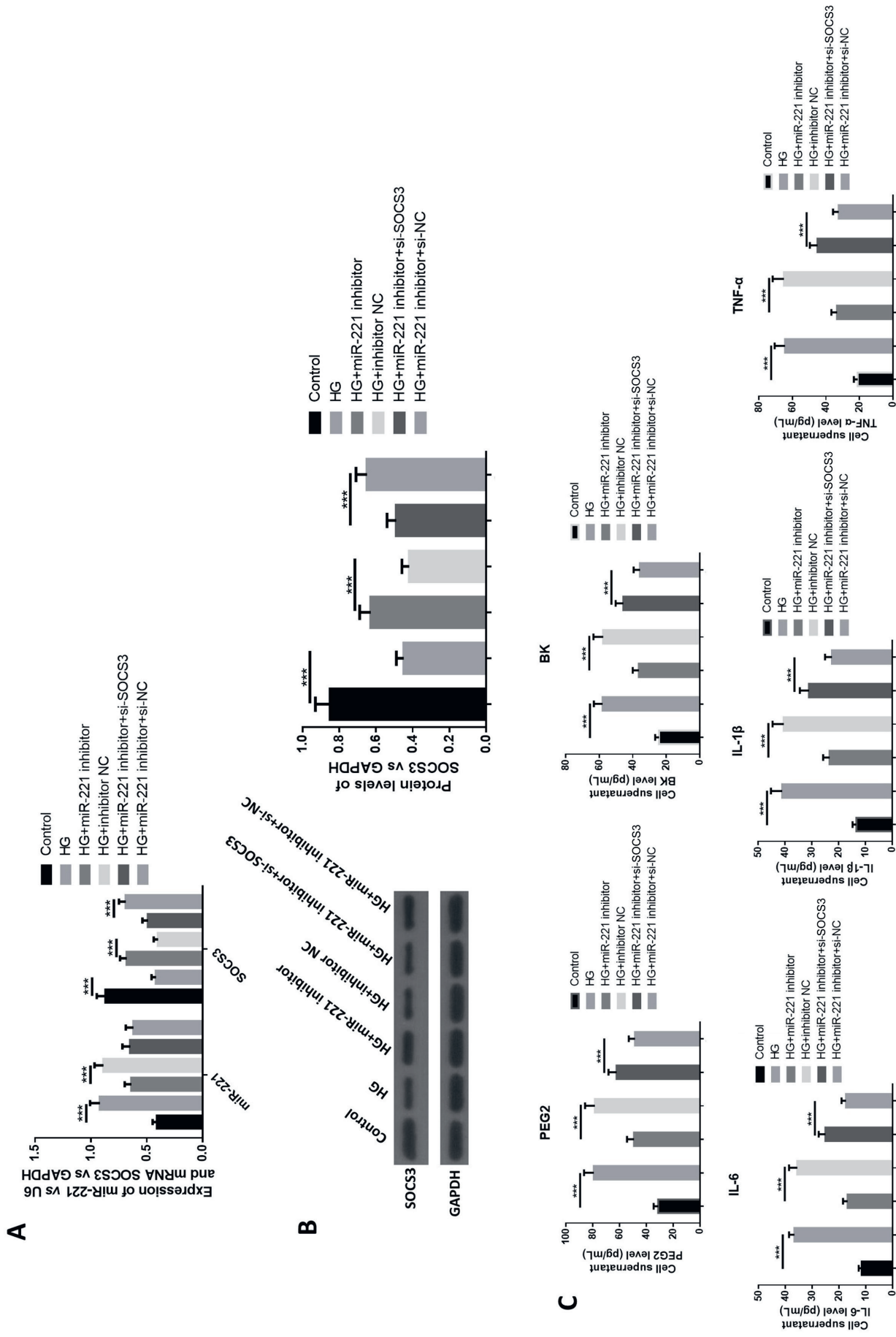β.[20,21] The *SOCS3* also shows anti-inflammation effects in LPS-induced lung inflammation, hepatitis B virus (HBV)-induced inflammation, oxidative stress, and encephalomyelitis.[22–24] Regarding the relationship between *SOCS3* and diabetes, Zhu et al. showed that paeoniflorin could upregulate the expression of *SOCS3* and inhibit inflammation, leading to suppression of matrix metalloproteinase-9 (MMP-9) and inflammatory factors in high glucose-induced renal clear cells.[25] Duan et al. demonstrated that overexpression of *SOCS3* improved high glucose-induced injury of pulmonary endothelial cells through inhibition of JAK2/STAT3 signaling.[26] Another study observed that inhibition of IL-6 improved diabetic nephropathy and that the process was associated with upregulation of *SOCS3*.[27] Taken together, these studies indicate that *SOCS3* might improve diabetes, potentially through its anti-inflammation effects. In the present study, we showed that *SOCS3* was downregulated in DPN rats and high glucose-induced cells, and that inhibition of *SOCS3* reversed the beneficial effects of the *miR-221* inhibitor in high glucose-induced cells. The relationship between *miR-221* and *SOCS3* has been reported in many other diseases, including prostate cancer, pancreatic cancer,

thrombocytosis, and bladder cancer.[28–30] However, this is the first confirmation that *miR-221* also targets *SOCS3* in DPN.

## Limitations

The present study has some limitations. The upstream molecules that regulate the *miR-221/SOCS3* axis are not sufficiently clear. Further research is also required to reveal the role of exosomes.

## Conclusions

We demonstrated that inhibition of *miR-221* reduced pain and suppressed inflammatory factors in DPN rats, and also inhibited inflammation in a high glucose-induced SH-SY5Y cell line. This research might provide some novel molecular mechanisms for the development of DPN treatment.

### ORCID iDs

Xiaole Wu  https://orcid.org/0000-0003-1002-309X
Xiaoyu Wang  https://orcid.org/0000-0002-8699-4469
Yiyu Yin  https://orcid.org/0000-0002-3607-8622
Lei Zhu  https://orcid.org/0000-0001-8407-0388
Fengchao Zhang  https://orcid.org/0000-0001-7689-3122
Jianping Yang  https://orcid.org/0000-0001-9694-8899

### References

1. Nathan CVS, Paul J, Abraham MM, Sasirekha M. Efficacy of low level laser therapy over conventional therapy on diabetic peripheral neuropathy: A pilot study. *Call for Editorial Board Members.* 2019;12(3):226.
2. Pop-Busui R, Boulton AJM, Feldman EL, et al. Diabetic neuropathy: A position statement by the American Diabetes Association. *Diabetes Care.* 2017;40(1):136–154. doi:10.2337/dc16-2042
3. Singh R, Kishore L, Kaur N. Diabetic peripheral neuropathy: Current perspective and future directions. *Pharmacol Res.* 2014;80:21–35. doi:10.1016/j.phrs.2013.12.005
4. Juster-Switlyk K, Smith AG. Updates in diabetic peripheral neuropathy. *F1000Research.* 2016;5:F1000 Faculty Rev-738. doi:10.12688/f1000 research.7898.1
5. Tesfaye S, Selvarajah D. Advances in the epidemiology, pathogenesis and management of diabetic peripheral neuropathy. *Diabetes Metabol Res Rev.* 2012;28:8–14. doi:10.1002/dmrr.2239
6. Dixit S, Maiya A, Shastry BA. Effect of moderate-intensity aerobic exercise on glycosylated haemoglobin among elderly patients with type 2 diabetes & peripheral neuropathy. *Indian J Med Res.* 2017;145(1):129–132. doi:10.4103/ijmr.IJMR_699_14
7. Teodoro JS, Nunes S, Rolo AP, Reis F, Palmeira CM. Therapeutic options targeting oxidative stress, mitochondrial dysfunction and inflammation to hinder the progression of vascular complications of diabetes. *Front Physiol.* 2019;9:1857. doi:10.3389/fphys.2018.01857
8. Sifuentes-Franco S, Pacheco-Moisés FP, Rodríguez-Carrizalez AD, Miranda-Díaz AG. The role of oxidative stress, mitochondrial function, and autophagy in diabetic polyneuropathy. *J Diabetes Res.* 2017; 2017:1673081. doi:10.1155/2017/1673081
9. Kozomara A, Birgaoanu M, Griffiths-Jones S. miRBase: From microRNA sequences to function. *Nucleic Acids Res.* 2019;47(D1):D155–D62. doi:10.1093/nar/gky1141
10. Oh SE, Park HJ, He L, Skibiel C, Junn E, Mouradian MM. The Parkinson's disease gene product DJ-1 modulates *miR-221* to promote neuronal survival against oxidative stress. *Redox Biol.* 2018;19:62–73. doi:10.1016/j.redox.2018.07.021

11. Fornari F, Pollutri D, Patrizi C, et al. In hepatocellular carcinoma *miR-221* modulates sorafenib resistance through inhibition of caspase-3-mediated apoptosis. *Clin Cancer Res*. 2017;23(14):3953–3965. doi:10.1158/1078-0432.CCR-16-1464

12. Lightell DJ, Moss SC, Woods TC. Upregulation of *miR-221* and *miR-222* in response to increased extracellular signal-regulated kinases 1/2 activity exacerbates neointimal hyperplasia in diabetes mellitus. *Atherosclerosis*. 2018;269:71–78. doi:10.1016/j.atherosclerosis.2017.12.016

13. Qian LB, Jiang SZ, Tang XQ, et al. Exacerbation of diabetic cardiac hypertrophy in OVE26 mice by angiotensin II is associated with JNK/c-Jun/*miR-221*-mediated autophagy inhibition. *Oncotarget*. 2017;8(63):106661–106671. doi:10.18632/oncotarget.21302

14. Xiaoxu G, Bojin X, Wenwei X, Lili X, Shan H. Long noncoding RNA GAS5 inhibits cell proliferation and fibrosis in diabetic nephropathy by sponging *miR-221* and modulating SIRT1 expression. *Aging*. 2019;11(20):8745–8759. doi:10.18632/aging.102249

15. Liu HN, Li X, Wu N, et al. Serum microRNA-221 as a biomarker for diabetic retinopathy in patients associated with type 2 diabetes. *Int J Ophthalmol*. 2018;11(12):1889–1894. doi:10.18240/ijo.2018.12.02

16. Fan L, Shan A, Su Y, et al. *MiR-221/222* inhibit insulin production of pancreatic β-cells in mice. *Endocrinology*. 2019;161(1):bqz027. doi:10.1210/endocr/bqz027

17. Zhao D, Zhuang N, Ding Y, Kang Y, Shi L. *MiR-221* activates the NF-κB pathway by targeting A20. *Biochem Biophys Res Commun*. 2016;472(1):11–18. doi:10.1016/j.bbrc.2015.11.009

18. Wang T, Jiang L, Wei X, et al. Inhibition of *miR-221* alleviates LPS-induced acute lung injury via inactivation of SOCS1/NF-κB signaling pathway. *Cell Cycle*. 2019;18(16):1893–1907. doi:10.1080/15384101.2019.1632136

19. Xia L, Zhang Y, Dong T. Inhibition of microRNA-221 alleviates neuropathic pain through targeting suppressor of cytokine signaling 1. *J Mol Neurosci*. 2016;59(3):411–420. doi:10.1007/s12031-016-0748-1

20. Babon JJ, Varghese LN, Nicola NA. Inhibition of IL-6 family cytokines by *SOCS3*. *Semin Immunol*. 2014;26(1):13–19. doi:10.1016/j.smim.2013.12.004

21. Gao A, Van DTE. Role of suppressors of cytokine signaling 3 in bone inflammatory responses. *Front Immunol*. 2013;4:506. doi:10.3389/fimmu.2013.00506

22. Yan C, Ward PA, Wang X, Gao H. Myeloid depletion of *SOCS3* enhances LPS-induced acute lung injury through CCAAT/enhancer binding protein δ pathway. *FASEB J*. 2013;27(8):2967–2976. doi:10.1096/fj.12-225797

23. Yuan K, Lei Y, Chen HN, et al. HBV-induced ROS accumulation promotes hepatocarcinogenesis through Snail-mediated epigenetic silencing of *SOCS3*. *Cell Death Differ*. 2016;23(4):616–627. doi:10.1038/cdd.2015.129

24. Yan Z, Yang W, Parkitny L, et al. Deficiency of *SOCS3* leads to brain-targeted experimental autoimmune encephalomyelitis via enhanced neutrophil activation and ROS production. *JCI Insight*. 2019;4(9):e126520. doi:10.1172/jci.insight.126520

25. Zhu SH, Liu BQ, Hao MJ, et al. Paeoniflorin suppressed high glucose-induced retinal microglia MMP-9 expression and inflammatory response via inhibition of TLR4/NF-κB pathway through upregulation of *SOCS3* in diabetic retinopathy. *Inflammation*. 2017;40(5):1475–1486. doi:10.1007/s10753-017-0571-z

26. Duan WN, Xia ZY, Min L, Qian S, Yan L. Protective effects of *SOCS3* overexpression in high glucose-induced lung epithelial cell injury through the JAK2/STAT3 pathway. *Mol Med Rep*. 2017;16(3):2668–2874. doi:10.3892/mmr.2017.6941

27. Wu R, Liu X, Yin J, Wu H, Wang F. IL-6 receptor blockade ameliorates diabetic nephropathy via inhibiting inflammasome in mice. *Metabolism*. 2018;83:18–24. doi:10.1016/j.metabol.2018.01.002

28. Kneitz B, Krebs M, Kalogirou C, et al. Survival in patients with high-risk prostate cancer is predicted by *miR-221*, which regulates proliferation, apoptosis, and invasion of prostate cancer cells by inhibiting IRF2 and *SOCS3*. *Cancer Res*. 2014;74(9):2591–2603. doi:10.1158/0008-5472.CAN-13-1606

29. Liu B, Wu S, Ma J, et al. lncRNA GAS5 reverses EMT and tumor stem cell-mediated gemcitabine resistance and metastasis by targeting *miR-221/SOCS3* in pancreatic cancer. *Mol Ther Nucleic Acids*. 2018;13:472–482. doi:10.1016/j.omtn.2018.09.026

30. Navarro A, Pairet S, Alvarez-Larrán A, et al. *MiR-203* and *miR-221* regulate *SOCS1* and *SOCS3* in essential thrombocythemia. *Blood Cancer J*. 2016;6(3):e406. doi:10.1038/bcj.2016.10

# PRF versus xenograft in sinus augmentation in case of HA-coating implant placement: A 36-month retrospective study

Sebastian Dominiak[1,C–F], Ewa Karuga-Kuźniewska[2,C], Paweł Popecki[1,E], Paweł Kubasiewicz-Ross[1,A–F]

[1] Department of Oral Surgery, Wroclaw Medical University, Poland

[2] Department of Epizootiology and Clinic of Birds and Exotic Animals, Faculty of Veterinary Medicine, Wroclaw University of Environmental and Life Sciences, Poland

A – research concept and design; B – collection and/or assembly of data; C – data analysis and interpretation;
D – writing the article; E – critical revision of the article; F – final approval of the article

**Address for correspondence**
Sebastian Dominiak
E-mail: sebastian.dominiak95@wp.pl

## Abstract

**Background.** Sinus lift with a simultaneous implant placement in the residual maxilla is a common technique used worldwide. Nevertheless, choosing an ideal grafting material remains an object of dispute. The use of an autologous blood-derived graft, known as platelet-rich fibrin (PRF), has not yet been recognized to be as good as xenografts and alloplastic materials. However, initial results have been promising.

**Objectives.** To conduct a clinical and radiological comparison of implantation with a simultaneous sinus lift using xenograft or PRF clots.

**Materials and methods.** Thirty sinus lifts with simultaneous implantation were conducted using a lateral window approach and the tent pole technique, with xenograft (group 1 ($G_1$)) or PRF (group 2 ($G_2$)) as a filling material. To be included in the study, patients must have had an alveolar ridge height of 4−5 mm, no signs of inflammatory processes, good oral hygiene, and no other grafting procedures performed in region of implant insertion. In each case, the measurements taken were probing pocket depth (PPD), height of keratinized tissue (HKT), clinical attachment level (CAL), recession depth/width (RD/RW), and, on panoramic X-rays, marginal bone loss (MBL), grafted sinus high (GSH), and bone gain (BG). Pre- and post-operative treatment was applied to reduce the chance of infection.

**Results.** During the study, 30 implants (hydroxyapatite-coated implants manufactured by SGS − 10 mm in length and 4.2 mm in diameter) were placed. The survival rate of implants in both groups was 100% with no implant mobility, pain, paresthesia, or inflammatory processes in the direct vicinity of the implants observed, except in 1 patient. After 36 months of follow-up, the radiological assessments for $G_1$ were: GSH 4.5 mm, MBL 0.46 mm and BG 4.53 mm; and for $G_2$: 3.4 mm, 0.6 mm and 3.4 mm, respectively. Results of the clinical measurements were for $G_1$: HKT after 36 months ($HKT_{36}$) 2.46 mm, CAL 0.47 mm and PPD 2 mm; and for $G_2$: $HKT_{36}$ 3.13 mm, CAL 0.6 mm and PPD 2.07 mm.

**Conclusions.** After 3 years of follow-up, the results of sinus lifting solely using PRF with simultaneous implantation were promising, especially in terms of soft tissue management. Therefore, PRF can be regarded as an alternative to previously used materials.

**Key words:** implant, platelet-rich fibrin, sinus lift, growth factors, hydroxyapatite-coated implants

# Background

Implant treatment for patients with edentulous maxilla can only be performed when there is an adequate amount of good-quality bone tissue. Following tooth extraction, the bony socket undergoes a series of adaptive changes, in both the vertical and horizontal dimensions, in an attempt to reduce bone height. It has been previously documented that the main result of alveolar bone resorption after tooth loss is the pneumatization of the maxillary sinus.[1,2] Implant-supported rehabilitation in such cases remains a challenge. However, the treatment of choice in these cases is sinus augmentation.

The sinus augmentation procedure was first described by Tatum and was subsequently redesigned by Boyne and James.[3,4] Depending on the clinical situation, such as the height and width of the alveolar ridge, different types of the procedure can be pursued. For example, in cases with a height over 6 mm, transcrestal techniques can be conducted.[5] In contrast, when the bone level is insufficient, procedures with an approach from the lateral side of the sinus cavity are most commonly used. This technique creates space between the maxillary alveolar process and the elevated Schneiderian membrane, which is filled with various grafting materials to maintain adequate space for new bone formation.[3–5]

Various materials, including freeze-dried bone allograft, β-calcium phosphate tribasic (β-TCP) and xenografts, such as deproteinized bovine bone mineral (DBBM), have been proposed as bone substitutes that can be applied during the sinus augmentation procedure.[6] However, due to their lack of progenitor cells and growth factors, these materials allow for potential osteoconductive growth only. In order to improve the osteoinductivity of alloplastic materials and xenografts, the use autologous growth factors has been proposed.[7]

Platelet-rich plasma (PRP) was initially used for this purpose.[8] However, there are potential risks associated with usage of this material, as PRP contains synthetic anticoagulant materials (e.g., sodium citrate, ethylenediaminetetraacetic acid, or anticoagulant citrate dextrose solution A).[8–10] Other limitations of PRP application include a more time-consuming preparation and a rapid degradation of platelets that can result in a reduced release of growth factors. Because of these reasons, platelet-rich fibrin (PRF) was substituted for PRP in guided bone regeneration procedures.[9]

The PRF process, first described by Choukroun et al.[10] in 2001, begins with blood being centrifuged immediately after collection without anticoagulants. With this procedure, coagulation starts during centrifugation. Centrifugation divides the blood sample into 3 parts: a red blood cell base at the bottom, an acellular plasma as a supernatant and a PRF clot in between. The PRF clot is transformed into a membrane through compression, and contains the highest concentration of the platelets and more than half of the leukocytes from a 9-milliliter blood harvest. Within the PRF membrane, the platelets are tightly merged together within a fibrin mesh, and the enmeshed leukocytes remain alive and functional in the dense fibrin network.

The PRFs release a high amount of growth factors including transforming growth factor-β1 and β2 (TGFβ-1 and TGFβ-2), platelet-derived growth factor (PDGF), vascular endothelial growth factor (VEGF), insulin-like growth factor 1 and 2 (IGF-1 and IGF-2), fibroblasts growth factor (FGF), and matrix glycoproteins (such as thrombospondin-1) for at least 7 days in vitro.[10–12] The PDGF occurs in the form of both homodimers (PDGF-AA and PDGF-BB) and heterodimers (PDGF-AB), and influences the synthesis of DNA strains, inducing angiogenesis, chemotaxis, and mitogenesis of fibroblasts, osteoblasts and monocytes. It cooperates with IGFs, which, in turn, leads to the differentiation of fibroblasts into osteoblasts, further increasing the amount of bone collagen in osteoblasts. In turn, TGF-β1 and TGF-β2 stimulate the production of connective tissue, synthesis and maturation of the collagen fibers, angiogenesis, and cell differentiation. The TGF-β1 has an impact on the mineralization of regenerating cells, influencing the speed and quality of the process. In turn, VEGF influences the synthesis of DNA strains, impacting the differentiation of endothelial cells, while simultaneously activating the healing process. During the early stages of healing (1–2 weeks), PDGF-BB and IGF-1 play a key role by stimulating and accelerating the gathering of fibroblasts. Later on (2–3 weeks), inflammatory tissue is replaced by connective tissue and induces production of the collagen fibers, where EGF and FGF lead the way. The last part of healing, when cells differentiate into osteoblasts and their maturation occurs, is once again induced by IGF-1.[12,13]

In recent years, researchers have paid increased attention to the clinical results of PRF application in sinus augmentation procedures. However, a general consensus pertaining to the use of this material has yet to be reached.[14,15]

# Objectives

The main aim of this study was to evaluate if PRF, used solely as a grafting material in sinus lifting procedures, is a reliable alternative to xenografts.

# Materials and methods

The data used in this study were collected via retrospective evaluation and were obtained through a well-known treatment. Thus, this study did not require approval of the bioethical committee.

## Patient selection

Thirty generally healthy patients (14 men, 16 women), aged 30–64 years, with atrophic maxilla due to missing teeth in the lateral aspects, and previously treated with

implant-supported oral rehabilitation, were included in the study. Other inclusion criteria included a apico-coronal height of 4–5 mm for the alveolar ridge in the region of the implant insertion during pre-surgical qualification, a minimal width of 7 mm for the alveolar ridge in the region of interest, approximal plaque index (API) ≤35, and plaque index (PI) ≤25. The exclusion criteria were previous grafting procedures in the area of interest and systemic or local diseases that could affect the healing or osteointegration processes. Smokers and patients with bruxism were excluded from the study as well.

Patients were randomly divided into 2 equal-sized groups. The 1st group ($G_1$) consisted of patients in whom the sinus lift was augmented with xenograft (Cerabone®; Botiss Biomaterials GmbH, Zossen, Germany). The 2nd group ($G_2$) consisted of patients solely receiving PRF as a grafting material.

## Implants

In both groups, electrochemically hydroxyapatite-coated implants SGS (SGS Dental Implant System Holding, St. Gallen, Switzerland) of the same size (10 mm in length, 4.2 mm in diameter) were used.

## PRF preparation

The PRF was prepared in accordance with Choukroun's protocol.[10] First, venous blood samples were collected from the patient into 10-milliliter tubes. Next, the samples were placed in a centrifuge (PRF PROCESSTM (CHOUKROUN DUO, Nice, France) and spun for 10 min at 3000 rpm. The PRF clot was then isolated from the erythrocytes fraction, 2 mm below platelets-rich layer. In order to obtain the desired PRF membrane, the PRF clots were put into a A-PRF™ box (Fida Tech, Copenhagen, Denmark) without any pressure applied.

## Surgical technique

In order to aid the procedure and successfully identify patients who needed sinus augmentation, preoperative cone-beam computed tomographic (CBCT) images were used to carefully measure the residual bone volume. All patients were given premedication for antibiotic prophylaxis (Augmentin; GSK, Brentford, UK; 2.0 g), and implants were placed on the day of sinus augmentation surgery as a one-stage procedure. The position of the implant insertion was within the premolar and molar region.

### Sinus augmentation with PRF

Under local anesthesia (4% articaine, 1 : 200000 Ubistesin; 3M, St. Paul, USA), a full-thickness mucoperiosteal flap with 2 releasing incisions was made. After creating an approach to the buccal wall of the maxillary sinus,

the smallest possible window was created with piezosurgery® white (Mectron Carasco, Genova, Italy) and constant water-cooling. The bone window was used as a new sinus floor, as it remained partly attached to the membrane. Next, the Schneiderian membrane was carefully elevated from the bottom of the sinus. The implant was then inserted into the alveolar arch with a low rpm rate to use tip of the implant as a tent pole to elevate the sinus sealing membrane, and an extra layer of the A-PRF was placed underneath. These latter procedures were carried out under constant eye control through created window, and the autogenous membranes were used to prevent perforations. The PRF membrane was applied to prevent further complications. When primary stabilization of the implant was satisfactory, PRF clots were placed around it to fill up the residual space completely. The PRFs were also positioned to cover the bony window, and the flap was sutured back with resorbable, monofilament 5-0 sutures (Monosyn B/Braun, Tuttlingen, Germany). The primary closure without tension was achieved by using horizontal mattress or continuous sutures. Postoperative treatment consisted of Eludril Classic® (Pierre Fabre, Paris, France) mouthwash for 2 weeks, 2 times per day, and an antibiotic cover (Augmentin; GSK; 2.0 g per day). If no complications were observed, the sutures were removed after 7–10 days.

### Sinus augmentation with xenograft

The operating procedures for creating access to the maxillary sinus were as described above. The procedure started to differ after the bone window was made. Here, the Schneiderian membrane was elevated, and the freshly created sub-sinus cavity was filled with xenograft. Implantation in this group was also conducted simultaneously. After obtaining primary stabilization in the residual alveolar arch, the approach to the sinus was closed with resorbable, monofilament 5-0 sutures. The full-thickness flap was sutured back without tension using horizontal mattress or continuous sutures. Postoperative management also included Eludril Classic® mouthwash for 2 weeks (2 times per day) and an antibiotic cover (Augmentin; GSK; 2.0 g per day). Sutures were removed after 7–10 days if there were no complications.

## Implant loading

All implants were non-submerged. After 6 months, loading of the implants was carried out. All implants were loaded with a splinted or non-splinted screwed restoration.

## Clinical evaluation

The assessment was based on a clinical examination, including probing pocket depth (PPD) measured around the implants in 4 measurement points, height of the keratinized tissue (HKT), clinical attachment level (CAL), and the recession depth/width (RD/RW). The evaluation

of HKT was performed on the day of surgery ($HKT_0$) and after 36 months from the implant loading ($HKT_{36}$). To calculate implant survival rate, criteria suggested by Albrektsson et al.[16] (individual unattached implant that is immobile when tested clinically; no evidence of peri-implant radiolucency; bone loss that is less than 0.2 mm annually after first year of service of the implant) and Buser et al.[17] (the absence of implant mobility; no pain or any subjective sensation and peri-implant infection; the absence of continuous radiolucency around the implants) were used.

## Radiological evaluation

At least 3 digital panoramic X-rays were taken for evaluation: 1st immediately after sinus augmentation, 2nd during the follow-up visit after 6 months after sinus augmentation and prior to loading the implant, and 3rd 36 months after implant loading. The X-rays were performed using Galileos® D3437 software (Sirona Dental, Erlangen, Germany). Radiological evaluation allowed for the assessment of 3 main parameters: marginal bone loss (MBL); grafted sinus high (GSH); and bone gain (BG).

To calculate MBL, the dimensions were first calibrated using the known parameters of implant, including diameter and length. Starting from the implant shoulder, distances were measured to the mesial and distal points of bone-to-implant contact, parallel to the implant axis. Both distal and mesial measurements were averaged. To report the change in the height of the grafted sinus, the lowest point of the original sinus floor (OSH) was calculated. The BG was finally calculated at 36-month follow-up based upon panoramic X-ray examination as a distance between OSH and the highest point of bone structure – GSH. All measurements were done by S.D., a junior member of the study team who was not involved in performing the implant surgeries.

## Statistical analysis

Statistical analysis was carried out using SPSS v. 25 (IBM Corp., Armonk, USA) In order to check the distribution of the examined variables and to test their compliance with the normal distribution, basic descriptive statistics were calculated and Shapiro–Wilk distribution normality tests were performed. Ultimately, the nonparametric Mann–Whitney U test was used to detect differences between groups in the following measurements: MBL, BG, PPD, HKT (measured immediately after surgeries, and after the 36-month follow-up period), CAL, RD, and RW. The global significance level for the study was $\alpha = 0.05$.

## Results

The implant survival rate in both groups was 100% at 36 months. For 1 case in the PRF group, PPD for 4 mm with accompanying bleeding was reported, although the implant

was stable. Mechanical and chemical debridement was applied in this case as a first option for peri-implantitis management. In the rest of the cases, implant mobility, pain, paresthesia, and inflammatory processes in the direct vicinity of the implants were not reported in either group. Thus, the cumulative success rate was calculated as 100% according to Albrektsson et al.[16] and 93% according to Buser et al.[17]

The mean GSH value was 3.4 mm for the PRF ($G_2$) group and was lower than that observed for the xenograft ($G_1$) group (4.5 mm). These findings were accompanied by poorer results for MBL and CAL in $G_2$ (0.6 mm and 0.53 mm, respectively) relative to $G_1$ (0.46 mm and 0.4 mm, respectively). In contrast, the initial HKT in $G_2$ was 3.4 mm, while in $G_1$ the pre-surgical HKT level was 2.93 mm. Detailed results from the clinical and radiological evaluations are reported separately for each group in Tables 1,2.

As the Shapiro–Wilk tests indicated that the variables were not normally distributed and exhibited kurtosis values usually surpassing the absolute value of 2, it was decided to use the nonparametric Mann–Whitney U test to examine group differences in site, PPD, $HKT_0$, $HKT_{36}$, CAL, RD, RW, MBL, and BG. The rank-biserial correlation (r) was used as a measure of the effect size. The results of Mann–Whitney U tests for each of the variables are reported in Table 3.

Three of the 9 conducted tests turned out to be statistically significant. The $HKT_{36}$ value in the $G_1$ group was significantly lower than that observed for $G_2$, and the effect factor r indicated a large effect. The RW value in the $G_1$ group was also significantly lower as compared to $G_2$, and the effect factor indicated a large effect. However, the BG value in $G_2$ was much lower than that observed in $G_1$, and the effect factor r also indicated a large effect.

## Discussion

The issue of maxillary sinus grafting is not new and has been evaluated by many authors before. Previously, using bone-substituting materials, xenografts have mostly proved effective. However, application of a xenograft in the sinus lifting procedure requires a long follow-up period due to relatively slow resorption of the biomaterial. Another disadvantage of using heterogenic or allogenic materials in this procedure is the necessity for evacuation in the case of complications. The ethical concerns associated with the aforementioned materials also cannot be depreciated. On the other hand, the alveolar recess of the maxillary sinus, due to sufficient blood supply and other anatomical properties, possesses a high osteoconductive potential. Thus, a sinus lift without grafted bone material or with an autologous graft is a very natural and attractive approach.[16]

The existing evidence-based literature is scarce in terms of the sole use of platelet concentrates in maxillary sinus augmentation. Evaluation of this procedure is hampered also by the fact that the majority of the existing studies

Table 1. Clinical and radiological results of patients included in group 1 ($G_1$)

| $G_1$ | Age/sex | Splinted or non-splinted | Site (tooth number) | PPD | $HKT_0$ | $HKT_{36}$ | CAL | RD | RW | MBL | BG |
|---|---|---|---|---|---|---|---|---|---|---|---|
| 1 | 45/M | N | 16 | 2 | 3 | 2 | 0 | 0 | 0 | 0 | 4 |
| 2 | 30/F | N | 16 | 2 | 2 | 3 | 1 | 1 | 0 | 1 | 5 |
| 3 | 66/M | N | 15 | 2 | 3 | 3 | 0 | 0 | 1 | 1 | 4 |
| 4 | 64/M | S | 25 | 2 | 4 | 3 | 0 | 0 | 0 | 0 | 5 |
| 5 | 48/F | S | 15 | 1 | 4 | 3 | 1 | 0 | 0 | 0 | 5 |
| 6 | 59/F | N | 16 | 2 | 3 | 2 | 0 | 0 | 0 | 0 | 5 |
| 7 | 52/F | S | 25 | 3 | 2 | 2 | 1 | 1 | 2 | 1 | 5 |
| 8 | 41/M | N | 26 | 2 | 2 | 2 | 1 | 1 | 1 | 1 | 4 |
| 9 | 48/F | S | 26 | 2 | 3 | 2 | 0 | 0 | 0 | 0 | 5 |
| 10 | 35/M | N | 15 | 3 | 3 | 3 | 1 | 1 | 0 | 1 | 4 |
| 11 | 48/F | S | 16 | 3 | 3 | 3 | 1 | 1 | 0 | 1 | 5 |
| 12 | 59/M | S | 26 | 2 | 4 | 3 | 1 | 0 | 0 | 0 | 5 |
| 13 | 56/F | S | 16 | 2 | 3 | 2 | 0 | 0 | 0 | 0 | 6 |
| 14 | 61/F | N | 15 | 1 | 3 | 2 | 0 | 0 | 0 | 0 | 3 |
| 15 | 38/M | N | 16 | 1 | 2 | 2 | 0 | 0 | 0 | 0 | 3 |
| Average | – | – | – | 2 | 2.933333 | 2.466667 | 0.466667 | 0.333333 | 0.266667 | 0.4 | 4.533333 |

$G_1$ – group 1; PPD – probing pocket depth; HKT – height of the keratinized tissue; CAL – clinical attachment level; RD – recession depth; RW – recession width; MBL – marginal bone loss; BG – bone gain.

Table 2. Clinical and radiological results of patients included in group 2 ($G_2$)

| $G_2$ | Age/sex | Splinted or non-splinted | Site (tooth number) | PPD | $HKT_0$ | $HKT_{36}$ | CAL | RD | RW | MBL | BG |
|---|---|---|---|---|---|---|---|---|---|---|---|
| 1 | 45/F | N | 16 | 3 | 4 | 4 | 1 | 1 | 2 | 1 | 3 |
| 2 | 57/M | N | 16 | 1 | 3 | 3 | 1 | 1 | 1 | 1 | 4 |
| 3 | 60/M | S | 26 | 1 | 4 | 3 | 1 | 1 | 2 | 1 | 5 |
| 4 | 55/M | N | 26 | 2 | 4 | 3 | 0 | 0 | 2 | 0 | 3 |
| 5 | 53/F | S | 25 | 2 | 3 | 3 | 0 | 0 | 2 | 0 | 4 |
| 6 | 63/F | S | 27 | 2 | 3 | 3 | 1 | 1 | 1 | 1 | 3 |
| 7 | 47/M | S | 26 | 2 | 3 | 3 | 0 | 0 | 2 | 0 | 2 |
| 8 | 41/F | N | 16 | 3 | 3 | 3 | 1 | 0 | 2 | 1 | 6 |
| 9 | 58/F | S | 15 | 2 | 4 | 4 | 0 | 0 | 2 | 0 | 4 |
| **10** | **55/M** | **S** | **16** | **4** | **3** | **3** | **3** | **1** | **1** | **2** | **4** |
| 11 | 38/F | N | 16 | 2 | 4 | 3 | 0 | 0 | 2 | 0 | 3 |
| 12 | 60/M | S | 16 | 2 | 4 | 4 | 0 | 0 | 2 | 0 | 3 |
| 13 | 44/F | S | 26 | 2 | 3 | 3 | 0 | 0 | 2 | 0 | 3 |
| 14 | 49/M | S | 25 | 1 | 3 | 2 | 1 | 1 | 1 | 1 | 2 |
| 15 | 59/F | N | 26 | 2 | 3 | 3 | 0 | 1 | 1 | 0 | 2 |
| Average | – | – | – | 2.066667 | 3.4 | 3.133333 | 0.6 | 0.466667 | 1.666667 | 0.533333 | 3.4 |

Bold – patient with bleeding; $G_2$ – group 2; PPD – probing pocket depth; HKT – height of the keratinized tissue; CAL – clinical attachment level; RD – recession depth; RW – recession width; MBL – marginal bone loss; BG – bone gain.

included only small cohorts of patients and short-term follow-up periods (6–12 months). Another difficulty in the assessment of platelet concentrate applications is the lack of control groups in the previous work.[18]

Anitua et al. were one of the first to conduct a retrospective study of platelet concentration application in maxillary sinus grafting with a long (36 months) follow-up period. When using short implants and a transcrestal approach, the alveolar bone height increased by 3.7 ±1.7 mm and 4.2 ±2.0 mm at 12 ±3 months and 35 ±11 months after surgery, respectively.[14] Previously, most studies included a shorter observation period. Toffler et al.[19] in a study

Table 3. Mann–Whitney U test results for each of the variables

| Variable | G₂ (n = 15) | | | | G₁ (n = 15) | | | | Z | p-value | R |
|---|---|---|---|---|---|---|---|---|---|---|---|
| | medium range | Me | SD | IQR | medium range | Me | SD | IQR | | | |
| Site | 17.90 | 25.00 | 5.20 | 10.00 | 13.10 | 16.00 | 4.91 | 10.00 | −1.56 | 0.118 | 0.29 |
| PPD | 15.60 | 2.00 | 0.80 | 0.00 | 15.40 | 2.00 | 0.66 | 0.00 | −0.07 | 0.944 | 0.01 |
| $HKT_0$ | 18.20 | 3.00 | 0.51 | 1.00 | 12.80 | 3.00 | 0.70 | 1.00 | −1.89 | 0.059* | 0.35 |
| $HKT_{36}$ | 19.70 | 3.00 | 0.52 | 0.00 | 11.30 | 2.00 | 0.52 | 1.00 | −3.00 | 0.003* | 0.55 |
| CAL | 15.73 | 0.00 | 0.83 | 1.00 | 15.27 | 0.00 | 0.52 | 1.00 | −0.17 | 0.868 | 0.03 |
| RD | 16.50 | 0.00 | 0.52 | 1.00 | 14.50 | 0.00 | 0.49 | 1.00 | −0.73 | 0.464 | 0.13 |
| RW | 22.00 | 2.00 | 0.49 | 1.00 | 9.00 | 0.00 | 0.59 | 0.00 | −4.32 | <0.001* | 0.79 |
| MBL | 16.20 | 0.00 | 0.64 | 1.00 | 14.80 | 0.00 | 0.51 | 1.00 | −0.50 | 0.616 | 0.09 |
| BG | 11.10 | 3.00 | 1.12 | 1.00 | 19.90 | 5.00 | 0.83 | 1.00 | −2.83 | 0.005* | 0.52 |

Asterisks indicate significant results; G₁ – group 1; G₂ – group 2; PPD – probing pocket depth; HKT – height of the keratinized tissue; CAL – clinical attachment level; RD – recession depth; RW – recession width; MBL – marginal bone loss; BG – bone gain; Me – median; SD – standard deviation; IQR – interquartile range.

on SLA implants with a 3-month follow-up reported a mean increase in the height of implant sites of 3.4 mm (range: 2.5–5 mm), while Diss et al.[20] in a 12-month follow-up on Astra Tech implants reported a mean endo-sinus BG of 3.2 ±1.5 mm. Aoki et al.[21] also reported a statistically significant mean BG in sandblasted acid-etched implants compared to hydroxyapatite implants, and Molemans et al.[22] reported a higher mean BG (5.4 ±1.5 mm) with the lateral sinus floor elevation approach compared to the transalveolar technique (3.4 ±1.2 mm).

The superiority of the lateral window technique was once again confirmed in a study by Mazor et al.,[23] where implants were placed in residual bone with heights between 1.5 mm and 6 mm (mean ± standard deviation (SD): 2.9 ±0.9 mm). The final bone gain with this procedure was very significant (between 7 mm and 13 mm (mean ±SD: 10.1 ±0.9 mm) at 6-month follow-up. In a similar study with a 6-month follow-up, Tajima et al.[24] observed a lower gain in mean residual alveolar bone height after the sinus floor elevation from 4.28 ±1.00 mm (range: 1.9–6.1 mm) prior to surgery to 11.8 ±1.67 mm (range: 9.1–14.1 mm) after surgery. The results of the sinus-lift procedure combined with PRF application also appear to remain stable with a longer follow-up. Simonpieri et al.[25] conducted a retrospective study with 2–6 years of observation and reported very stable results with between 8.5 mm and 12 mm of bone gain (mean ±SD: 10.4 ±1.2 mm) observed. These findings of very stable results for crestal bone height were confirmed by Pichotano et al.[26] In this study, 20 patients treated with SLA implants placed immediately with PRF sinus-grafting showed a bone gain of 8.5–12 mm (mean ±SD: 10.4 ±1.2 mm). Another study, including 27 patients who received 2 types of implants during the sinus-lift procedure, with PRF used solely as the grafting material, reported a bone gain of 4.38 mm and 4.00 mm for SLA and HA implants, respectively. The observation period in this latter study was 12 months.[27]

Similar to the abovementioned studies, the current work evaluated maxillary sinus grafting by radiographic assessment using pre- and post-surgical panoramic X-ray. In this study, a comparison of the effectiveness of solely used xenograft or PRF was carried out. However, some authors have suggested that PRF could be combined with xenograft to improve the osteoconductive properties of the graft. This combination may accelerate bone formation and promote wound healing. The mechanism that underlies both events could be the ability of PRF to increase blood flow in the sinus cavity and osteoblast formation via the release of growth factors. Pichotano et al.[28] showed that the addition of PRF to xenograft improves resorption rates when compared to xenograft alone (22.25% and 8.95%, respectively). Histomorphometric analysis showed an increased amount of newly formed bone when PRF was used compared with xenograft alone, and allowed, in turn, faster implant loading. However, Nizam et al.[29] reported no qualitative difference in histological analyses among groups of patients receiving xenograft alone or in combination with PRF. In all samples, a newly formed bone was in direct contact with the residual material. Similar radiographic bone height was observed in the augmented area, and the implant survival rate was 100% for both groups.

Retrospective studies based on clinical evaluations of sinus floor augmentation are even less common. Hadzik et al.[30] reported that the HKT value changed from 2.7 ±1.64 mm to 1.73 ±1.1 mm at 36 months following the direct placing of similar-sized SLA implants with sinus floor lifting + xenograft usage, a much bigger decline in comparison to the current results.

None of the implants were lost during the current study, including during the initial-surgical phase and over a 36-month follow-up period. According to the criteria proposed by Albrektsson et al.,[16] the success and survival rate was 100%, as no mobility of the implant or radiolucency was observed. Unlike the criteria proposed by Albrektsson et al.,[16] the criteria proposed by Buser et al.[17] include vertical bone loss and the presence of infection (peri-implantitis). This latter clinical evaluation allows for a more stringent assessment of the peri-implant hard

and soft tissue condition, which explains the lower success rate according to Buser et al.[17] For 1 case in $G_2$, PPD for 4 mm with accompanying bleeding was observed; thus, dropping the success rate for that group to 93% according to the criteria proposed by Buser et al.[17]

In a study on 114 HA-coated implants with a long (8–10 years) follow-up, Binahmed et al.[31] reported a survival rate in the maxilla of 70.59%. However, McGlumphy et al.[32] in a shorter follow-up study (5–7 years) on 429 HA-coated implants reported a much higher cumulative survival rate (96% at 5 years and 95% at 7 years of follow-up). The mean combined mesial/distal bone loss in this latter study was 1.2 mm in the mandible and 1.4 mm in the maxilla after 5 years of functional loading. Schwartz-Arad et al.[33] conducted a comparison study of HA-coated and commercially pure titanium implants with a 12-year follow-up. In this study, the reported total mean MBL was 1.07 ±2.16 mm. In addition, MBL was significantly lower with titanium implants (0.55 ±1.04 mm) compared to HA-coated implants (1.51 ±2.71 mm; p < 0.001). Furthermore, the total 12-year survival rate was 91.4%, and HA-coated implants had a significantly higher 12-year survival rate than titanium implants (93.2% compared to 89%; p < 0.03). Atia et al.[34] provided a comparison of the success rates according to Buser et al.[17] and Albrektsson et al.[16] for SLA implants placed in maxilla previously treated with PRP or augmented solely with an autogenous bone graft. These authors reported a cumulative success rate of 93.3% (97.5% for the bone graft group) according to criteria proposed by Buser et al.[17] at 15 years and 1 month of observation. However, the success rate according to the criteria proposed by Albrektsson et al.[16] was generally lower, and on the PRP side at the 5-, 10-, and 15-year observation points it was 96.7%, 94.4% and 43.7%, respectively, while on the control side it was 98.8%, 97.5% and 77%, respectively.

## Conclusions

After 3 years of follow-up on the sinus lifting procedure solely using PRF with simultaneous implantation, the results obtained appear promising, especially regarding of soft tissue management. Thus, PRF can confidently be regarded as a credible alternative to previously used materials.

## ORCID iDs

Sebastian Dominiak ● https://orcid.org/0000-0001-7623-7811
Ewa Karuga-Kuźniewska ● https://orcid.org/0000-0003-0417-2005
Paweł Popecki ● https://orcid.org/0000-0001-5113-2933
Paweł Kubasiewicz-Ross ● https://orcid.org/0000-0001-7305-7161

## References

1. Starch-Jensen T, Aludden H, Hallman M, Dahlin C, Christensen AE, Mordenfeld A. A systematic review and meta-analysis of long-term studies (five or more years) assessing maxillary sinus floor augmentation. *Int J Oral Maxillofac Surg*. 2018;47:103–116. doi:10.1016/j.ijom.2017.05.001

2. Silva L de F, de Lima VN, Faverani LP, de Mendonça, MR, Okamoto R, Pellizzer EP. Maxillary sinus lift surgery: With or without graft material? A systematic review. *Int J Oral Maxillofac Surg*. 2016;45:1570–1576 doi:10.1016/j.ijom.2016.09.023

3. Tatum H Jr. Maxillary and sinus implant reconstructions. *Dent Clin North Am*. 1986;30(2):207–229. PMID:3516738

4. Boyne PJ, James RA. Grafting of the maxillary sinus floor with autogenous marrow and bone. *J Oral Surg*. 1980;38(8):613–616. PMID:6993637

5. Esposito M, Grusovin MG, Rees J, et al. Interventions for replacing missing teeth: Augmentation procedures of the maxillary sinus. *Cochrane Database Syst Rev*. 2010;(3):CD008397. doi:10.1002/14651858.CD008397

6. Jeong TM, Lee JK. The efficacy of the graft materials after sinus elevation: Retrospective comparative study using panoramic radiography. *Maxillofac Plast Reconstr Surg*. 2014;36(4):146–153. doi:10.14402/jkamprs.2014.36.4.146

7. Kowalczewski CJ, Saul JM. Biomaterials for the delivery of growth factors and other therapeutic agents in tissue engineering approaches to bone regeneration. *Front Pharmacol*. 2018;9:513. doi:10.3389/fphar.2018.00513

8. Rodriguez IA, Growney Kalaf EA, Bowlin GL, Sell SA. Platelet-rich plasma in bone regeneration: Engineering the delivery for improved clinical efficacy. *Biomed Res Int*. 2014;2014:392398. doi:10.1155/2014/392398

9. Fernandes G, Yang S. Application of platelet-rich plasma with stem cells in bone and periodontal tissue engineering. *Bone Res*. 2016;4:16036. doi:10.1038/boneres.2016.36

10. Choukroun J, Adda F, Schoeffler C, Vervelle A. An opportunity in perio-implantology: The PRF [in French]. *Implantodontie*. 2001;42:55–62.

11. Schär MO, Diaz-Romero J, Kohl S, Zumstein MA, Nesic D. Platelet-rich concentrates differentially release growth factors and induce cell migration in vitro. *Clin Orthop Relat Res*. 2015;473(5):1635–1643. doi:10.1007/s11999-015-4192-2

12. Chatterjee A, Debnath K. Comparative evaluation of growth factors from platelet concentrates: An in vitro study. *J Indian Soc Periodontol*. 2019;23(4):322–328. doi:10.4103/jisp.jisp_678_18

13. Dominiak M, Mierzwa-Dudek D, Konopka T. Platelet-rich plasma (PRP) in treatment of gingival recession: Preliminary report [in Polish]. *Dent Med Probl*. 2003;40(1):45–55. https://www.dbc.wroc.pl/Content/2399/DMP_2003401045_Domi.pdf

14. Anitua E, Flores J, Alkhraisat MH. Transcrestal sinus lift using platelet concentrates in association to short implant placement: A retrospective study of augmented bone height remodeling. *Clin Implant Dent Relat Res*. 2016;18(5):993–1002. doi:10.1111/cid.12383

15. Aoki N, Maeda M, Kurata M, et al. Sinus floor elevation with platelet-rich fibrin alone: A clinical retrospective study of 1–7 years. *J Clin Exp Dent*. 2018;10(10):e984–e991. doi:10.4317/jced.55113

16. Albrektsson T, Zarb G, Worthington P, Eriksson AR. The long-term efficacy of currently used dental implants: A review and proposed criteria of success. *Int J Oral Maxillofac Implants*. 1986;1(1):11–25. PMID:3527955

17. Buser D, Mericske-Stern R, Bernard JP, Behneke A, Behneke N, Hirt HP. Long-term evaluation of non-submerged ITI implants. Part 1: 8-year life table analysis of a prospective multi-center study with 2359 implants. *Clin Oral Implants Res*. 1997;8:161–172. doi:10.1034/j.1600-0501.1997.080302.x

18. Ortega-Mejia H, Estrugo-Devesa A, Saka-Herrán C, Ayuso-Montero R, López-López J, Velasco-Ortega E. Platelet-rich plasma in maxillary sinus augmentation: Systematic review. *Materials (Basel)*. 2020;13(3):622. doi:10.3390/ma13030622

19. Toffler M, Toscano N, Holtzclaw D. Osteotome-mediated sinus floor elevation using only platelet-rich fibrin: An early report on 110 patients. *Implant Dent*. 2010;19(5):447–456. doi:10.1097/ID.0b013e3181f57288

20. Diss A, Dohan DM, Mouhyi J, Mahler P. Osteotome sinus floor elevation using Choukroun's platelet-rich fibrin as grafting material: A 1-year prospective pilot study with microthreaded implants. *Oral Surg Oral Med Oral Pathol Oral Radiol Endod*. 2008;105(5):572–579. doi:10.1016/j.tripleo.2007.08.021

21. Aoki N, Kanayama T, Maeda M, et al. Sinus augmentation by platelet-rich fibrin alone: A report of two cases with histological examinations. *Case Rep Dent*. 2016;2016:2654645. doi:10.1155/2016/2654645

22. Molemans B, Cortellini S, Jacobs R, Pinto N, Teughels W, Quirynen M. Simultaneous sinus floor elevation and implant placement using leukocyte- and platelet-rich fibrin as a sole graft material. *Int J Oral Maxillofac Implants*. 2019;34(5):1195–1201. doi:10.11607/jomi.7371

23. Mazor Z, Horowitz RA, Del Corso M, Prasad HS, Rohrer MD, Dohan Ehrenfest DM. Sinus floor augmentation with simultaneous implant placement using Choukroun's platelet-rich fibrin as the sole grafting material: A radiologic and histologic study at 6 months. *J Periodontol*. 2009;80(12):2056–2064. doi:10.1902/jop.2009.090252

24. Tajima N, Ohba S, Sawase T, Asahina I. Evaluation of sinus floor augmentation with simultaneous implant placement using platelet-rich fibrin as sole grafting material. *Int J Oral Maxillofac Implants*. 2013;28(1):77–83. doi:10.11607/jomi.2613

25. Simonpieri A, Choukroun J, Del Corso M, Sammartino G, Dohan Ehrenfest DM. Simultaneous sinus-lift and implantation using microthreaded implants and leukocyte- and platelet-rich fibrin as sole grafting material: A six-year experience. *Implant Dent*. 2011;20(1):2–12. doi:10.1097/ID.0b013e3181faa8af

26. Pichotano EC, de Molon RS, de Souza RV, Austin RS, Marcantonio R, Zandim-Barcelos DL. Evaluation of L-PRF combined with deproteinized bovine bone mineral for early implant placement after maxillary sinus augmentation: A randomized clinical trial. *Clin Implant Dent Relat Res*. 2019;21:253–262. doi:10.1111/cid.12713

27. Kanayama T, Horii K, Senga Y, Shibuya Y. Crestal approach to sinus floor elevation for atrophic maxilla using platelet-rich fibrin as the only grafting material: A 1-year prospective study. *Implant Dent*. 2016;25(1):32–38. doi:10.1097/ID.0000000000000327

28. Pichotano EC, de Molon RS, Freitas de Paula LG, de Souza RV, Marcantonio E Jr., Zandim-Barcelos DL. Early placement of dental implants in maxillary sinus grafted with leukocyte and platelet-rich fibrin and deproteinized bovine bone mineral. *J Oral Implantol*. 2018;44:199–206. doi:10.1563/aaid-joi-D-17-00220

29. Nizam N, Eren G, Akcalı A, Donos N. Maxillary sinus augmentation with leukocyte and platelet-rich fibrin and deproteinized bovine bone mineral: A split-mouth histological and histomorphometric study. *Clin Oral Implants Res*. 2018;29(1):67–75. doi:10.1111/clr.13044

30. Hadzik J, Krawiec M, Kubasiewicz-Ross P, Prylińska-Czyżewska A, Gedrange T, Dominiak M. Short implants and conventional implants in the residual maxillary alveolar ridge: A 36-month follow-up observation. *Med Sci Monit*. 2018;24:5645–5652. doi:10.12659/MSM.910404

31. Binahmed A, Stoykewych A, Hussain A, Love B, Pruthi V. Long-term follow-up of hydroxyapatite-coated dental implants: A clinical trial. *Int J Oral Maxillofac Implants*. 2007;22(6):963–968. PMID:18271378

32. McGlumphy EA, Peterson LJ, Larsen PE, Jeffcoat MK. Prospective study of 429 hydroxyapatite-coated cylindric omniloc implants placed in 121 patients. *Int J Oral Maxillofac Implants*. 2003;18(1):82–92. PMID:12608673

33. Schwartz-Arad D, Mardinger O, Levin L, Kozlovsky A, Hirshberg A. Marginal bone loss pattern around hydroxyapatite-coated versus commercially pure titanium implants after up to 12 years of follow-up. *Int J Oral Maxillofac Implants*. 2005;20(2):238–244. PMID:15839117

34. Attia S, Narberhaus C, Schaaf H, et al. Long-term influence of platelet-rich plasma (PRP) on dental implants after maxillary augmentation: Implant survival and success rates. *J Clin Med*. 2020;9(2):391. doi:10.3390/jcm9020391

# Lethal and life-limiting skeletal dysplasias: Selected prenatal issues

Agnieszka Stembalska[1,A–F], Lech Dudarewicz[2,D,E], Robert Śmigiel[3,D–F]

[1] Department of Genetics, Wroclaw Medical University, Poland

[2] Department of Genetics, Polish Mother's Memorial Hospital Research Institute, Łódź, Poland

[3] Department of Pediatrics and Rare Disorders, Wroclaw Medical University, Poland

A – research concept and design; B – collection and/or assembly of data; C – data analysis and interpretation;
D – writing the article; E – critical revision of the article; F – final approval of the article

**Address for correspondence**
Agnieszka Stembalska
E-mail: agnieszka.stembalska@umed.wroc.pl

## Abstract

Skeletal dysplasias are a heterogeneous group of congenital bone and cartilage disorders with a genetic etiology. The current classification of skeletal dysplasias distinguishes 461 diseases in 42 groups. The incidence of all skeletal dysplasias is more than 1 in every 5000 newborns. The type of dysplasia and associated abnormalities affect the lethality, survival and long-term prognosis of skeletal dysplasias. It is crucial to distinguish skeletal dysplasias and correctly diagnose the disease to establish the prognosis and achieve better management. It is possible to use prenatal ultrasonography to observe predictors of lethality, such as a bell-shaped thorax, short ribs, severe femoral shortening, and decreased lung volume. Individual lethal or life-limiting dysplasias may have more or less specific features on prenatal ultrasound. The prenatal features of the most common skeletal dysplasias, such as thanatophoric dysplasia, osteogenesis imperfecta type II, achondrogenesis, and campomelic dysplasia, are discussed in this article. Less frequent dysplasias, such as asphyxiating thoracic dystrophy, fibrochondrogenesis, atelosteogenesis, and homozygous achondroplasia, are also discussed.

**Key words:** prenatal diagnostic, skeletal dysplasia, lethal, life-limiting

# Background

Skeletal dysplasias (SD, also known as osteochondrodysplasias) are an etiologically heterogeneous group of clinical skeletal disorders that disturb the growth and development of bones and cartilage. There are 461 different diseases belonging to SD, which are classified into 42 groups (Nosology and Classification of Genetic Skeletal Disorders 2019) according to their clinical/pathological, biochemical, imaging, and molecular characteristics.[1]

In most cases, SD is the result of mutations in single genes. Less often, dysplasias result from chromosomal anomalies, environmental teratogenic agents or multifactorial inheritance.[2–4] The average incidence of all types of SD is more than 1 in every 5000 newborns.[5–7] The real incidence rate may be higher because SD includes both viable as well as life-limiting and lethal disorders.[2,3] It is suggested that SD of the fetus has an incidence rate of about 5 in every 1000 pregnancies.[8]

# Objectives

The aim of the present review is to better understand the natural history and the course of lethal and life-limiting SD, as well as its molecular etiology. Such understanding will support the management and development of therapeutic possibilities for these conditions.

# Methods of literature search

PubMed was used to search the literature. First, the keywords "life-limiting prognosis AND skeletal dysplasia OR prenatal diagnosis" were used, followed by the single term "lethal skeletal dysplasia", to identify all articles describing poor prognosis of SD diagnosed prenatally. A publication year filter was applied to restrict the results to 1993–2020. If the abstract mentioned syndromes with SD with poor prognosis diagnosed prenatally, the full article text was then analyzed (Fig. 1).

# Results and discussion

## Symptoms of skeletal dysplasia

A characteristic feature of SD is body disproportion due to shortening of the limbs, the trunk, or both.[4–6,9] If the limbs are short (short-limb dwarfism), the linear growth deficiency can involve the proximal segment (humerus/femur), intermediate segment (radius and ulna/tibia and fibula), distal segment (hands/feet), or all segments of the limbs, with the appropriate terms being, respectively, rhizomelic, mesomelic, acromelic shortening, or micromelia. Short-trunked dwarfism is mainly caused
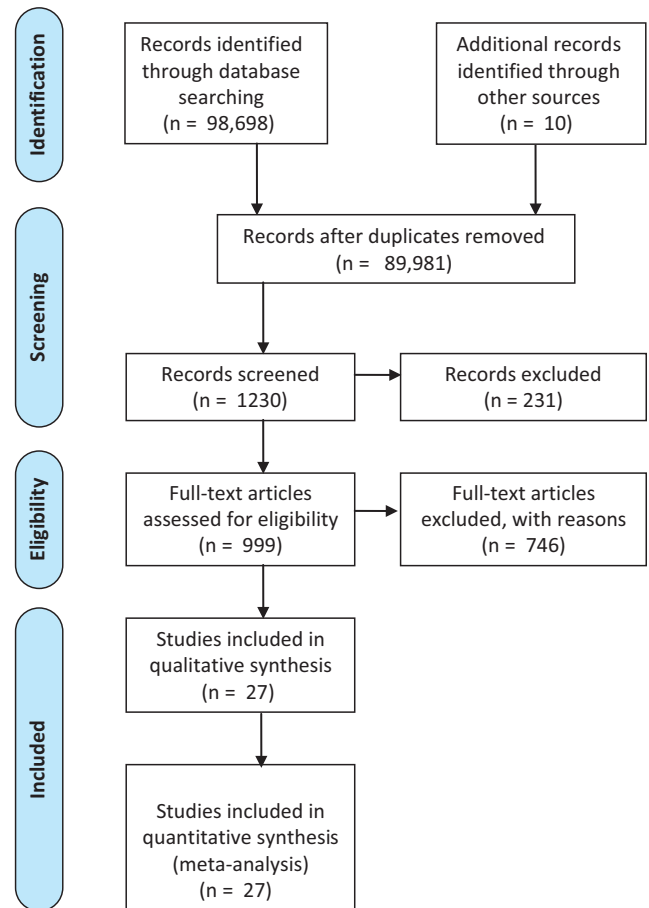


Fig. 1. Literature review strategy

From: Moher D, Liberati A, Tetzlaff J, Altman DG, The PRISMA Group (2009). Preferred Reporting Items for Systematic Reviews and Meta-Analyses: The PRISMA Statement. *PLoS Med.* 6(7): e1000097. doi:10.1371/journal. pmed1000097

by changes in the spine (e.g., vertebral fusion, dysplastic changes, platyspondly, kyphoscoliosis) or/and chest (e.g., small chest, barrel-shaped chest).[6,10,11] Some dysplasias are characterized by deformity, such as bowing of long bones (campomelia) or talipes, asymmetry of limb length, and preaxial (radial/thumb or tibial side) or postaxial (ulnar/little finger or fibular) polydactyly, as well as a high incidence of recurrent fractures.[12] Other features of SD may include facial dysmorphia (e.g., micrognathia, frontal bossing, depressed nasal bridge, midface hypoplasia) and a variety of extra-skeletal manifestations, such as neurological, auditory, visual, pulmonary, cardiac, renal, and psychological symptoms.[3,11]

Therefore, to establish a precise diagnosis of a particular SD, it is important to describe what segment of long bones and what parts of the body are affected. Specifically, it is important to describe which segment of long bones and which part of the body is affected and to evaluate the affected spine and thorax, hands/feet, calvarium, and the face (frontal bossing, presence of nasal bone, micrognathia), and to assess the involvement of other organs.[6,12,13] During prenatal evaluation, it is important

to assess the volume of amniotic fluid and the presence of fetal hydrops.[12,13]

The type of dysplasia and associated abnormalities affect the lethality, survival and long-term prognosis of SD. Early parental diagnosis of SD may improve adequate counseling, pre-delivery planning, pregnancy, and postnatal management.[12]

## Lethal or life-limiting dysplasias

A particular group of SD is lethal or life-limiting. It is suggested that 75–80% of prenatally detected SD is lethal.[8,14,15] Lethality is defined as inevitably causing or capable of causing death in the prenatal period or shortly after birth. According to Krakow, defining lethality in the prenatal period can be accomplished by 2 means: 1) a certain molecular diagnosis of a known lethal dysplasia; or 2) precise clinical assessment or ultrasound showing the presence of changes correlating with lethality.[4] The prediction of lethality is based on specific features, namely, the presence of a bell-shaped thorax, short ribs, severe femoral shortening (>4 standard deviations), lung volume <5th percentile of expected for gestational age, femur length to abdominal circumference ratio <0.16 (especially with polyhydramnios), chest circumference to abdominal circumference ratio <0.6, bone bowing (although also present in viable dysplasias such as achondroplasia), multiple bone fractures, absent or hypoplastic bones, underossification of the spine, and severe micrognathia.[4,11,12,15,16] It may occur that a fetus with lethal SD will survive for a prolonged period of time, especially if lethality was predicted based on ultrasound findings. In this case, clinical reassessment must be performed after birth.[4,17]

## Prenatal diagnosis of skeletal dysplasia

Ultrasound examination is considered an effective method for the diagnosis of prenatal-onset SD. However, studies have estimated that the sensitivity of prenatal ultrasound for the detection of particular SDs is approx. 68%.[15] Few SDs are apparent during the 1st trimester, but most can be ascertained in the 2nd or 3rd trimester ultrasound. A sign of severe SD is a small crown-rump length for gestational age and increased nuchal translucency at 11–13 (+6 days) weeks of gestation if accompanied by shortened or bowed limb, a small chest and ribs, and an undermineralized skull.[2,8] More features of SD can be detected at 18–22 weeks of gestation when the main screening scan of structural defects is performed. At this time, other abnormalities such as congenital heart, renal and brain defects, as well as other anomalies comorbid with SD, can be observed.[14,18] Additional diagnostic test such as 3D ultrasound can allow visualization of dysmorphic findings in SD, such as facial dysmorphism (low-set or deformed ears, micrognathia, midface hypoplasia) and

assessment of scapular anomalies, abnormal calcification patterns, and a detailed evaluation of extremities.[3]

Other SDs become evident in the 3rd trimester, or even after birth, further complicating timely diagnosis.[2,3,12] Non-lethal SDs are most often diagnosed in the late period of infancy or childhood. It has been observed that an earlier onset of dysplasia corresponds with a more severe phenotype.[2]

Prenatal diagnosis of SDs may be determined using fetal magnetic resonance imaging (MRI) and even sometimes with low-dose fetal computed tomography (CT).[2,12,13] Both MRI and CT are performed in the 2nd and 3rd trimesters of gestation. Fetal CT can be used to depict osseous structures in greater detail, whereas fetal MRI can be used to analyze spinal anomalies or vertebral malformations.[2,3,12,13]

There are multiple SDs that display the same prenatal features, although they have different genetic etiologies. Conversely, some SDs display different features but have similar genetic changes. Additionally, pathogenic changes in many different genes may independently correspond with the same SD (genetic heterogeneity).[1,19] An occurrence of an individual SD is rare and most SDs occur without known parental risk factors.[20] For this reason, genetic diagnosis of SD in the prenatal period may be difficult regarding the targeted diagnostics.[19] In clinical practice, in order to make a definitive diagnosis and provide appropriate genetic counselling to enable the choice of further management, the timing of the genetic results may be important. Thus, rapid diagnostics and data analysis are necessary.[19] As a result, the next generation sequencing (NGS) method is often used in fetal genetic diagnosis.[3–5,11,12] It has been proposed by clinicians to use a high-throughput multigene sequencing approach, such as targeted exome sequencing, whole exome sequencing (WES) or whole-genome sequencing (WGS).[19–21] Rapid diagnosis in trios is especially recommended. Fetal and parental DNA are sequenced simultaneously ("trios") for faster and better interpretation of the results.[19] A NGS assay can lead to the detection of pathogenic, likely pathogenic or novel variants of uncertain clinical significance in known or unknown genes. Targeted exome sequencing analyzes regions of the exome with all known disease-causing genes, which leads to minimization of the risk of identifying additional findings.[19] An identification of incidental findings possible in WES and WGS may be an ethical problems. However, WES and WGS may identify novel causative genes in SD.[20] Pre-test genetic counselling for all patients is needed so that they understand the aims and limitations of the test and can give informed consent. Due to the fact that not all genetic variants are clinically relevant, the results of prenatal genomic tests must be always correlated with clinical findings.[2] The diagnosis of SD remains challenging, especially when there is no family history of the disorder.[19] However, in all cases of suspected SD, it is necessary to collect family history, including information from at least 3 generations. Post-test genetic counselling is also necessary.[20]

The final diagnosis of SD may be based on imaging results, histomorphology or genetic methods.[11] Some cases of SD cannot be accurately diagnosed in the prenatal or the postnatal period.

## Selected examples of the most common lethal and life-limiting skeletal dysplasias

The most common types of lethal or life-limiting SDs are thanatophoric dysplasia (26%), osteogenesis imperfecta type II (14%), achondrogenesis (9%), and campomelic dysplasia (2%).[22] The inheritance data, genes involved, OMIM code (Online Mendelian Inheritance in Man), and Orphanet code (portal for rare disease and orphan drugs) for these conditions are summarized in Table 1. Individual lethal or life-limiting dysplasias may have more or less specific features.

1. Thanatophoric dysplasia type I or II (TD1, TD2) results from one de novo allelic mutation in the *FGFR3* gene (OMIM 134934). This gene encodes one of the members of the fibroblast growth factor receptor (FGFR) family. The protein interacts with acidic and basic fibroblast growth hormone to influence bone development and maintenance. Mutations in the *FGFR3* gene play a role in craniosynostosis and various types of SDs, such as those mentioned after achondroplasia. The incidence of TDs is 0.27 in 10,000.

The TD is characterized by shortness of limbs, generalized micromelia, a bowed femur (telephone receiver shaped femur in type I; straight femurs in type II) or other bones of the extremities, brachydactyly, a small chest, thickened soft tissues of the extremities, flattened vertebrae (platyspondyly), an unusually prominent forehead (frontal bossing) and depressed nasal bridge, and a cloverleaf skull (in type II) (Fig. 2). Additionally, polyhydramnios is often present and fractures are never present; however, bowing of the femora may be mistaken for a fracture.[3,13,15,23,24]

2. Osteogenesis imperfecta type II (OI2) is a very severe and lethal SD. The prevalence of OI2 is unknown. Most cases result from sporadic (de novo) heterozygous mutations in the *COL1A1* gene (OMIM 120150) or *COL1A2* gene (OMIM 120160). These genes encode collagen type 1, alpha 1 chain and alpha 2 chain, respectively. Collagen belongs to the family of structural proteins that strengthen and support connective tissue in the body, including bone, tendon and skin.

The OI typically includes fractures, bowed and irregular thickened bones, short/normal size extremities, and a soft, thin skull. Ultrasound findings are distortions of the ribs with fractures or irregular outlines, a narrow thorax, and a compressible head due to underossification of the skull (Fig. 3). Occasionally, hydrops is observed. The OI subtypes a and b are distinguished as b presents milder findings as a result of the less severe reduction of mechanical resistance of bone structure. In type IIb, the fractures are less severe, the upper limbs are less affected (due to smaller

**Table 1.** Selected lethal or life-limiting skeletal dysplasias

| Skeletal dysplasia | OMIM* | ORPHA code** | Inheritance | Gene/genes (chromosome location) |
|---|---|---|---|---|
| Thanatophoric dysplasia<br>type I<br>type II | 187600<br>187601 | 2655<br>1860<br>93274 | AD | *FGFR3* (4p16. 3) |
| Osteogenesis imperfecta type II | 166210 | 216804 | AD | *COL1A1* (17q21.33)<br>*COL1A2* (7q21.3) |
| Achondrogenesis<br>type Ia<br>type Ib<br>type II | 200600<br>600972<br>200610 | 932<br>93299<br>93298<br>93296 | AR – type Ia, Ib<br>AD – type II | *TRIP11* (14q32) – type Ia<br>*SLC26A2* (5q32) – type Ib<br>*COL2A1* (*12q13.11*) – type II |
| Campomelic dysplasia | 114290 | 140 | AD | *SOX9* (17q24) |
| Asphyxiating thoracic dystrophy | 208500 | 474 | AR | *DYNC2H1* (11q22.3), *DYNC2LI1* (2p21), *DYNC2I2* (9q34.11), *DYNLT2B* (3q29), *DYNC2I1* (7q36.3), *WDR19* (4p14), *IFT140* (16p13.3), *TTC21B* (2q24.3), *IFT80* (3q25.33), *IFT172* (2p23.3), *IFT81* (12q24.11), *IFT52* (20q13.12), *TRAF3IP1* (2q37.3), *CFAP410* (21q22.3), *CEP120* (5q23.2), *KIAA0586* (14q23.1), *KIAA0753* (17p13.1) |
| Fibrochondrogenesis<br>type 1<br>type 2 | 228520<br>614524 | 2021 | AR – type 1<br>AR or AD – type 2 | *COL11A1* (1p21) – type 1<br>*COL11A2* (6p21.3) – type 2 |
| Atelosteogenesis<br>type I<br>type II<br>type III | 108720<br>256050<br>108721 | 1190<br>56304<br>56305 | AD – type I, III<br>AR – type II | *FLNB* (3p14) – type I, III<br>*SLC26A2* (5q32) – type II |
| Homozygous achondroplasia | 100800 | 15 | AD (homozygous mutation) | *FGFR3* (4p16.3) |

* OMIM – https://omim.org; ** Orphanet – https://www.orpha.net; AR (autosomal recessive) – homozygous mutation or compound heterozygous mutations; AD (autosomal dominant) – heterozygous mutation.
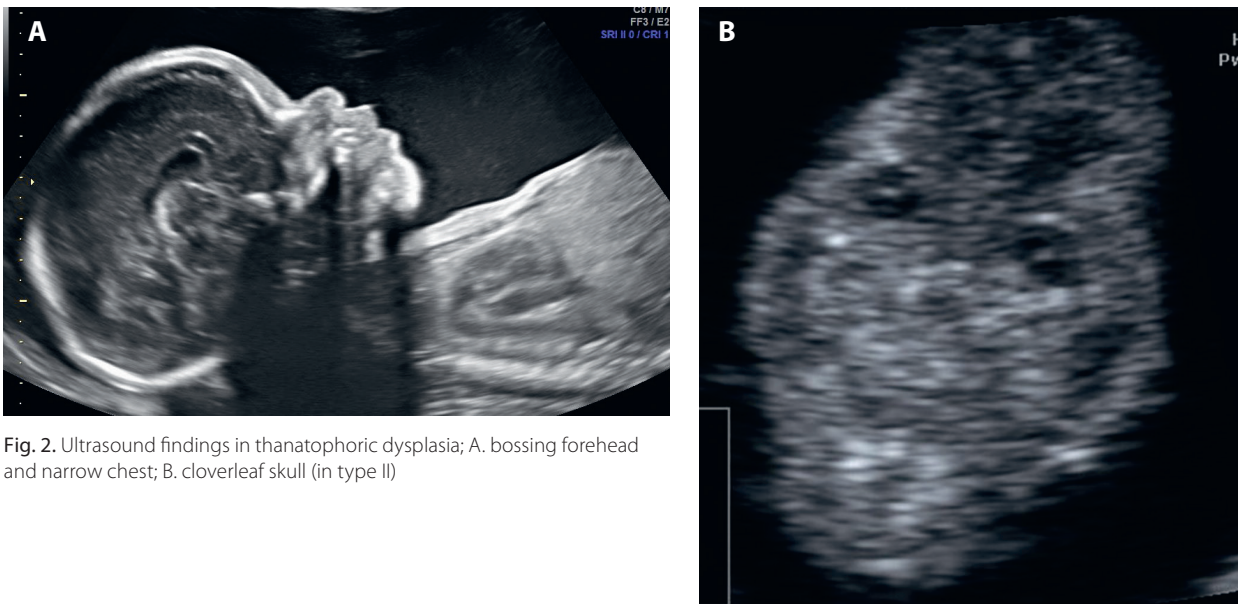
Fig. 2. Ultrasound findings in thanatophoric dysplasia; A. bossing forehead and narrow chest; B. cloverleaf skull (in type II)
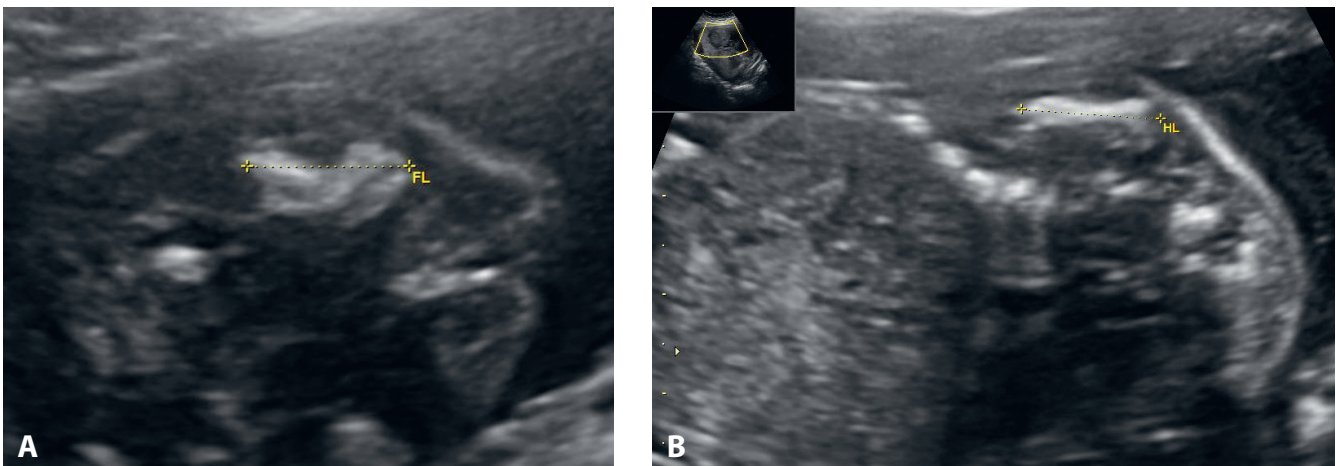


Fig. 3. Ultrasound findings in osteogenesis imperfecta type II; A. short, broken femur; B. narrow chest and shortened humerus

muscle mass than in the lower limbs), and the ribs have a wavy appearance, most often without fractures.

Radiographic features include Wormian bones, multiple fractures, crumbled bones, and characteristic beading of the ribs due to healing callus formation.[10,15,22,24,25]

3. Achondrogenesis type Ia, Ib, II (ACG1A, ACG1B, ACG2) is caused by autosomal recessive mutations in the *TRIP11* gene (type Ia) (OMIM 604505) or the *SLC26A2* gene (type Ib) (OMIM 606718) and de novo autosomal dominant mutations in the *COL2A1* gene (type II). The *TRIP11* gene encodes Golgi microtubule-associated protein 210 (GMAP-210). This protein plays a role in maintaining the structure of the Golgi apparatus, in the transport of certain proteins out of cells, and is believed to be important in the developing skeleton. The *SLC26A2* gene encodes a sulfate transporter that is responsible for adequate sulfation of proteoglycans in the cartilage matrix; this process is necessary for proper endochondral bone formation. Mutations

in the *SLC26A2* gene can cause other disorders, such as lethal atelosteogenesis (described below).

The prevalence of all ACG types is unknown. This severe SD presents with micromelia, thickened soft tissues, a poorly ossified skull, bones of the spine that are not mineralized or fully formed, flared ribs, a small thorax, and micrognathia (Fig. 4). During pregnancy, polyhydramnios and fetal hydrops are often observed.[3,13,15,26,27]

4. Campomelic dysplasia (CMPD) results from autosomal dominant mutations in the *SOX9* gene (OMIM 608160). The gene encodes the transcription factor SOX-9, which plays a critical role during embryonic development – especially in skeletal development and sex determination.

The incidence of CMPD is less than 1 in 1,000,000. This dysplasia is characterized by angulated femora or other bones of the extremities (campomelia), shortened limbs (micromelia), club feet with brachydactyly, hypoplastic scapulae and tibiae, 11 pairs of ribs, a bell-shaped chest, ambiguous genitalia (sex-reversal in males), micrognathia, flattened
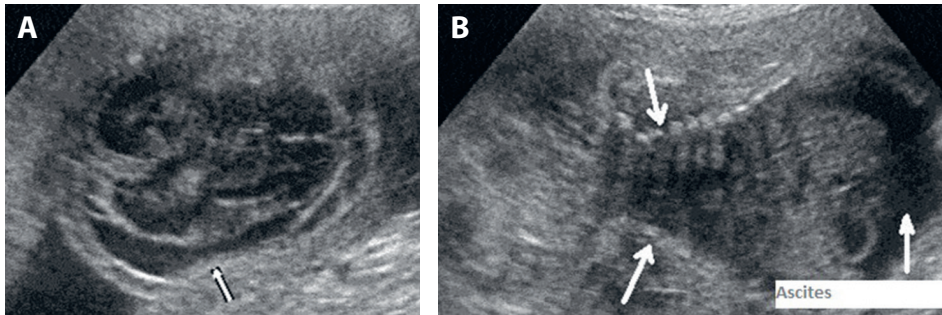
**Fig. 4.** Ultrasound findings in achondrogenesis; A. unossified skull; B. narrow chest and ascites
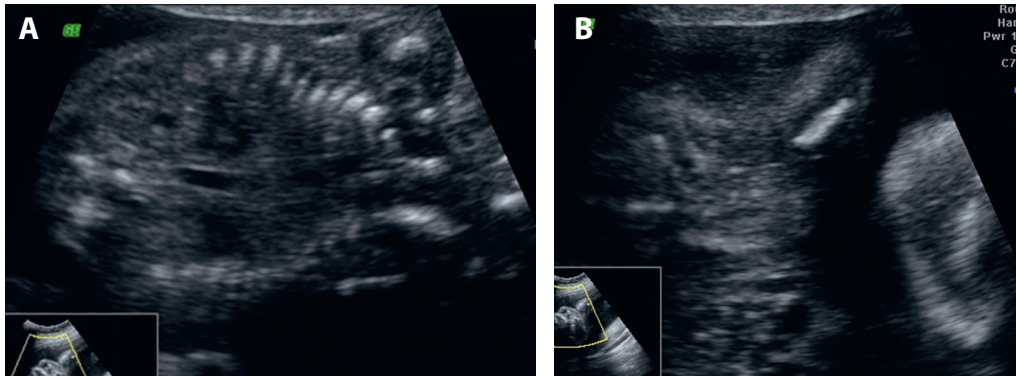


**Fig. 5.** Ultrasound findings in campomelic dysplasia; A. distorted ribs; B. hypoplastic scapula

facial features, an unusually prominent forehead, and ventriculomegaly (Fig. 5).[3,13,15,28] Lethality is mainly due to softness of the tracheal cartilage causing respiratory failure.

## Other, less common lethal skeletal dysplasias

1. Asphyxiating thoracic dystrophy (ATD; short-rib thoracic dysplasia – SRTD) is very heterogeneous regarding the genetic cause and results from autosomal mutations in 1 of at least 17 genes (*DYNC2H1* – OMIM 603297, *DYNC2LI1* – OMIM 617083, *DYNC2I2* – OMIM 613363, *DYNLT2B* – OMIM 617353, *DYNC2I1* – OMIM 615462, *WDR19* – OMIM 608151, *IFT140* – OMIM 614620, *TTC21B* – OMIM 612014, *IFT80* – OMIM 611177, *IFT172* – OMIM 607386, *IFT81* – OMIM 605489, *IFT52* – OMIM 617094, *TRAF3IP1* – OMIM 607380, *CFAP410* – OMIM 603191, *CEP120* – OMIM 613446, *KIAA0586* – OMIM 610178, *KIAA0753* – OMIM 617112). These genes encode proteins involved in the formation or function of cilia, which play a role in the signaling pathways important for the growth, proliferation and differentiation of cells during the formation and maintenance of cartilage and bone. The prevalence of ATD is unknown.

It includes mildly short limbs with mild bowing, a very narrow thorax and short ribs (a small chest), pulmonary hypoplasia, and renal dysplasia (renal cysts).[1,19,29]

2. Fibrochondrogenesis type 1 or 2 (FBCG2) results from autosomal recessive mutations in the *COL11A1* gene (type 1) (OMIM 120280) or autosomal recessive or dominant mutations in the *COL11A2* gene (type 2) (OMIM 120290). These 2 genes encode components of type XI collagen called the pro-alpha1 chain and pro-alpha2 (XI) chain, respectively. Type XI collagen is important in the structure of cartilage, the inner ear and the nucleus pulposus in the spine.

The incidence of FBCG2 is less than 1 in 1,000,000. It is characterized by shortened long bones (micromelia with broad metaphyseal ends of bone, described as dumbbell-shaped) with relatively normal hands and feet and flattened vertebrae (platyspondyly). Other features are a narrow chest with short, wide ribs and a round and prominent abdomen, and facial dysmorphism (prominent eyes, a flat midface with a small nose and flat nasal bridge, micrognathia).[22,30]

3. Atelosteogenesis type I, II or III (AO1, AO2, AO3) results from autosomal dominant mutations in the *FLNB* gene (type I and III) (OMIM 603381) or autosomal recessive mutations in the *SLC26A2* gene (type II). The *FLNB* gene encodes filamin B protein. This protein participates in normal cell growth and division, maturation of chondrocytes, and ossification of cartilage.

The incidence of all types of atelosteogenesis is less than 1 in 1,000,000. Clinical findings are severe short-limbed dwarfism (micromelia); dislocated hip, knee and elbow joints; club feet; a narrow chest; and craniofacial dysmorphism (prominent forehead, hypertelorism, a depressed nasal bridge with a grooved tip, micrognathia, and frequently a cleft palate). Polyhydramnios in atelosteogenesis type 1 and hydrocephalus in type III may occur.[22,31]

4. Homozygous achondroplasia (ACH) results from homozygous mutations in the *FGFR3* gene (OMIM 134934). The prevalence of homozygous ACH is unknown. Homozygous achondroplasia occurs if both parents suffer from

achondroplasia. Sonographic findings are a femoral angle >130°, dysmorphic features (frontal bossing, depressed nasal bridge, macrocephaly), trident hands, and severe long bone shortening in 1st or 2nd trimester.[15]

## Conclusions

The final diagnosis of SD may require a multidisciplinary team including obstetricians, radiologists and geneticists. In all cases of prenatally confirmed SD, genetic counseling for parents is necessary. In the case of lethal dysplasias, all possibilities of further management should be presented, both continuation of the pregnancy and termination of the pregnancy (if this solution is permitted by law).[3] When the pregnancy continues, perinatal hospice care as well as palliative care after birth are proposed. If a diagnosis of lethal dysplasia or life-limiting dysplasia is suspected in the prenatal period, pediatric evaluation or multidisciplinary clinical assessment after birth is essential to verify the diagnosis. In the case of intrauterine death, physical evaluation, radiographic and autopsy examination, and storing fetal blood or other tissues as a source of DNA are recommended.[2,3]

It should be emphasized that genetic counselling of the parents of a child or fetus affected by SD is necessary before the next pregnancy to discuss the recurrence risk and the possibility of preimplantation or prenatal diagnostic tests. It should also be emphasized that lethal conditions associated with de novo mutations may have less than a 1% recurrence risk (not counting the possibility of germline mosaicism), whereas SDs associated with autosomal recessive inheritance are associated with a 25% recurrence risk.

### ORCID iDs

Agnieszka Stembalska  https://orcid.org/0000-0003-3528-6582
Lech Dudarewicz  https://orcid.org/0000-0003-0595-6194
Robert Śmigiel  https://orcid.org/0000-0003-2930-9549

## References

1. Mortier GR, Cohn DH, Cormier-Daire V, et al. Nosology and classification of genetic skeletal disorders: 2019 revision. *Am J Med Genet A*. 2019;179(12):2393–2419. doi:10.1002/ajmg.a.61366
2. Savarirayan R, Rossiter JP, Hoover-Fong JE, et al; Skeletal Dysplasia Management Consortium. Best practice guidelines regarding prenatal evaluation and delivery of patients with skeletal dysplasia. *Am J Obstet Gynecol*. 2018;219(6):545–562. doi:10.1016/j.ajog.2018.07.017
3. Noel AE, Brown RN. Advances in evaluating the fetal skeleton. *Int J Womens Health*. 2014;13(6):489–500. doi:10.2147/IJWH.S47073
4. Krakow D. Skeletal dysplasias. *Clin Perinatol*. 2015;42(2):301–319. doi:10.1016/j.clp.2015.03.003
5. Cho SY, Jin DK. Genetic skeletal dysplasias for pediatricians. *Ann Pediatr Endocrinol Metab*. 2015;20(4):187–191. doi:10.6065/apem.2015.20.4.187
6. Krakow D, Rimoin D. The skeletal dysplasias. *Genet Med*. 2010;12(6):327–341. doi:10.1097/GIM.0b013e3181daae9b
7. Ipek MS, Ozmen CA. Skeletal dysplasias that cause thoracic insufficiency in neonates. *Medicine (Baltimore)*. 2016;95(14):e3298. doi:10.1097/MD.0000000000003298
8. Schramm T, Mommsen H. Fetal skeletal disorders. *Ultraschall Med*. 2018;39(6):61–634. doi:10.1055/a-0660-9417
9. Campeau P, Schlesinger AE. Skeletal dysplasias. Endotext. South Dartmouth, USA: MDText.com, Inc. https://www.ncbi.nlm.nih.gov/books/NBK279130/. Updated January 30, 2017.
10. Chaudhary V, Bano S. Imaging in short stature. *Indian J Endocrinol Metab*. 2012;16(5):692–697. doi:10.4103/2230-8210.100641
11. Sewell MD, Chahal A, Al-Hadithy N, Blunn GW, Molloy S, Hashemi-Nejad A. Genetic skeletal dysplasias: A guide to diagnosis and management. *J Back Musculoskelet Rehabil*. 2015;28(3):575–590. doi:10.3233/BMR-140558
12. Victoria T, Zhu X, Lachman R, et al. What is new in prenatal skeletal dysplasias? *AJR Am J Roentgenol*. 2018;210(5):1022–1033. doi:10.2214/AJR.17.19337
13. Krakow D, Lachman RS, Rimoin DL. Guidelines for the prenatal diagnosis of fetal skeletal dysplasias. *Genet Med*. 2009;11(2):127–133. doi:10.1097/GIM.0b013e3181971ccb
14. Schramm T, Gloning KP, Minderer S, et al. Prenatal sonographic diagnosis of skeletal dysplasias. *Ultrasound Obstet Gynecol*. 2009;34(2):160–170. doi:10.1002/uog.6359
15. Milks KS, Hill LM, Hosseinzadeh K. Evaluating skeletal dysplasias on prenatal ultrasound: An emphasis on predicting lethality. *Pediatr Radiol*. 2017;47(2):134–145. doi:10.1007/s00247-016-3725-5
16. Alanay Y, Lachman RS. A review of the principles of radiological assessment of skeletal dysplasias. *J Clin Res Pediatr Endocrinol*. 2011;3(4):163–178. doi:10.4274/jcrpe.463
17. Watson SG, Calder AD, Offiah AC, Negus S. A review of imaging protocols for suspected skeletal dysplasia and a proposal for standardisation. *Pediatr Radiol*. 2015;45(12):1733–1737. doi:10.1007/s00247-015-3381-1
18. Hurst JA, Firth HV, Smithson S. Skeletal dysplasias. *Semin Fetal Neonatal Med*. 2005;10(3):233–241. https://doi.org/10.1016/j.siny.2004.12.001
19. Chandler N, Best S, Hayward J, et al. Rapid prenatal diagnosis using targeted exome sequencing: A cohort study to assess feasibility and potential impact on prenatal counseling and pregnancy management. *Genet Med*. 2018;20(11):1430–1437. doi:10.1038/gim.2018.30
20. Tang J, Zhou C, Shi H, et al. Prenatal diagnosis of skeletal dysplasias using whole exome sequencing in China. *Clin Chim Acta*. 2020;507:187–193. doi:10.1016/j.cca.2020.04.031
21. Liu Y, Wang L, Yang YK, et al. Prenatal diagnosis of fetal skeletal dysplasia using targeted next-generation sequencing: An analysis of 30 cases. *Diagn Pathol*. 2019;14(1):76. doi:10.1186/s13000-019-0853-x
22. Savoldi AM, Villar MAM, Machado HN, Llerena Júnior JC. Fetal skeletal lethal dysplasia: Case report. *Rev Bras Ginecol Obstet*. 2017;39(10):576–582. doi:10.1055/s-0037-1603943
23. French T, Savarirayan R. Thanatophoric dysplasia. GeneReviews®. Seattle, USA: University of Washington. https://www.ncbi.nlm.nih.gov/books/NBK1366/. Published May 21, 2004. Updated June 18, 2020.
24. Wainwright H. Thanatophoric dysplasia: A review. *S Afr Med J*. 2016;106(6 Suppl 1):S50–S53. doi:10.7196/SAMJ.2016.v106i6.10993
25. Steiner RD, Basel D. *COL1A1/2* osteogenesis imperfecta. GeneReviews®. Seattle, USA: University of Washington. https://www.ncbi.nlm.nih.gov/books/NBK1295/. Published January 28, 2005. Updated December 12, 2019.
26. Gregersen PA, Savarirayan R. Type II collagen disorders overview. GeneReviews®. Seattle, USA: University of Washington. https://www.ncbi.nlm.nih.gov/books/NBK540447/. Published April 25, 2019.
27. Bonafé L, Mittaz-Crettol L, Ballhausen D, Superti-Furga A. Achondrogenesis type 1B. GeneReviews®. Seattle, USA: University of Washington. https://www.ncbi.nlm.nih.gov/books/NBK1516/. Published August 30, 2002. Updated November 14, 2013.
28. Unger S, Scherer G, Superti-Furga A. Campomelic dysplasia. GeneReviews®. Seattle, USA: University of Washington. https://www.ncbi.nlm.nih.gov/books/NBK1760/. Published July 31, 2008. Updated May 9, 2013.
29. Waters AM, Beales PL. Ciliopathies: An expanding disease spectrum. *Pediatr Nephrol*, 2011;26:1039–1056. doi:10.1007/s00467-010-1731-7
30. Bekdache GN, Begam MA, Chedid F, Al-Gazali L, Mirghani H. Fibrochondrogenesis: Prenatal diagnosis and outcome. *J Obstet Gynaecol*. 2013;33(7):663–668. doi:10.3109/01443615.2013.817977
31. Superti-Furga A, Unger S. Atelosteogenesis type 2. GeneReviews®. Seattle, USA: University of Washington. https://www.ncbi.nlm.nih.gov/books/NBK1317/. Published August 3, 2002. Updated September 24, 2020.